UNIVERSIDAD DE CHILE
FACULTAD DE CIENCIAS FÍSICAS Y MATEMÁTICAS
ESCUELA DE POSTGRADO Y EDUCACIÓN CONTINUA

STUDY OF LOCAL ENTROPY GENERATION IN POROUS MEDIA UNDER LAMINAR AND TURBULENT REGIMES

TESIS PARA OPTAR AL GRADO DE
DOCTOR EN CIENCIAS DE LA INGENIERÍA, MENCIÓN FLUIDODINÁMICA

CRISTÓBAL ANDRÉS SARMIENTO LAUREL

PROFESOR GUÍA:
WILLIAMS CALDERÓN MUÑOZ

MIEMBROS DE LA COMISIÓN:
JOSÉ CARDEMIL IGLESIAS
RODRIGO ESCOBAR MORAGAS
ALDO TAMBURRINO TAVANTZIS
MÓNICA ZAMORA ZAPATA

Este trabajo ha sido parcialmente financiado por ANID, a través de la beca de doctorado nacional 2018

SANTIAGO DE CHILE
2023

RESUMEN

ESTUDIO DE LA GENERACIÓN DE ENTROPÍA LOCAL EN MEDIOS POROSOS BAJO REGIMEN LAMINAR Y TURBULENTO

Recientemente, en los últimos 15 años, las estructuras porosas han sido propuestas como una solución interesante en el diseño de sistemas de intercambio y almacenamiento de energía a altas temperaturas, ambos para aplicaciones de en sistemas de concentración solar de potencia. La amplia área de transferencia de la matriz porosa permite alcanzar altas eficiencias de conversión, particularmente en aplicaciones de alta temperatura para gases compresibles (CO_2 o aire). Sin embargo, la presencia de la matriz porosa incrementa la resistencia hidrodinámica sobre el flujo y, en consecuencia, genera irreversibilidades que controlar. Asimismo, las duras condiciones de operación en algunos casos y la complejidad inherente a la simulación de un medio poroso tortuoso hacen que la tarea de simulación y análisis aún sea un problema complejo de resolver en regímenes turbulentos. Por lo tanto, para este trabajo se propone la generación de entropía como una figura de mérito integral capaz de incorporar los diferentes mecanismos de generación de irreversibilidades en una sola variable sobre el transporte y gestión de potencial energético. Adicionalmente, un análisis enfocado en la entropía, su transporte y generación proporciona la posibilidad de distinguir la calidad del potencial energético de cada flujo de energía desde o hacia el sistema.

A pesar de que la entropía como concepto tiene al menos 200 años, no existe una expresión y un método de simulación que permita determinar la generación de entropía a escala local (LEG) en medios porosos y distinguir sus diferentes mecanismos de generación. Al incorporar un matriz porosa al análisis, aparecen mecanismos de transferencia de calor volumétrica y de disipación de energía adicionales que no se encuentran en flujos internos libres. Esto hace necesario el estudio sobre la modelación de dichos mecanismos adicionales y su repercusión en la generación de entropía. El presente trabajo propone un análisis teórico sobre las ecuaciones fundamentales que gobiernan el transporte de masa, energía y momentum, y a partir de ellas, desarrolla una expresión físico-matemática para el transporte y generación de entropía en medios porosos. Además, se presenta una metodología de análisis para aplicar el modelo teórico de LEG en herramientas de simulación de CFD.

Se presenta un análisis adimensional preliminar sobre la expresión de LEG para determinar las variables adimensionales que definen el nivel de significancia de cada mecanismo de LEG. Posteriormente, se implemeta un experimento numérico en un caso de estudio simplificado y representativo, para estudiar el comportamiento de un canal poroso bajo 200 configuraciones variando las condiciones de borde de diseño y operación. Los resultados muestran que las irreversibilidades asociadas a la resistencia hidráulica en medios porosos pueden dominar la generación de entropía global por sobre los mecanismos de transferencia de calor volumétrica. Asimismo, se definen puntos de inflexión donde la resistencia hidráulica puede dominar la LEG para diferentes configuraciones de Reynolds, porosidad y diferencia de temperatura entre el medio sólido y líquido. La resistencia hidrodinámica de Forchheimer puede dominar la LEG por sobre los efectos asociados a la transferencia de calor volumétrica para regímenes de alto número de Reynolds ($Re_D > 100$), con una porosidad menor a 0,6.

Abstract

Recently, in the last 15 years, porous structures have been proposed as an interesting solution in the design of high-temperature energy storage and exchange systems, both for applications in concentrated solar power (CSP) systems. The wide exchange area of the solid matrix allows to reaching higher conversion efficiencies, particularly in high-temperature applications (1000°C) for compressible gases (CO_2 or air). However, the presence of the solid matrix increases the hydrodynamic resistance of the flow and, consequently, generates irreversibilities to control. Similarly, the arduous operating conditions in some cases and the inherent complexity of simulating a tortuous porous medium make the task of simulation and analysis still a complex problem to solve in turbulent systems. Therefore, in this work, the generation of entropy is proposed as a comprehensive figure of merit capable of incorporating the different mechanisms of generation of irreversibilities in a single variable on the transport and management of the energy. Additionally, an analysis focused on the transport and generation of entropy to distinguish the quality of the energy potential of each energy flow interacting with a system.

Despite the fact that entropy as a concept is at least 200 years old, there is no methodology in the literature that allows to determining the local entropy generation (LEG) in porous media and distinguishing its different generation mechanisms. When a porous matrix is included in the analysis, additional volumetric heat transfer and energy dissipation mechanisms appear that are not found in free internal flows. This makes it necessary to study the modeling of these additional mechanisms and their impact on the generation of entropy. This work proposes a theoretical analysis of the transport equations of mass, energy, and momentum, and from them develops a physical-mathematical expression for the transport and generation of entropy in porous media. Furthermore, a methodology is presented to apply the LEG theoretical model in CFD simulation tools.

A preliminary dimensionless analysis on the LEG expression is presented to determine the dimensionless variables that define the level of significance of each LEG mechanism. Subsequently, a numerical experiment is implemented in a porous channel under 200 design and operation configurations. The results show that the irreversibilities associated with hydraulic resistance in porous media can dominate the LEG rate over volumetric heat transfer mechanisms. Similarly, inflection points are determined where the hydraulic resistance can dominate the LEG for different Re_D, porosity, and inlet temperature difference. The hydrodynamic resistance effect dominate the total LEG in comparison to the volumetric heat transfer for high porous Reynolds regimes ($Re_D > 100$) when the porosity is below 0.6.

Agradezco infinitamente a mi madre por su amor incondicional y por ser el ejemplo que me motivó a perseverar en este proceso. A mi padre por su apoyo y cariño permanente. A mis segundos padre y madre, José Carlos y Pamela por su cariño y apoyo en todo momento. A mis hermanas por su cariño y comprensión. A mi pareja por su paciencia, por ser la compañera perfecta en los momentos más críticos de mi travesía. Agradezco también a mis amigas y amigos por su cariño y apoyo.

Asimismo, a mis profesores por su dedicación y consejo. En particular a José Cardemil por confiar en mi como estudiante durante estos largos años de trabajo y formación como investigador. Muchas gracias profesor por su dedicación en la labor científica y docente, esos fueron los factores claves en mi desarrollo como investigador.

Acknowledgments

I gratefully acknowledge the support of this work by the CONICYT-PCHA/Doctorado Nacional/2018-21181794 doctoral fellowship.

Table of Content

List of Tables

List of Figures

Nomenclature

a_i solid-fluid surface area per unit of volume

$C_\mu, C_{1\varepsilon}, C_{2\varepsilon}, \sigma_k, \sigma_\varepsilon$ coefficients for $k-\varepsilon$ turbulence model

c_E Ergun's inertia coefficient

c_p specific heat at constant pressure

d_p mean pore diameter

Da Darcy number, $Da = \frac{K}{{d_p}^2}$

e internal energy per unit of mass

Ec Eckert number, $Ec = \frac{{U_0}^2}{c_{p,f}(T_w - T_{f,in})}$

f_i mass forces vector

G_i generation rate of ${k_t}^i$

H channel height

h_i interfacial convective heat transfer

K permeability of the porous media

k turbulent kinetic energy (TKE)

k_1, k_2 Darcy and Forchheimer hydrodynamic resistance parameters

k_Θ variance of the temperature time-fluctuation

L channel length

N_{CHT} dimensionless LEG regarded to conductive heat transfer

N_D dimensionless LEG due to Darcy hydrodynamic resistance

N_{FH} dimensionless LEG due to Forchheimer hydrodynamic resistance

N_{Sgen} entropy generation comparison dimensionless factor, $\frac{\dot{S}_{Phi}}{\dot{S}_{Theta}}$

N_{VHT} dimensionless LEG due to Forchheimer hydrodynamic resistance

N_V dimensionless LEG regarded to Forchheimer hydrodynamic resistance

Nu_H Nusselt number, $Nu_H = \frac{h_i H}{\lambda_f}$

P pressure

P_i production rate of $\langle k_t \rangle^i$

$P_{k,\Theta}$ production rate of k_Θ

Pr Prandtl number, $Pr = \frac{\mu c_{p,f}}{\lambda_f}$

$Pr_{t\phi}$ turbulent volume-average Prandtl number, $Pr_{t\phi} = \frac{\mu_{t\phi}}{\alpha_{t\phi}}$

Pr_t turbulent Prandtl number, $Pr_t = \frac{\mu_t}{\alpha_t}$

q_j net the heat flux

R hydrodynamic drag force of the porous media

R_{gas} ideal gas constant

Re_D Reynolds number based in d_p and u_D, $Re_D = \frac{\rho u_D d_p}{\mu}$

Re_H Reynolds number based in H and u_D, $Re_H = \frac{\rho u_D H}{\mu}$

s specific entropy

T temperature

t time

u fluid velocity

U_0 fluid velocity at the inlet

u_D Darcy's velocity

$\dot{s}_{\phi,DF}$ LEG rate associated to the Darcy–Forchheimer's hydrodynamic resistance

$\dot{s}_{\Theta,V}$ LEG rate regarded to the volumetric heat transfer between the solid and fluid phases

$\langle \dot{s}_\Phi \rangle^v$ LEG rate due to hydrodynamic and viscous effects

$\langle \dot{s}_\Theta \rangle^v$ LEG rate regarded to heat transfer

$\langle \dot{s}_{gen} \rangle^v$ total entropy generation rate

$\left\langle \dot{s}_{\Phi,\bar{D}} \right\rangle^v$ LEG rate due to viscous dissipation related to the time-average velocity

$\langle \dot{s}_{\Phi,D'} \rangle^v$ LEG rate by viscous dissipation regarded to the fluid velocity time-fluctuations

$\left\langle \dot{s}_{\Theta,\bar{C}} \right\rangle^v$ LEG rate by the conductive heat transfer related to the time-average fluid temperature

$\langle \dot{s}_{\Theta,C'} \rangle^v$ LEG rate due to the conductive heat transfer associated to the fluid temperature time-fluctuations

Greek Symbols

α thermal diffusivity

$\alpha_{t\phi}$ macroscopic turbulent thermal diffusivity

α_t turbulent thermal diffusivity

ε dissipation rate of TKE

ε_Θ dissipation rate of k_Θ

γ dimensionless inlet temperature, $\gamma = \frac{T_{in}}{T_w - T_{in}}$

λ thermal conductivity

λ_{fs} local thermal conductivity tensor

$\lambda_{t\phi}$ macroscopic turbulent thermal conductivity

μ viscosity

$\mu_{t\phi}$ macroscopic turbulent viscosity

μ_t turbulent viscosity

Φ viscous dissipation rate

ϕ porosity

ρ density

σ surface forces tensor

θ dimensionless temperature difference, $\gamma = \frac{T_w - T}{T_w - T_{in}}$

Subscripts

f fluid

in inlet

out outlet

s solid

w wall side

Special Symbols

$\bar{\varphi}$ time-average value of φ

φ' time-fluctuation of φ

${}^{i}\varphi$	spatial-dispersion of φ
$\langle\varphi\rangle^{i}$	intrinsic volume-average value of φ
$\langle\varphi\rangle^{v}$	volume-average value of φ

Chapter 1

Introduction

1.1 First steps of the Entropy in history

The second law of thermodynamics and its fundamentals have been the object of wide scientific study and discussion since the XIX century. In 1823, Sadi Carnot, aimed by his father's work, Lazare Carnot, published his reflections on the motive power of heat (Carnot, 1824a,b). At that time, the young thermal engines were subordinated to efficiencies of around 2% (Hanlon, 2020). From this, Carnot focused his study on the recognition of the phenomena responsible for potential losses in energy transfer processes. Carnot proposed that heat flows from high to low temperatures, as a mass of water that flows between high and low heights in a waterfall. From this analogy, Carnot established that the maximum motive power potential of a heat engine depends only on the temperature difference, independent of the engine design. In the same way, the maximum power potential of hydraulic systems depends only on the height difference, $\dot{m}(z_{high} - z_{low})$ (Kostic, 2011). In addition, Carnot coined the concept of reversibility, establishing that directionality exists in thermal processes, and effects such as friction and/or heat transfer can make a process less reversible and consequently less efficient (Salvi and Schettino, 2019; Hanlon, 2020). With this idea in mind, Carnot defined an ideal cycle composed only of reversible processes, the famous Carnot's cycle. This cycle establishes an upper limit for the efficiency of a real thermal engine, subject to the operating temperatures of the said system. Through his analogy between water falls and heat transfer, Carnot established that the maximum efficiency that a thermal engine can reach is the Carnot's cycle efficiency, and it only depends on the temperature difference between the energy source and energy sink.

Despite the fact that Carnot's ideas laid the foundations for building the second law of thermodynamics, in its time, his self-managed publication did not have much dissemination and attention from the scientific community. The document with Carnot's reflections had no more than 600 copies in circulation (Salvi and Schettino, 2019). It was thanks to the subsequent publication in 1834 of the mathematician Emile Clapeyron about the Carnot's reflections (Clapeyron, 1834; Girolami, 2020; Hanlon, 2020), that these concepts would spread throughout the scientific community. Due to the work of Clapeyron, the ideas of Carnot reached to inspire William Thompson, or most known in history as Lord Kelvin, for his later

work about the second law of thermodynamics. Due to the limited number of available copies of Carnot's reflections, in 1845 it was almost impossible to find an original copy. It was also impossible for Kelvin to find a copy of Carnot's memoirs in Paris (Salvi and Schettino, 2019).

Later, a few months apart, in 1850 Kelvin (Thomson, 1853) and Clausius (Clausius, 1850) presented the statements that restrict the operation of thermal machines and refrigeration systems, respectively. Clausius established that "No process is possible whose sole result is the transfer of heat from a body of lower temperature to a body of higher temperature", establishing an operating framework for refrigeration systems. For his part, Kelvin established that "It is impossible, by means of inanimate material agency, to derive a mechanical effect from any portion of matter by cooling it below the temperature of the coldest of the surrounding objects", where he defines the restriction for the operation of thermal engines.

In his fourth memoir (Clausius, 1856), in 1854, based on Carnot's second principle (developed numerically by Clapeyron) on the efficiency of a reversible engine, Clausius established the relationship between the heat transfer Q and the temperature T that would give way to the constitution of entropy later. Carnot´s principle:

"*the motive power of heat is independent of the agents employed to realize it; its quantity is fixed solely by the temperatures of the bodies between which is effected, finally, the transfer of the caloric*"

Thus, with the contribution of Clapeyron, the last idea could be written as follows:

$$\eta_{rev} = \frac{\partial W}{\partial Q} = \frac{T}{C(T)} \tag{1.1}$$

where η_{rev} is the efficiency of a reversible engine, T is the temperature, and $C(T)$ is a function of T (proposed by Clapeyron from the idea of Carnot), and W and Q are the work and heat produced and consumed, respectively.

Then, in his fourth memoir (Clausius, 1856), Clausius stated that if the process is reversible, "the transformations which occur must exactly cancel each other, so that their algebraical sum is zero". Clausius defined the transformation value as N, as follows:

$$N = \oint \frac{\partial Q}{T} = 0 \tag{1.2}$$

Later in 1865, in his ninth memoir(Clausius, 1879), Clausius established his famous inequality, extending the aforementioned idea to either case, reversible or not, where the sum of the transformations for cyclical processes can only be negative or equal to zero [1], as follows:

$$N = \oint \frac{\partial Q}{T} \leq 0 \tag{1.3}$$

where N is the transformation value, Q the heat transfer rate, and T the temperature.

[1]Considering that the heat that leaves the system from a thermal reservoir is positive and, analogously, the heat that enters to the system from a thermal reservoir is positive.

In addition to that, Clausius defines one of the most important concept in thermodynamics and the manner in which the science sees the universe.

On his ninth memoir N was baptized by Clausius as Entropy, and defined with the symbol "S", as seen below:

$$S = \oint \frac{\partial Q}{T} \leq 0 \tag{1.4}$$

$$dS = \frac{\partial Q}{T} \tag{1.5}$$

For the construction of the concept, Clausius took the Greek word "$\tau\rho o\pi\eta$"($trope$), which means transform, and combined it with the syllable "en". Alluding to the fact that entropy means transformational content. Likewise, he argued that the choice of the syllable "en" was made deliberately to maintain the proximity between the concepts of energy and entropy, and consequently, creating an alliteration between both concepts(Clausius, 1879).

Finally, realizing the impact of his discovery, Clausius closes his work with the following two statements.

- The energy of the universe is constant.
- The entropy of the universe tends to a maximum

After the development of the second law of thermodynamics and its modifications as we know it today, several studies appeared focusing on the manifestations that entropy can have depending on the transport phenomenon to be studied (Moran, 1989). In the 70's, from the economic crisis several authors encouraged their efforts to increase the efficiency of the processes, optimizing the design of systems in order to take the maximum benefits of the limited fuel sources (Moran and Sciubba, 1994; Bejan, 2002). In the following 20 years, assisted by the growing computational and technological capacity of the time, the scientific community set out to modify the traditional energy based analysis giving way to the study of entropy generation at local scale.

Although an energy analysis based only on the first law of thermodynamics allows to determine the performance of a system with respect to the energy inputs which it receives, the first law efficiency can be misleading in some cases (Dincer and Rosen, 2012). The first-law efficiency hides important information about how close the analyzed system is to the ideal (reversible) case. On the other hand, the second law allows us to know how the system generates inefficiencies and which regions are responsible for the energy degradation(Bejan, 2013).

Therefore, it is important to have the theoretical support to determine the generation of entropy in its different generation mechanisms. Given the complexity of energy generation, storage and distribution systems today, it is usual have more than one generation mechanism occurring simultaneously. Furthermore, with the advent of advanced data management and simulation technologies, there exists adequate computational capability to carry out first and second law analysis on a differential scale.

Accordingly, this document presents the study and development of an expression to determine the generation of entropy at a local scale in porous media, under non-thermal equilibrium considering laminar and turbulent regimes.

The expression and methodology developed in this work, provides the possibility to study and determine computationally the entropy generation and its spatial distribution in systems which exchange, manage and store energy through porous structures. These structures have a wide spectrum of applications in concentrating solar systems, thermal energy storage and hydrogen generation systems, among others.

1.2 Porous Media Applied to Engineering

The transport phenomena between a solid porous matrix and fluid or multiphase fluid mixtures have been an active research subject during the last 70 years (Ávila-Marín, 2011; Ergun and Orning, 1949; Vafai, 2015) due to their large capacity to exchange and store thermal energy (Kalita and Dass, 2011; Calderón-Vásquez et al., 2021). The first interest in the literature was focused on heat exchange devices and their applications as reacting and/or filtering media (Baumann et al., 2020); however, particularly during the last 20 years, several authors have proposed novel technological solutions for energy conversion and storage systems, such as hydrogen reactors, and concentrated solar power (CSP) systems (Ávila-Marín, 2011; Kribus et al., 1996; Kun-Can et al., 2017; Villafán-Vidales et al., 2011; Wu and Yu, 2007; Wu et al., 2010; Xu et al., 2011; Younis and Viskanta, 1993). Likewise, due to the expansion of CSP systems during the last years, porous heat exchangers have been proposed as an interesting solution to increase the operating temperatures of solar tower systems using volumetric receivers. The main idea is to increase the maximum temperature of the working fluid in the solar receiver, enabling the possibility of achieving higher overall conversion efficiencies. Currently, the operation of commercial central receiver CSP systems has a benchmark operating temperature of around 600 °C, established by the limit of chemical stability of the working fluid: molten nitrate salts (Ho and Iverson, 2014). In this context, some authors (Ávila-Marín, 2011) have proposed the use of compressible gases as working fluids in combination with a porous volumetric solar receiver (VSR) to increase the operating temperature to 1000-1200 °C and, consequently, increasing the conversion efficiencies to levels of around 50% (Ávila-Marín, 2011; Kribus et al., 2014). A similar idea has been proposed for thermal energy storage systems (TES) (Singh et al., 2019), using porous solid media as a sensible heat storage matrix in interaction with compressible gases. Nevertheless, the use of this kind of system implies dealing with several challenges in the design phase, mainly related to difficulties in the computational modelling stage to properly describe the transport phenomena in a complex solid porous matrix of mini- and microchannels.

Implementing a porous media either in a volumetric receiver or in a thermal storage system increases the heat exchanging area between the solid and the fluid; however, at the same time, the hydraulic resistance also increases significantly. Therefore, during the design process, it is necessary to consider a detailed analysis for determining the best configuration, material, and geometry of the porous media (i.e., ceramic foam, wire mesh, packed bed, among others.), aiming to maximize the benefits of the porous morphology. In the same

direction, it is necessary to have a figure of merit able to consider the trade-off of the disadvantages and benefits in the same analysis. With this goal, some authors have proposed different approaches for assessing different materials, geometries, and designs in terms of heat exchange capacity and/or hydraulic resistance (Ávila-Marín et al., 2019; Bai, 2010; Hischier et al., 2012; Wu et al., 2011a), showing promising results in terms of VSR technology. In 2012, Hischier et al. (Hischier et al., 2012) presented a complete analysis methodology, which defined two parameters of thermal efficiency for the concentrating and absorbing systems, respectively. Later, the authors evaluated them for several operating configurations. Their results report thermal efficiencies of 90% and outlet air temperatures of 1273 K for the configuration that minimizes thermal losses. From this result, it should be interesting to extend the decision criteria and include the concept of energy quality, as stated by the second law of thermodynamics, in the decision parameter the influence of the fluid temperature. A second-law analysis offers the possibility, through the entropy generation concept, to compute the irreversibilities, expressed as thermal losses and pressure drop, and the quality of the energy dispatched in terms of the outlet temperature. In 2014, Kribus et al. (Kribus et al., 2014) presented a complete review of the modeling methods and available correlations for VSR systems, considering radiative, convective, and conductive heat transfer, and pressure drop across the absorber. Nevertheless, despite the evidenced progress, the assessments still present significant discrepancies regarding the behavior of porous systems and the heat transfer capacity of porous systems. In their analysis, the authors concluded that some convective heat transfer results do not match or overestimate the heat transfer capacity of porous foams, hindering the design process and comparison with other technological proposals. Finally, the authors state that an additional effort is still required in the specification of material and design approaches for building structures that reach reliable high operating temperatures and conversion efficiencies. Therefore, developing a figure of merit, coupled with a detailed methodology for assessing the design of VSR systems would be significantly useful. The present study aims to describe the potential use of local entropy generation (LEG) as a metric to evaluate the performance of porous media systems, integrating thermodynamic costs in one single parameter and the loss of useful energy potential (Bejan, 1995). Through the use of entropy generation as a metric it is possible to assess the irreversibilities generated by the transport phenomena (mass, momentum, and energy) and, at the same time, to distinguish the best design option in terms of the quality of energy (Sarmiento-Laurel et al., 2019). Thus, the proposed analysis of entropy generation offers additional information on the internal conversion processes and the rationale use of the energy resources (Bejan, 1995; Sarmiento-Laurel et al., 2019).

1.3 Entropy Generation in the Literature

The concept of entropy generation has been widely discussed in the last 40 years (Bejan, 1980; Sciacovelli et al., 2015), and it has recently received a special emphasis due to the need for increasing the exchange and conversion efficiencies in energy systems (Sciacovelli et al., 2015). However, despite the potential of entropy generation as a development parameter on design and optimization (Han et al., 2021; Liu et al., 2021; Song and Liu, 2018), most of the entropy generation analyses have focused on large or medium-scale systems (such as power plants or their components) (see Figure 1.1). On the other hand, the differential-

scale for Computational Fluid Dynamics (CFD) analyses is limited mainly to the first law of thermodynamics, focusing on the energy losses such as pressure drop and thermal losses. However, some authors have conducted interesting studies regarding entropy generation on

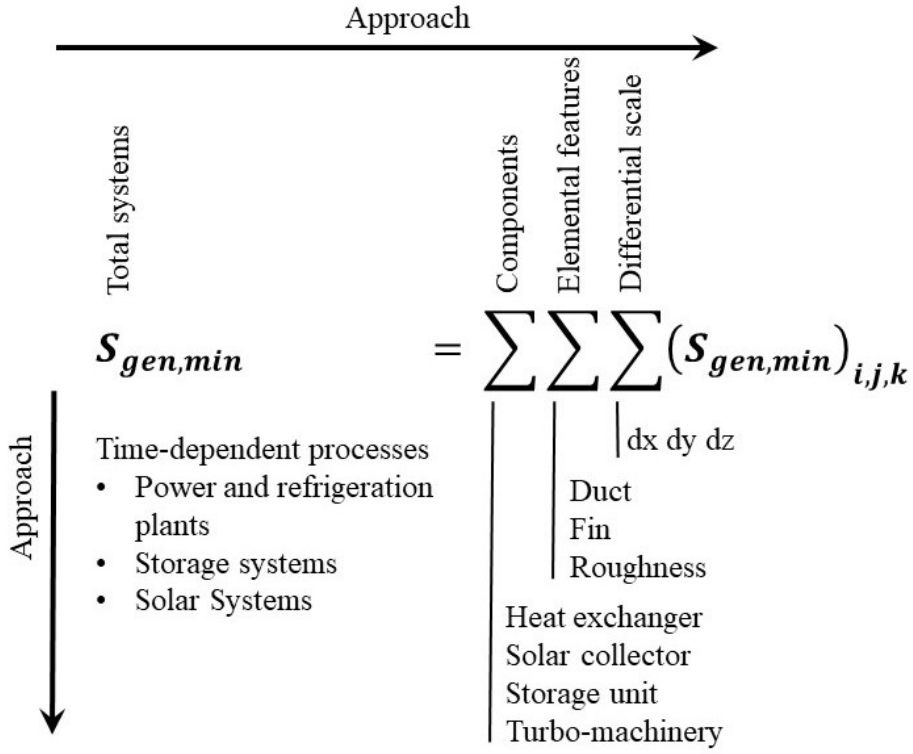

Figure 1.1: The two-dimensional structure of the field of entropy generation minimization (Adapted from (Bejan, 2013)).

micro and nano scales applied to heat transfer in porous media (Betchen and Straatman, 2008; Mahian et al., 2013; Torabi et al., 2019).

In 2008, Betchen and Straatman (2008) developed an entropy generation function for nonthermal equilibrium (NTE) heat transfer in high-conductivity foams using a volume-average scope in transport equations (Quintard and Whitaker, 1994). The proposed model offers an appropriate theoretical expression for the viscous dissipation entropy generation through high conductivity foams in several realistic applications, opening pathways for novel conceptual proposals. Although the analysis of Betchen and Straatman proposes a theoretical expression for LEG in a porous foam, the results reported are restricted to laminar regimes. In addition to that, and despite their considerations, the final entropy model does not include a practical expression to determine the LEG by turbulent dissipation in terms of available turbulence models (k-ε, k-ω SST, etc.) (Wilcox, 2006). Usually, viscous dissipation effects are neglected since they do not significantly affect the entropy generation in comparison to the heat transfer. However, turbulence has indeed an impact on the mixing and advection of heat during the exchange process.

Mahian et al. (2013) reviewed the state of the art in entropy analysis for nanofluid applications, reporting several contributions in the literature regarding differential-scale entropy analysis. The authors stated the importance of suitable relations to calculate the thermophysical

properties because, in some cases, different thermophysical models could produce opposite predictions for the entropy generation. In 2010, Feng and Kleinstreuer (2010) presented a heat transfer analysis on parallel disc systems, using nano-fluids under laminar flow regimes. The analysis considers the entropy generation as a figure of merit, showing a comparison between the entropy generation due to viscous effects and the heat transfer, recognizing the design configurations where the viscous dissipation is negligible against the entropy variation due to heat transfer. In the same way, in 2011, Moghaddami et al. (2011) presented a second law analysis on nano fluid flows through a circular pipe under laminar and turbulent regimes, varying the volume fraction of particles. The authors distinguished the dominant entropy generation mechanisms and defined the optimal design in each flow configuration.

Later in 2014, from their previous research work on LEG in porous foams (Betchen and Straatman, 2008), Betchen and Straatman (2014) conducted a pore-scale CFD analysis of high-conductivity foam heat exchangers. The analysis defines some recommendable pore geometries to maximize the heat exchange capacity by minimizing the entropy generation. Furthermore, in 2015, based on Betchen and Straatman's entropy generation model (Betchen and Straatman, 2008), Ting et al. (2015) presented a numerical analysis of nanofluid flow through porous media, focused on studying the relevance of viscous dissipation in modeling entropy generation. The authors concluded that neglecting the viscous dissipation effects in the analysis overestimates in 10% the fluid friction irreversibilities and significantly underestimates the heat transfer irreversibilities, concluding that it is relevant to consider this effect to ensure the accuracy of the results. Recently, in 2019, Torabi et al. (2019) presented a numerical analysis of entropy generation in porous media at the pore scale. From the results, the authors show the impact on the heat exchange capacity of the porous media in terms of the diameter and shape of the pores under high Reynolds configurations. A RANS model was implemented, based on the proposals of Kock and Herwig (2004, 2005) to determine the viscous entropy generation in terms of the outlet parameters of viscous dissipation and turbulent kinetic energy (TKE) of k-ε and k-ω turbulence models (Wilcox, 2006).

In 2005, Kock and Herwig (2005) presented a numerical model to link turbulence models such as k-ε and k-ω (Wilcox, 2006) to the theoretical expression of entropy generation defined by Bejan (2013).

From the above, an analysis using the LEG offers advantages on the optimization and CFD design task, in comparison to the commonly used pressure drop and heat transfer performance analysis. In that regard, an entropy generation analysis is an excellent assessing tool able to consider the trade-off between the benefit of the high heat-exchanging area of porous heat exchange systems, and the thermodynamic costs of pressure drop produced by the presence of the solid matrix. Nevertheless, despite the extensive study in the literature on second law analysis, it is necessary a LEG model able to determine the entropy generation and its generation mechanisms in fluid flows through a porous matrix, from low to high Reynolds regimes. In that sense, encouraged by the wide field of applications of porous media (CSP VSR, TES, and hydrogen generation systems), and the advantages of the LEG as a figure of merit stated in the literature, the present work describes an assessment methodology for the design and optimization of heat exchange porous media systems. The proposed model allows for determining the LEG for different entropy generation mechanisms (heat exchange and viscous dissipation) from high to low Reynolds regimes. The methodology determines the LEG as a post-process result from the solutions of continuity, momentum, and energy

equations, without the need of solving an additional transport entropy equation per se.

Although some authors have analyzed the generation of entropy in porous heat exchange devices (Betchen and Straatman, 2014; Torabi et al., 2017, 2019), the analyzes were performed on a specific geometry of spherical or oval pores at pore-scale limiting the impact of the results under one or two types of porous geometry. Currently, several porous geometries have been proposed in the literature, such as ceramic and metal foams (Capuano et al., 2016; Pabst et al., 2017; Wu et al., 2011a, 2010), packed wire mesh (Avila-Marin et al., 2018, 2019), packed bed of rock or solid spheres (Spelling et al., 2012), and mineral wool (Fend et al., 2004a), among others. Therefore, the proposed model is designed at a macroscopic scale based on the volume averaging method (Quintard and Whitaker, 1994), with the objective of simplifying the numerical task and opening the analysis to any available geometry. Furthermore, based on the proposal of Kock and Herwig (2004), the generation of turbulent viscous dissipation entropy was determined by the available RANS turbulence models, by adapting the local entropy model to the available turbulence model developed for porous media by Nakayama and Kawahara (1999), Pedras and de Lemos (2001), and Teruel and Rizwan-uddin (2009b,a). Finally, the heat exchange of a Newtonian fluid through a porous medium is numerically analyzed to identify the scope of the local entropy model.

Summarizing the information presented in the literature review, Tab 1.1: shows the most relevant articles in the state of the art. This is a selection of articles that helped to direct the development of the methodology proposed in this investigation.

Table 1.1: Relevant articles for the investigation

Contribution to this research	**Reference**
Main guidelines on the theoretical development of entropy generation at differential scale.	Bejan (2013)
Volume averaging methodology on transport equations in porous media.	Quintard and Whitaker (1994)
Theory on the transport phenomena in porous media under turbulent regimes. Development of a k-epsilon-based turbulence model adapted to porous media, through volume averaging method over Reynolds (RANS) time-averaged equations.	Pedras and de Lemos (2001) de Lemos (2012)
Develop an expression for the entropy generation rate from k and epsilon CFD results under turbulent regimes in internal flows.	Kock and Herwig (2004, 2005)
Theoretical and dimensionless analysis of entropy generation in porous media.	Betchen and Straatman (2008)

1.4 Hypothesis and objectives

1.4.1 Hypothesis

It is possible to establish a physical-mathematical model to study the LEG rate and entropy transport in porous media. The distribution of the LEG rate can be studied through different generation mechanisms under turbulent and laminar regimes.

To demonstrate the principal hypothesis, the following specific hypotheses are considered.

- The LEG mechanisms in porous media of viscous dissipation and heat transfer can be described in terms of the turbulent kinetic energy (TKE) k and the TKE dissipation rate ε from a macroscopic scaled $k-\varepsilon$ turbulence model, and the macroscopic interaction parameters about volumetric heat transfer and drag surface forces between the solid matrix and the fluid.
- The LEG rate of thermal conduction and viscous dissipation, related to time fluctuations of temperature and velocity in a porous medium, can be determined by macroscopic turbulent effects modeled in the macroscopic scaled $k-\varepsilon$ turbulence model.

1.4.2 General Objective

Apply a novel methodology for the study of the local entropy generation and its spatial distribution in porous media, distinguishing its different generation mechanisms from high to low Reynolds regimes.

1.4.3 Specific Objectives

- Develop a physical-mathematical expression for macroscopic entropy transport in porous media by the spatial-time averaging method.
- Define an empirical relationship to determine the LEG rate in porous media from the vectorial and scalar results of temperature, velocity, TKE, and ε.
- Develop a CFD solver to model the LEG rate for porous media in OpenFoam.
- Study the spatial distribution and numerical significance of the LEG rate separated by generation mechanisms.

1.5 Overview of contributions

The main contributions of this work are as follows.

- Develop a macroscopic expression of LEG for porous media under laminar and turbulent flow regimes, considering nonthermal equilibrium.
- Define a methodology to determine the LEG mechanisms from the CFD scalar and vectorial results (temperature, velocity, TKE, and ε).
- Analyze the LEG distribution and compare its different generation mechanisms through a numerical experiment applied to a porous channel, considering different porosities, temperature differences, and Reynolds regimes.

The content presented in this doctoral research conforms to the results presented in a conference article (Sarmiento-Laurel et al., 2019), and a journal article in "Engineering Applications of Computational Fluid Mechanics" (Sarmiento-Laurel et al., 2022), and the development of a computational CFD simulation tool for OpenFOAM V9 (2021) for analyzing local entropy generation in a porous medium.

The first article (Sarmiento-Laurel et al., 2019) shows an energy-based analysis on a porous VSR and the influence of the porous geometry and the solid material on the device performance. Likewise, the usual way to evaluate the performance of a porous heat exchanger is discussed, concluding that it is insufficient to employ an analysis based on the heat transfer rate and the pressure drop separately, as it is usual in the literature. Despite the fact that these parameters of interest are relevant to performance, it is difficult to account for their impact on a single objective function, furthermore, there is no clarity about the quality of the energy exchanged and the degradation of its energy potential.

Unlike an energy-based analysis, a second law analysis can make a distinction about the quality of the energy exchanged by the device from the temperature associated with each heat flow in a porous medium. From this reflection on a VSR as a porous heat exchanger, the second part of the doctoral research was directed on the study of the transport equations and simulation methodologies in porous media, to develop an expression for the transport and generation rate of entropy at a local scale and the additional effects related to the presence of a porous matrix.

Thus, the depth analysis of the LEG in porous media constitutes the results presented in the journal "Engineering Applications of Computational Fluid Mechanics" (Sarmiento-Laurel et al., 2022). Through the model developed, the analysis of entropy transport and LEG, it is possible to account for the additional irreversibilities associated with the presence of the porous medium (volumetric heat transfer and hydraulic resistance) in a single equation. Likewise, the impact of weight that each LEG mechanism has on the generation of entropy on a global scale is evaluated.

Chapter 2 shows a review of the governing equations of transport phenomena in porous media and a volume-averaging methodology to analyze them. Chapter 3 shows a preliminary 1D energy analysis of a porous heat exchanger, Chapter 4 presents a physical-mathematical development of an expression for the local entropy transport and entropy generation rate in porous media. In addition, Chapter 4 shows a methodology for determining the LEG rate for turbulence regimes. Chapter 5 presents a study case for the proposed entropy model implemented in a CFD solver on OpenFOAM (OpenFOAM V9, 2021).Finally, the conclusions are presented in Chapter 6.

Chapter 2

Transport phenomena in porous media

In order to study the transport phenomena in a porous medium, Chapter 2 presents the conservation equations and the methodology reported in the literature to model the spatial dispersion of the thermophysical properties. Finally, the expression of energy transport is determined at the macroscopic scale.

Two strategies are defined to study the transport phenomena in porous structures, which depend on the characteristic scale of the problem (Kaviany, 1999). The first, the pore-scale scope, consists in studying the interactions between the fluid and solid phase as a large matrix of channels (see Figure 2.1). The pore-scale analysis offers a complete and detailed view of the differential scale of the specific solid-fluid interactions of mass, momentum, and energy over the pore surface. Nevertheless, the high computational cost restricts the applicability of the analysis for larger components or devices.

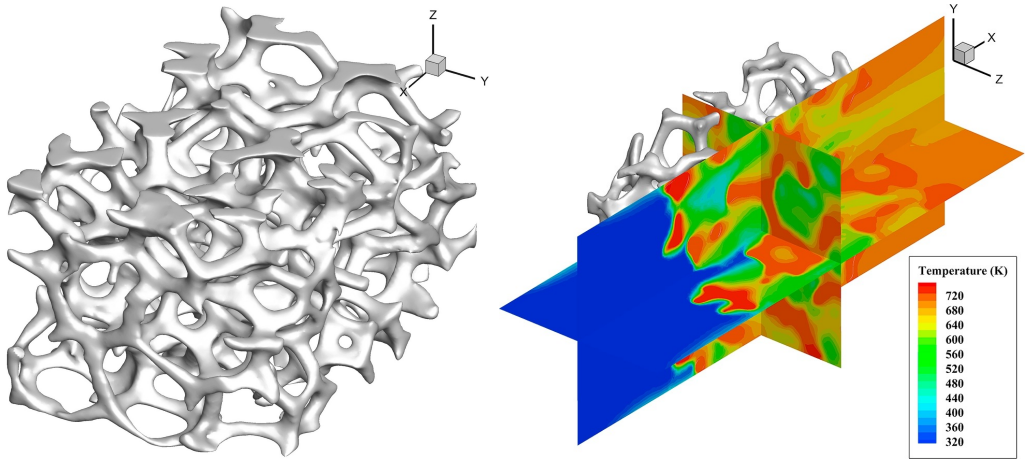

Figure 2.1: Temperature field of a porous media at the pore-scale. Reprinted from (Du et al., 2017), Copyright (2023), with permission from the Journal Energy, Elsevier.

Figure 2.1 shows an example of pore-scale analysis, where the solid matrix is studied in detail, considering every micro channel inside the porous matrix. There, a solid matrix was obtained using X-ray computed tomography of a real porous media. Then the structure is

processed to reduce the number of 3D faces. Finally, the space between the pores is processed for mesh generation.

On the other hand, the second strategy proposes modeling the solid matrix effects as macroscopic field effects over a fluid flow, such as hydraulic resistance and volumetric heat transfer. The macro-scale analysis considers a minimum characteristic length small enough to consider a discrete number of pores and its drag effect as a volumetric phenomenon, assuming the discrete number of pores as a continuum. Thus, as shown in Figure 2.2, the results are presented for solid and fluid phases as two continuous medias where it is not possible to distinguish the pores or solid-fluid boundaries. The presence effects of the solid matrix are simulated as field phenomena in the fluid phase. Figure 2.2 shows the temperature field for solid and fluid phases in a volumetric receiver of concentrated solar energy. Concentrated radiation enters from the left side and passes through the solid medium until it is extinguished as it moves to the right. At the same time, a stream of ambient air enters from the left, increasing its temperature upstream.

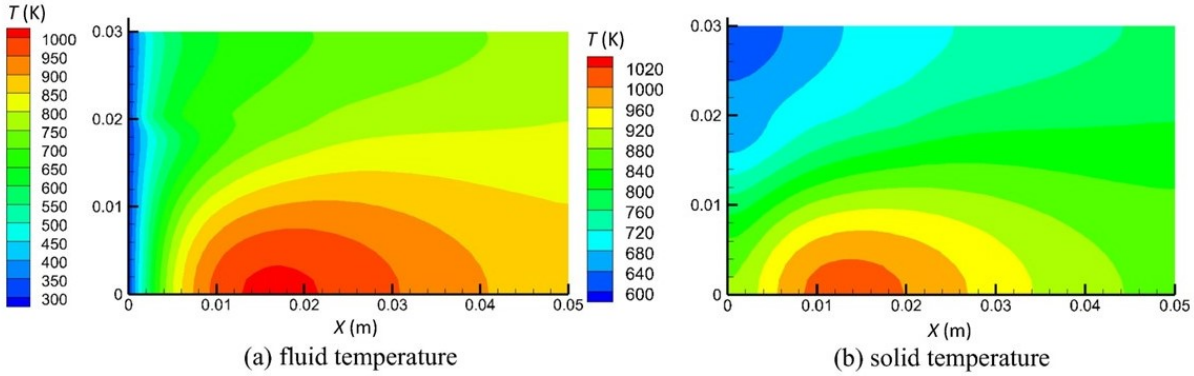

(a) fluid temperature (b) solid temperature

Figure 2.2: Temperature field of a porous media considering a macro-scale analysis. Reprinted from (Chen et al., 2017), Copyright (2023), with permission from International Journal Energy Conversion and Management, Elsevier.

2.1 Volume Averaging Method

In a similar form to the time-average proposed by Reynolds in 1895 (Reynolds, 1895), the macroscopic analysis considers a Representative Elementary Volume (REV) as the minimum volume of the analysis presented by Slattery (1967) and Whitaker (1969, 1998). Figure 2.3 shows the spatial dispersion of the property φ in a REV. The property φ is separated in a volume-average of φ in the REV and fluctuations from the average, as follows.

$$\langle \varphi \rangle^V = \frac{1}{\Delta V} \int_{\Delta V} \varphi \mathrm{d}V \tag{2.1}$$

$$\bar{\varphi} = \frac{1}{\Delta t} \int_{\Delta t} \varphi \mathrm{d}\tau \tag{2.2}$$

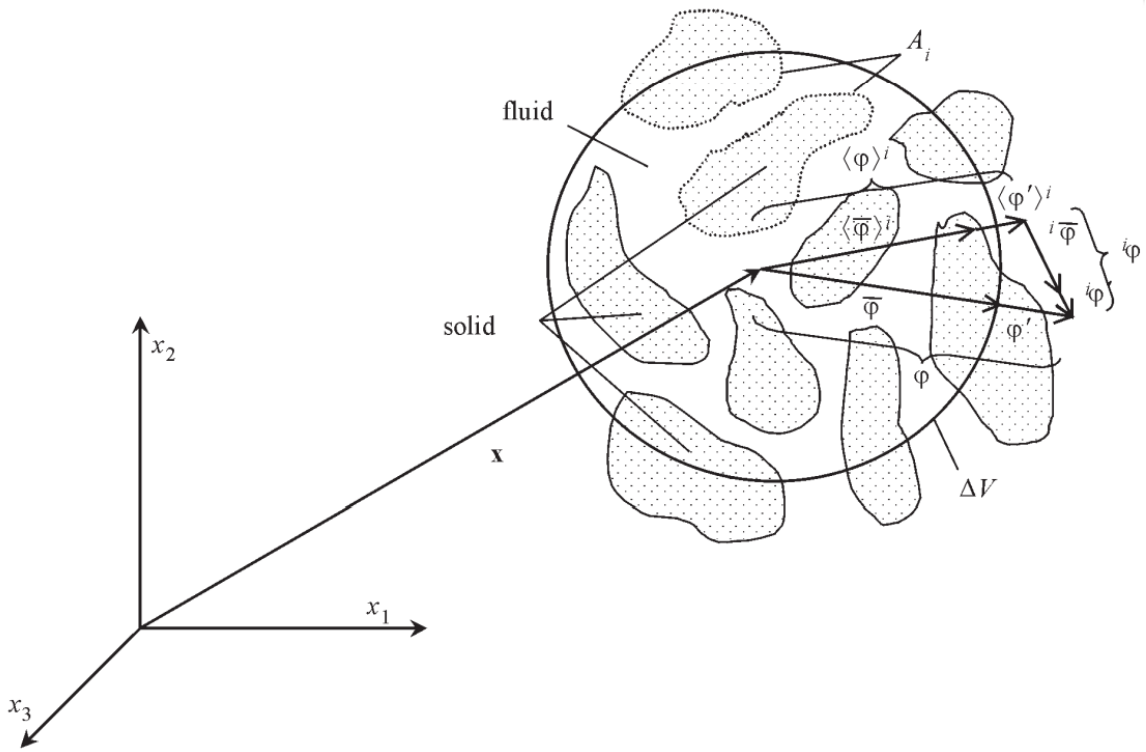

Figure 2.3: Variation of a property in a Representative Elementary Volume (REV). Reprinted from (de Lemos, 2012), Copyright (2023), with permission from International Journal of Heat and Mass Transfer, Elsevier.

where φ is an auxiliary property, $\langle\varphi\rangle^V$ is the average value of φ at any point inside of a representative elementary volume of size ΔV and analogously, $\bar{\varphi}$ is the average value in a time interval of Δt. Then the value of $\langle\varphi_f\rangle^V$ is related to the intrinsic average for the fluid phase $\langle\varphi_f\rangle^i$ as follows.

$$\langle\varphi_f\rangle^v = \phi\langle\varphi_f\rangle^i \tag{2.3}$$

where ϕ is the porosity, considering a mean local value of porosity. Nevertheless, in a more accurate analysis is possible include the spatial dispersion of the porosity.

Then, the volume decomposition of φ (Hsu and Cheng, 1990; Quintard and Whitaker, 1994; de Lemos, 2012) is expressed as follows:

$$\varphi = \langle\varphi\rangle^i + {}^i\varphi \tag{2.4}$$

where ${}^i\varphi$ is the spatial deviation of φ.

In addition, for deriving operators (Howes and Whitaker, 1985; de Lemos, 2012) presents the following relationship to consider the flow of a property between phases, as heat or surface forces.

$$\left\langle \frac{\partial}{\partial x_i}(\varphi) \right\rangle^V = \frac{\partial}{\partial x_i}\left(\phi\langle\varphi\rangle^i\right) + \frac{1}{\Delta V}\int_{A_i} \boldsymbol{n}\varphi ds_i \tag{2.5}$$

$$\left\langle \frac{\partial \varphi_k}{\partial x_k} \right\rangle^V = \frac{\partial}{\partial x_k}\left(\phi\langle\varphi_k\rangle^i\right) + \frac{1}{\Delta V}\int_{A_i} \boldsymbol{n}\cdot\varphi ds_i \tag{2.6}$$

where $\mathbf{n}$ is the unitary normal vector, and u_i the velocity phase to the interfacial area A_i between the fluid and the solid phases.

2.1.1 Time-average and spatial-average

To take into account the turbulent effects in porous media de Lemos proposes a double decomposition in space and time as follows (de Lemos, 2012).

$$\varphi = \langle \overline{\varphi} + \varphi' \rangle^i + {}^i(\overline{\varphi} + \varphi') \tag{2.7}$$

then,

$$\varphi = \langle \overline{\varphi} \rangle^i + \langle \varphi' \rangle^i + {}^i\overline{\varphi} + {}^i\varphi' \tag{2.8}$$

where $\langle \overline{\varphi} \rangle^i$ is the time and volume-averaged φ, $\langle \varphi' \rangle^i$ is the volume average of the time fluctuation of φ, ${}^i\overline{\varphi}$ is the volume deviation of the time average of φ, and ${}^i\varphi'$ is the volume deviation of the time fluctuation of φ.

Finally, as it was established by Pedras and de Lemos (2001), both averaging operators (time and spatial) are independent among them (Commutative property). Therefore, the order of application of these does not modify the resulting equation or property, as follows.

Thus,

$$\begin{aligned} \overline{\langle \varphi \rangle^V}(x,t) &= \frac{1}{\Delta t} \int_{\Delta t} \left(\frac{1}{\Delta V} \int_{\Delta V} \varphi \mathrm{d}V \right) \mathrm{d}\tau \\ &= \frac{1}{\Delta V} \int_{\Delta V} \left(\frac{1}{\Delta t} \int_{\Delta t} \varphi \mathrm{d}\tau \right) \mathrm{d}V = \langle \bar{\varphi} \rangle^V(x,t) \end{aligned} \tag{2.9}$$

Through Eq.(2.8) and (2.9), the spatial and temporal fluctuations of advected a property in a porous medium can be separated and analyzed independently. This method is applied later in Chapter 3 for the entropy transport equation, to define an expression linking the local-scale entropy generation with the effect of spatial deviations and time fluctuation.

2.2 Transport equations for mass, momentum, and energy

In order to analyze the entropy transport in porous media, first it is necessary conduct a detailed study of the conservation equations of mass, momentum, and energy. In the following sections, the transport equations are developed from their general expression. Then, the volume-averaging method is applied step by step to conclude in the analysis of entropy transport and, in consequence, finish in an expression for the volume-averaged entropy transport equation.

2.2.1 Continuity and Momentum equations

The momentum and mass conservation equations below, are a result of applying the volume-averaging method to an isotropic porous medium. There, the properties are presented through the volume-average $\langle\varphi_f\rangle^i$ described in equation Eq.(2.3). The momentum conservation equation considers two additional terms to model the hydraulic resistance that the solid matrix exerts on the fluid. In these two terms (Eq.(2.11)), are accounted the interaction and exchange of momentum between the solid and fluid phases through the shear and pressure stresses (associated with the drag forces).

Taking the conservation equations of mass and momentum using the constitutive equation for Newtonian fluids (de Lemos, 2012; Kaviany, 1999), and applying the volume average, the macroscopic conservation equations are defined as follows:

$$\frac{\partial \rho_f}{\partial t} + \rho_f \frac{\partial}{\partial x_k}\Big(\phi \langle u_k\rangle^i\Big) = 0 \tag{2.10}$$

$$\begin{aligned}
&\frac{\partial\left(\rho_f \phi \langle u_j\rangle^i\right)}{\partial t} + \rho_f \frac{\partial}{\partial x_k}\left(\phi \langle u_j u_k\rangle^i\right) \\
&\quad = \frac{\partial}{\partial x_i}\left(-\phi\langle P\rangle^i \delta_{ij} + \phi\mu\left(\frac{\partial\langle u_i\rangle^i}{\partial x_j} + \frac{\partial\langle u_j\rangle^i}{\partial x_i}\right)\right. \\
&\qquad \left. - \frac{2}{3}\phi\mu\left(\delta_{ij}\frac{\partial\langle u_k\rangle^i}{\partial x_k}\right)\right) \\
&\qquad + \underbrace{\frac{\mu}{\Delta V}\int_{A_i}\left(\left(\frac{\partial u_i}{\partial x_j} + \frac{\partial u_j}{\partial x_i}\right) - \frac{2}{3}\left(\delta_{ij}\frac{\partial u_k}{\partial x_k}\right)\right)\cdot \boldsymbol{n} ds_i}_{\text{Darcy HR}} \\
&\qquad \underbrace{- \frac{1}{\Delta V}\int_{A_i} P\boldsymbol{n} ds_i}_{\text{Forchheimer HR}}
\end{aligned} \tag{2.11}$$

where ρ_f is the fluid density, u the velocity, ϕ the porosity, P the time-averaged fluid pressure and μ the fluid viscosity.

The last two terms of the right-hand side in Eq.(2.11) derive from the Eq.(2.5) and Eq.(2.6) applied to both surface force terms, pressure, and viscous shear stress. They represent the interaction between the fluid with the solid matrix as a drag force. They are commonly defined as the Darcy-Forchheimer's hydrodynamic resistance terms (Pedras and de Lemos, 2001), and are expressed as R as follows:

$$\begin{aligned}
R &= \underbrace{\frac{\mu}{\Delta V}\int_{A_i}\left(\left(\frac{\partial u_i}{\partial x_j} + \frac{\partial u_j}{\partial x_i}\right) - \frac{2}{3}\left(\delta_{ij}\frac{\partial u_k}{\partial x_k}\right)\right)\cdot \boldsymbol{n} ds_i}_{\text{Darcy HR}} - \underbrace{\frac{1}{\Delta V}\int_{A_i} P\boldsymbol{n} ds_i}_{\text{Forchheimer HR}} \\
&= \phi\left(\frac{\mu_f}{k_1} u_D + \frac{\rho_f}{k_2}|u_D| u_D\right)
\end{aligned} \tag{2.12}$$

The last two terms in Eq.(2.12) are determined experimentally, considering the darcian velocity vector $u_D = \phi\langle u_j\rangle^i$, where k_1 (m^{-1}) and k_2 (m^{-2}) are correlation constants.

2.2.2 Energy equation

The first step to analyze the entropy generation is to study the complete expression of the energy transport equation in a control volume at the differential scale. Therefore, this section shows the mathematical development for an energy transport equation in porous media, and the additional terms that arise from the interaction of the solid and liquid phases (Currie, 2016; Cohen and Kundu, 2004).

Below is the energy transport considering the total energy per unit mass (kinetic plus internal), the heat rate, and the total work done by the surface forces $\frac{\partial}{\partial x_i}(u_j\sigma_{ij})$.

$$\begin{aligned}\frac{\partial}{\partial t}\left(\rho_f e + \frac{1}{2}\rho_f u_j u_j\right) + \frac{\partial}{\partial x_k}\left(\left(\rho_f e + \frac{1}{2}\rho_f u_j u_j\right)u_k\right)\\ = \frac{\partial}{\partial x_i}(u_j\sigma_{ij}) + u_j\rho_f f_j - \frac{\partial q_j}{\partial x_j}\end{aligned} \tag{2.13}$$

where e is the fluid internal energy per unit of mass, σ_{ij} the surface forces tensor, f_j the mass forces vector and, q_j net the heat flux.

Expanding and regrouping the left-hand side terms in Eq. (2.13) (see the complete mathematical development in Annex (A.1), it holds,

$$\begin{aligned}\rho_f\left[\left(\frac{\partial}{\partial t}(e) + \frac{\partial}{\partial x_k}(e)u_k\right) + \left(u_j\frac{\partial}{\partial t}(u_j) + \frac{\partial}{\partial x_k}(u_j)u_j u_k\right)\right]\\ = u_j\frac{\partial}{\partial x_i}(\sigma_{ij}) + \sigma_{ij}\frac{\partial}{\partial x_i}(u_j) + u_j\rho_f f_j - \frac{\partial q_j}{\partial x_j}\end{aligned} \tag{2.14}$$

Therefore, by applying space-averaging $\langle\rangle^v$ in Eq.(2.14), the following expression holds,

$$\begin{aligned}\rho_f\left[\left(\frac{\partial}{\partial t}\left(\phi\langle e\rangle^i\right) + \phi\left\langle\frac{\partial}{\partial x_k}(e)u_k\right\rangle^i\right)\right.\\ \left. + \phi\left\langle\left(u_j\frac{\partial}{\partial t}(u_j) + \frac{\partial}{\partial x_k}(u_j)u_j u_k\right)\right\rangle^i\right]\\ = \left\langle u_j\frac{\partial}{\partial x_i}(\sigma_{ij})\right\rangle^V + \phi\left\langle\sigma_{ij}\frac{\partial}{\partial x_i}(u_j)\right\rangle^i + \phi\langle u_j\rho_f f_j\rangle^i\\ - \left[\frac{\partial\left(\langle q_j\rangle^v\right)}{\partial x_j} + \frac{\partial}{\partial x_j}\left(\frac{1}{\Delta V}\int_{A_i}\boldsymbol{n}\lambda_f T_f ds_i\right)\right.\\ \left. + \frac{1}{\Delta V}\int_{A_i}\boldsymbol{n}\cdot\lambda_f\frac{\partial T_f}{\partial x_j}ds_i\right]\end{aligned} \tag{2.15}$$

where λ_f is fluid conductivity and T_f is fluid temperature. In addition, the last two terms on the right-side represent the local conduction between the solid and fluid phases, and the convective heat transfer between the solid and fluid, respectively.

Once the general expression for energy transport has been developed (Eq. (2.14)), the volume average method is applied to find out all the effects associated with the fluid-solid interaction in energy transport. After applying the spatial averages the exchange of energy and stresses between the solid and the fluid must be accounted for. Thus, from the first and fourth terms to the right of equation Eq. (2.14),emerge the terms associated with hydraulic resistance and volumetric heat exchange, respectively. Consequently, the items below present the mathematical development of the terms representing the trade between the solid and the fluid.

First, the term $\left\langle \frac{\partial}{\partial x_i}(\sigma_{ij}) \right\rangle^V$ is analyzed to develop the hydraulic resistance terms in detail. Expanding the first term of the right-hand side in Eq.(2.15), and applying the space-averaging $\langle\rangle^v$.

$$\left\langle u_j \frac{\partial}{\partial x_i}(\sigma_{ij}) \right\rangle^V = \phi \langle u_j \rangle^i \left\langle \frac{\partial}{\partial x_i}(\sigma_{ij}) \right\rangle^V + \phi \left\langle {}^i u_j \left(\frac{\partial}{\partial x_i}(\sigma_{ij}) \right) \right\rangle^i \tag{2.16}$$

Also, expanding the gradient of the surface forces tensor $\left\langle \frac{\partial}{\partial x_i}(\sigma_{ij}) \right\rangle^V$, as follows:

$$\begin{aligned}
&\left\langle \frac{\partial}{\partial x_i}(\sigma_{ij}) \right\rangle^V \\
&= \frac{\partial}{\partial x_i} \left(\phi \left\langle \left(-P\delta_{ij} + \mu \left(\frac{\partial u_i}{\partial x_j} + \frac{\partial u_j}{\partial x_i} \right) - \frac{2}{3}\mu \left(\delta_{ij} \frac{\partial u_k}{\partial x_k} \right) \right) \right\rangle^i \right) \\
&\quad + \underbrace{\frac{\mu}{\Delta V} \int_{A_i} \left(\left(\frac{\partial u_i}{\partial x_j} + \frac{\partial u_j}{\partial x_i} \right) - \frac{2}{3} \left(\delta_{ij} \frac{\partial u_k}{\partial x_k} \right) \right) \cdot \boldsymbol{n} ds_i}_{\text{Darcy HR}} \\
&\quad - \underbrace{\frac{1}{\Delta V} \int_{A_i} P \boldsymbol{n} ds_i}_{\text{Forchheimer HR}}
\end{aligned} \tag{2.17}$$

Then, the last two terms of the right-hand side in Eq.(2.17) are the Darcy-Forchheimer's hydrodynamic resistance terms. Darcy's term represents the shear stresses associated with the drag generated by the solid on the fluid in motion. On the other hand, the Forchheimer term represents the efforts associated with the forces perpendicular to the solid. Both terms multiplied by the fluid velocity $\langle u_j \rangle^i$, represent the loss of energy associated with the hydraulic resistance or, in other words, the useless work that the flow does against the porous matrix, generating irreversibilities. These two terms have great relevance in the LEG rate. So, they are written as follows:

$$\begin{aligned}
&\left\langle \frac{\partial}{\partial x_i}(\sigma_{ij}) \right\rangle^V \\
&= \frac{\partial}{\partial x_i} \left(-\phi \langle P \rangle^i \delta_{ij} + \phi\mu \left(\frac{\partial \langle u_i \rangle^i}{\partial x_j} + \frac{\partial \langle u_j \rangle^i}{\partial x_i} \right) \right. \\
&\quad \left. - \frac{2}{3}\phi\mu \left(\delta_{ij} \frac{\partial \langle u_k \rangle^i}{\partial x_k} \right) \right) + R
\end{aligned} \tag{2.18}$$

To obtain the complete expression of the surface forces tensor $\left\langle u_j \frac{\partial}{\partial x_i}(\sigma_{ij}) \right\rangle^V$, the Eq.(2.18) is included in Eq.(2.16), as follows:

$$\begin{aligned}
&\left\langle u_j \frac{\partial}{\partial x_i}(\sigma_{ij}) \right\rangle^V \\
&= \phi \langle u_j \rangle^i \frac{\partial}{\partial x_i} \left(-\phi \langle P \rangle^i \delta_{ij} + \phi\mu \left(\frac{\partial \langle u_i \rangle^i}{\partial x_j} + \frac{\partial \langle u_j \rangle^i}{\partial x_i} \right) \right. \\
&\quad \left. - \frac{2}{3}\phi\mu \left(\delta_{ij} \frac{\partial \langle u_k \rangle^i}{\partial x_k} \right) \right) \\
&\quad + \phi \langle u_j \rangle^i R + \phi \left\langle \left({}^i(u_j)^i \left(\frac{\partial}{\partial x_i}(\sigma_{ij}) \right) \right) \right\rangle^i \\
&= \phi \langle u_j \rangle^i \frac{\partial}{\partial x_i} \left(\phi \langle \sigma_{ij} \rangle^i \right) + \phi \langle u_j \rangle^i R \\
&\quad + \phi \left\langle \left({}^i(u_j)^i \left(\frac{\partial}{\partial x_i}(\sigma_{ij}) \right) \right) \right\rangle^i
\end{aligned} \tag{2.19}$$

Thus, introducing the extended surface forces tensor Eq.(2.19) into the energy transport Eq.(2.15),

$$\begin{aligned}
&\rho_f \left[\left(\frac{\partial}{\partial t} \left(\phi \langle e \rangle^i \right) + \phi \left\langle \frac{\partial}{\partial x_k}(e) u_k \right\rangle^i \right) \right. \\
&\quad \left. + \phi \left\langle \left(u_j \frac{\partial}{\partial t}(u_j) + \frac{\partial}{\partial x_k}(u_j) u_j u_k \right) \right\rangle^i \right] \\
&= \phi \langle u_j \rangle^i \frac{\partial}{\partial x_i} \left(\phi \langle \sigma_{ij} \rangle^i \right) \\
&\quad + \phi \langle u_j \rangle^i R + \phi \left\langle \left({}^i(u_j)^i \left(\frac{\partial}{\partial x_i}(\sigma_{ij}) \right) \right) \right\rangle^i \\
&\quad + \phi \left\langle \sigma_{ij} \frac{\partial}{\partial x_i}(u_j) \right\rangle^i + \phi \langle u_j \rho_f f_j \rangle^i \\
&\quad - \left[\frac{\partial \left(\langle q_j \rangle^v \right)}{\partial x_j} + \frac{\partial}{\partial x_j} \left(\frac{1}{\Delta V} \int_{A_i} \boldsymbol{n} \lambda_f T_f \, ds_i \right) \right. \\
&\quad \left. + \frac{1}{\Delta V} \int_{A_i} \boldsymbol{n} \cdot \lambda_f \frac{\partial T_f}{\partial x_j} \, ds_i \right]
\end{aligned} \tag{2.20}$$

Eq.(2.20) shows a general version of the energy transport in porous medium considering a macroscopic approach. There, the terms of energy exchange between both phases are presented, which represent the volumetric interaction of stresses and heat transfer between both phases. Additionally, it is possible to observe that the third and fourth terms on the left-hand side are canceled by the first and third terms on the right-hand side, since these

terms collectively amount to the product of u_j with the momentum equation (see annex (A.2)).

$$\begin{aligned}
&\rho_f \left[\left(\frac{\partial}{\partial t} \left(\phi \langle e \rangle^i \right) + \phi \left\langle \frac{\partial}{\partial x_k}(e) u_k \right\rangle^i \right) \right] \\
&= \phi \left\langle \sigma_{ij} \frac{\partial}{\partial x_i}(u_j) \right\rangle^i + \phi \langle u_j \rangle^i R \\
&\quad - \left[\frac{\partial \left(\langle q_j \rangle^v \right)}{\partial x_j} + \frac{\partial}{\partial x_j} \left(\frac{1}{\Delta V} \int_{A_i} \boldsymbol{n} \lambda_f T_f ds_i \right) \right. \\
&\quad \left. + \frac{1}{\Delta V} \int_{A_i} \boldsymbol{n} \cdot \left(\lambda_f \frac{\partial T_f}{\partial x_j} \right) ds_i \right]
\end{aligned} \tag{2.21}$$

The fourth and fifth terms on the right side correspond to the local conduction and volumetric heat transfer between the solid and fluid phases, respectively. In the literature, both heat transfer mechanisms are determined by computational simulations at the pore-scale, and in some cases experimentally (Kuwahara et al., 1996). The local conduction between each phase is determined as follows (de Lemos, 2012):

$$q_{sf,j} = \frac{1}{\Delta V} \int_{A_i} \boldsymbol{n} \lambda_f T_f ds_i = -\lambda_{fs} \frac{\partial \langle T_f \rangle^i}{\partial x_j} \tag{2.22}$$

where λ_{fs} is the local thermal conductivity tensor, usually determined by computational simulation at the pore-scale. For simplicity, the local conduction term is considered inside the heat transfer term $\langle q_j \rangle^v$ in the effective conductivity tensor, given by:

$$\lambda_{\text{eff},f} = \phi \lambda_f \delta_{ij} + \lambda_{fs} \tag{2.23}$$

On the other hand, the volumetric convective heat transfer is determined as a function of the temperature difference of each phase (Kaviany, 1999; Saito and de Lemos, 2005; de Lemos, 2012) as follows.

$$\frac{1}{\Delta V} \int_{A_i} \boldsymbol{n} \cdot \left(\lambda_f \frac{\partial T_f}{\partial x_j} \right) ds_i = h_i a_i \left(\langle T_f \rangle^i - \langle T_s \rangle^i \right) \tag{2.24}$$

where h_i is the interfacial convective heat transfer and a_i the surface area per unit of volume.

Usually, the volumetric convection heat transfer coefficient and the local thermal conductivity tensor are determined experimentally and depend on the geometrical distribution of the solid matrix (such as packed rock bed, ceramic foam, wire mesh, etc.).

Now, for simplicity, Eq.(2.21) is written as follows:

$$\begin{aligned}
&\rho_f \left[\left(\frac{\partial}{\partial t} \left(\phi \langle e \rangle^i \right) + \left\langle \frac{\partial}{\partial x_k}(e) u_k \right\rangle^i \right) \right] \\
&= \phi \left\langle \sigma_{ij} \frac{\partial}{\partial x_i}(u_j) \right\rangle^i + \phi \langle u_j \rangle^i R \\
&\quad - \frac{\partial}{\partial x_j} \left(\langle q_j \rangle^v \right) + h_i a_i \left(\langle T_s \rangle^i - \langle T_f \rangle^i \right)
\end{aligned} \tag{2.25}$$

Expanding the first term on the right-side of deformation work in Eq.(2.25), it is possible to determine the viscous dissipation term Φ (Currie, 2016), as follows:

$$\phi\left\langle \sigma_{ij}\frac{\partial}{\partial x_i}(u_j)\right\rangle^i = \phi\left\langle -P\delta_{ij}\frac{\partial u_j}{\partial x_i} + \mu\left(\frac{\partial u_i}{\partial x_j}+\frac{\partial u_j}{\partial x_i}\right)\frac{\partial u_j}{\partial x_i} - \frac{2}{3}\phi\mu\left(\delta_{ij}\frac{\partial u_k}{\partial x_k}\right)\frac{\partial u_j}{\partial x_i}\right\rangle^i \tag{2.26}$$

$$\phi\left\langle \sigma_{ij}\frac{\partial}{\partial x_i}(u_j)\right\rangle^i = \phi\left\langle -P\frac{\partial u_k}{\partial x_k} + \frac{\mu}{2}\left(\frac{\partial u_i}{\partial x_j}+\frac{\partial u_j}{\partial x_i}\right)^2 - \frac{2}{3}\mu\left(\frac{\partial u_k}{\partial x_k}\right)^2\right\rangle^i \tag{2.27}$$

$$\phi\left\langle \sigma_{ij}\frac{\partial}{\partial x_i}(u_j)\right\rangle^i = \phi\left\langle -P\frac{\partial u_k}{\partial x_k} + \Phi\right\rangle^i \tag{2.28}$$

Thus, replacing the Eq.(2.28) in Eq.(2.25), the following expression holds,

$$\begin{aligned}\rho_f&\left[\frac{D\left(\phi\langle e\rangle^i\right)}{Dt}\right]\\ &= -\phi\left\langle P\frac{\partial u_k}{\partial x_k}\right\rangle^i + \phi\langle\Phi\rangle^i + \phi\langle u_j\rangle^i R - \frac{\partial}{\partial x_j}\left(\langle q_j\rangle^v\right)\\ &\quad + h_i a_i\left(\langle T_s\rangle^i - \langle T_f\rangle^i\right)\end{aligned} \tag{2.29}$$

Finally, considering the continuity equation to replace the term $\frac{\partial u_k}{\partial x_k} = \frac{1}{\rho_f}\frac{D(\rho_f)}{Dt}$ in Eq.(2.29) (Currie, 2016; Cantwell, 2022) the energy expression is described as follows:

$$\begin{aligned}\rho_f&\left[\frac{D\left(\phi\langle e\rangle^i\right)}{Dt}\right]\\ &= \phi\left\langle P\frac{1}{\rho_f}\frac{D(\rho_f)}{Dt}\right\rangle^i + \phi\langle\Phi\rangle^i + \phi\langle u_j\rangle^i R - \frac{\partial}{\partial x_j}\left(\langle q_j\rangle^v\right)\\ &\quad + h_i a_i\left(\langle T_s\rangle^i - \langle T_f\rangle^i\right)\end{aligned} \tag{2.30}$$

Commonly in the literature, the energy equation suffers some simplifications, principally for simplicity against the modeling of complex systems. Usually the second and third terms on the right-side of Eq.(2.30) are neglected (Kribus et al., 2014). Nevertheless, for the correct entropy analysis and modelling, this work considers the complete expression for the energy transport in (2.30). Later in Chapter 4, the expression (2.30) is expanded and modified to develop a detailed entropy transport equation.

To recapitulate, Chapter 2 presents the development in detail of an extended expression for energy transport in a porous medium. From this, it is possible to build an expression for entropy transport. The results presented in this chapter are used in Chapter 4 to establish a macroscopic-scale entropy transport equation. The volumetric terms of stresses exchange and heat transfer determined in this chapter, are the starting point to recognize the additional LEG mechanisms due to the presence of the solid matrix, and the interaction between both phases.

Chapter 3

1D Energy analysis of a porous heat exchanger

As mentioned in Chapter 1, porous media have several applications for heat exchange and storage. Thus, this chapter presents a study case as a preliminary analysis of the transport phenomenon in porous media.

As a result of their large exchange area, porous media are good candidates for the design of heat exchange devices. Nevertheless, due to the drag produced by the presence of the porous matrix, it is necessary to analyse the design, geometry and porosity, to maximize the exchange rate, and also, to minimize losses due to pressure drop. In that context, the discussion in Chapter 3 examines the performance as heat exchange medium for two different porous media applied in a volumetric receiver for CSP.

The behaviour of two different porous media are compared applied in a volumetric receiver for concentrating solar power. The analysis proposes a figure of merit based in energy losses to compare with two configurations for the receiver design. One considers a square microchannel honeycomb structure as porous media, and the second considers a ceramic foam as heat exchange media.

3.1 Motivation

After the initial development in the 80's, the CSP industry has experienced considerable growth since 2007 (Kribus et al., 1996; Ávila-Marín, 2011). In this period, new technologies have reached commercial maturity and new concepts have emerged. Among the CSP technologies, central receiver systems (CRS) have received larger attention during the last years, since the higher operating temperatures allow reaching higher thermal-to-electricity conversion efficiencies. In this context, two main operating schemes have emerged for this technology: Direct Steam Generation and Molten Nitrate Salts receivers, which are denominated as the first and second generation, respectively. Aiming to further improve the conversion efficiencies, several authors proposed the use of compressible gases (CO_2 or air) as working

fluid, due to its thermal stability up to 1200°C. The use of such working fluids requires the implementation of volumetric absorbers. Among the compressible gases, air offers additional advantages by the lower operating pressure and cost, when using atmospheric air in open receiver systems. However, achieving temperatures higher than 1200°C in volumetric absorbers presents two scientific challenges. The first is related to the computational modelling of the transport phenomena inside the porous media, coupling the viscous effects, compressibility, the convective heat transfer, and the extinction-propagation of the concentrated radiation in the solid media. The second challenge is related to the design process regarding the configuration, distribution and material selection of the solid media, with the aim of dealing with the challenging operating conditions. As a consequence, Chapter 3 presents a performance analysis of an open volumetric absorber using atmospheric air as working fluid, comparing honeycomb mini-channel (HC) and ceramic foam (CF) as solid exchange medium.

3.2 Volumetric solar receiver design

A volumetric receiver heats a compressible gas, such as air or supercritical CO_2, taking advantage of the large exchange area of a solid porous medium (packed rock bed, ceramic foam, mini-channel honeycomb, etc.), as shown in Fig 2.3. Likewise, the porous media receives concentrated solar energy from a heliostat field, which permeates upstream trough the porous matrix in the direction of flow. Currently, air is the most studied working fluid due to the simplicity in the implementation, because it is not necessary to deal with high operating pressures of CO_2. Thus, most of the tested systems use open receivers heating atmospheric air (Ávila-Marín, 2011).

Several designs of porous media are proposed in the literature, which could be classified by type of material or the geometric configuration that forms the porous matrix, as follows in Table 3.1:

Structure	Material	Reference
Packed bed	Rock	(Esence et al., 2017; Calderón-Vásquez et al., 2021)
Foam	Metal Ceramic Carbide	(Wu and Yu, 2007; Wu et al., 2011a)
Wire mesh	Metal Ceramic Carbide	(Avila-Marin et al., 2018, 2019)
Packed wool mesh	Mineral Ceramic Carbide	(Fend et al., 2004a)
Mini-Channel	Metal Ceramic Carbide	(Capuano et al., 2016; Pabst et al., 2017)

Table 3.1: Porous media classification

Although the literature offers a wide range of studied porous materials (Table 3.1), the big problem is that there are not enough experimental data to compare satisfactorily the different proposals, and also there are no parameters or figures of merit that allow comparing and measuring the benefit regarded to variations in porous matrix geometry, design, and material implemented in a technological application. Thus, the present work proposes to

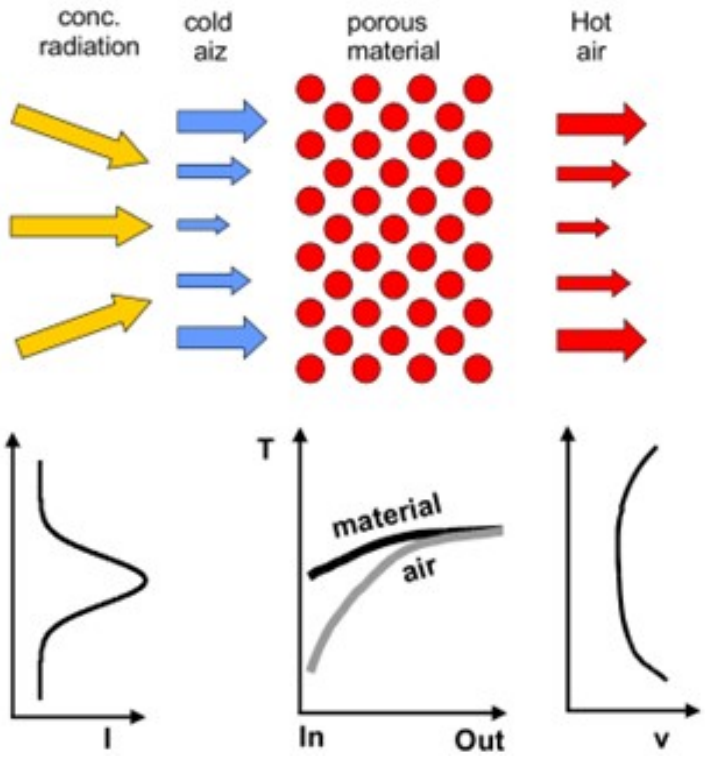

Figure 3.1: Diagram of volumetric absorber. Reprinted from (Fend et al., 2004b), Copyright (2023), with permission from Journal Solar Energy Materials and Solar Cells, Elsevier.

study the local entropy transport in order to analyze the local entropy generation as a performance figure, considering the different mechanisms of entropy generation and their relation with the design, the porous matrix geometry, and flow characteristics. Despite several configurations for volumetric receivers have been proposed in the literature (Ávila-Marín, 2011), the present analysis focusses on comparing two of the most studied configurations, HC and CF. The HC structure presents simplicity for the manufacturing process and offers a low pressure drop. On the other hand, the CF proposal offers outstanding heat exchange capabilities, due to its larger exchange area, but increasing the pressure drop (Wu et al., 2010; Chen et al., 2017; Kribus et al., 2014). Therefore, this relationship, between the benefits of increasing the exchange area and the disadvantages of the pressure drop involved, encourages the analysis presented herein. Thus, in order to establish a comparison framework between both technological options, the methodology proposes a figure of merit able to assess and compare the performance of CF and HC, including the heat exchange benefits and pressure drop involved at the same time. The computational modelling of both technologies was performed through an one-dimensional (1D) model under the same operating conditions for each technology.

3.3 One dimensional analysis of a volumetric solar receiver

To understand the basic concepts about transport phenomena in porous media and the framework commonly used for comparing the performance of some devices in the literature,

a one-dimension analysis was implemented over two volumetric solar receiver systems. The receivers are composed of CF and HC, respectively (see Fig 3.2). Both devices receive concentrated solar radiation which penetrates the solid matrix and extinguishes its value across the porous medium. On the one hand, the ceramic foam receiver offers more exchange area between solid and fluid phases but implies a higher pressure drop in the process. On the other hand, the mini-channel receiver has a lower exchange area with a lower pressure drop. Thus, to have an idea about the performance of both devices were implemented one of the most used figures of merit in the literature to compare heat exchange devices, the goodness factor. This factor was proposed by Bergles et al. (1976) to study the performance of heat exchange devices, comparing the heat transferred to the fluid with the power lost by the pressure drop through the heat exchange device. Thus, considering the relation between the pressure drop and the heat exchange capacity of each aforementioned device, it is proposed a modified volumetric goodness factor as a comparison figure of merit. Thereby, this previous analysis shows how volumetric receivers are studied until now, and what are the additional advantages that an entropy generation analysis can offer for the decision task of defining the best design or geometry for a volumetric solar receiver.

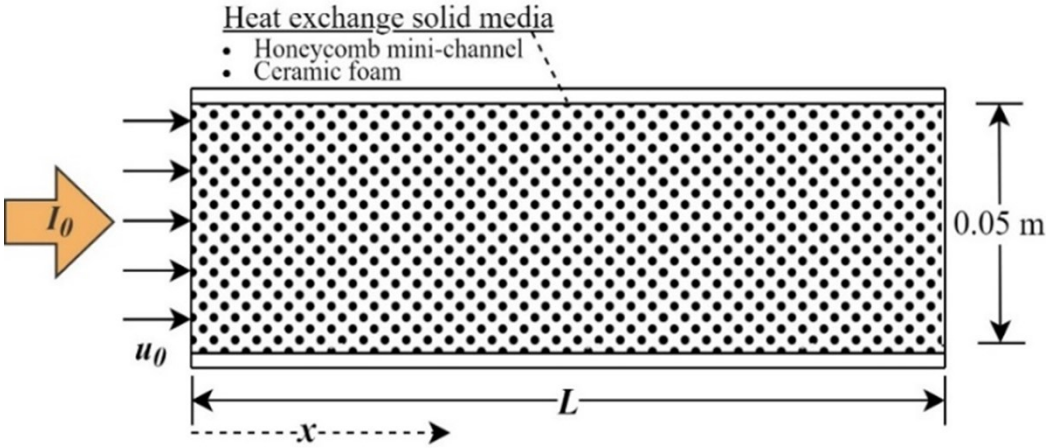

Figure 3.2: Distribution scheme for macroscopic analysis (Sarmiento-Laurel et al., 2019)

3.4 Model Assumptions

The 1D model for both structures was developed in MATLAB using the Runge Kutta numerical integration method (RK4). The system of equations for each kind of absorber considers a) Conservation of mass of the fluid domain, b) Conservation of momentum of the flow, and c) Conservation of energy in the solid and fluid domain. In addition to that, each energy conservation in the solid medium considers a source term for accounting the propagation of the radiation in the solid (considering extinction and emission effects). Likewise, some assumptions were considered to simplify the analysis, considering that the model solves both systems (HC and CF) at the same time. Thus, the assumptions are as follows:

- Conduction effects through the fluid are neglected in both models.

- Radiative absorption at the fluid phase is neglected in both systems.
- Both processes are in steady-state.
- Air is considered an ideal gas.
- Isotropic distribution of porosity.
- Momentum diffusion by viscous effects inside the fluid is neglected in both systems.
- Isolated system on the parallel walls to the flow direction.
- The flow is in Forchheimer regime, $Re_p < 150$ (the Forchheimer term must be considered in the hydrodynamic resistance effort on the momentum equation).

3.5 Theoretical model

Then from the equations stated in Chapter 2, the equation system for both devices is as follows:

3.5.1 Continuity and momentum equations

$$\frac{\partial}{\partial x_k}(\rho_f U) = 0 \tag{3.1}$$

$$\frac{\partial}{\partial x_k}(\rho_f UU) = -\frac{\partial}{\partial x_i}\Big(\langle P\rangle^i \delta_{ij}\Big) - F \tag{3.2}$$

where U is the fluid velocity, which changes to the fluid apparent Darcian velocity $u_D = \phi u$ for the ceramic foam analysis. F is the hydrodynamic resistance in each medium as follows:

Ceramic Foam Hydrodynamic Resistance

$$F_{CF} = R = \phi(\frac{\mu}{k_1}u_D + \frac{\rho_f}{k_2}|u_D|u_D) \tag{3.3}$$

where both k_1 and k_2, are correlation constants determined by Wu's correlation for Ceramic Foam (Wu and Yu, 2007). Thus, the right terms in Eq.(3.3) represent the normal and tangential forces done by the solid matrix over the fluid mean flow, respectively.

Honeycomb Mini-channel Hydrodynamic Resistance

$$F_{HC} = f\frac{\rho}{2l}u^2 \tag{3.4}$$

where l is the mini-channel axial length, f the friction factor concerning to a square channel (Bejan, 1995).

3.5.2 Fluid energy equation

$$\rho_f \frac{\partial}{\partial x_k}(c_{p,f} u_D \langle T_f \rangle^i) = h(\langle T_s \rangle^i - \langle T_f \rangle^i) \tag{3.5}$$

where h is the convection heat transfer coefficient in each medium. For the CF this term represents the volumetric convection heat transfer between the solid and fluid phases, considering the presence of the solid as a macroscopic field effect over the flow (Hsu and Cheng, 1990). This last coefficient was determined by the correlation proposed by Wu et al. (2011b). On the other hand, the HC model considers the standard convection heat transfer in a square channel, which represents the heat exchange per unit of area on the channel wall (Bejan, 2013).

3.5.3 Solid energy equation

$$\frac{\partial}{\partial x_j}(\lambda_s \frac{\partial}{\partial x_j}(\phi \langle T_f \rangle^i)) = h(\langle T_s \rangle^i - \langle T_f \rangle^i) + S_r \tag{3.6}$$

where S_r is the radiative heat source in the solid phase. This source term represents the propagation of the radiation through the receiver, which is determined in different ways according to both mediums. Thus, the source term of the HC considers the equation proposed by Worth et al. (1996), which includes the emission and absorption effects of the radiation entering the square mini-channel. On the other hand, to determine the radiative source in the CF is necessary to solve the radiative transfer equation (RTE) in the solid (Eq. 3.10 Eq. 3.12). Thus, the $P1$ (see section 3.5.4) approximation model was implemented to solve the RTE (Wu et al., 2011a; Andrienko and Surzhikov, 2012; Chen et al., 2017; Modest, 2013).

3.5.4 Radiative energy transport in porous media as a participating media

To consider the transport of radiative energy through the solar receiver, where the radiative energy is usually considered as a heat source only inside the solid matrix, the radiative effects over the fluid phase were neglected. Thus, the RTE (Modest, 2013) performs an energy balance between the radiative energy emitted and scattered by the media and the radiative energy received by emission and scattering in the surrounding of the control volume (see Fig 3.3). Also, the radiation in the porous media is split into collimated and diffuse radiation, where the first is related to the radiation which penetrates the participating media without losing its direction, and the second corresponds to the amount of radiation scattered and emitted by the surroundings.

$$\bar{s} \cdot \nabla I(r, \hat{s}) = k I_b(r) - \beta I(r, \hat{s}) + \frac{\sigma_{s\eta}}{4\pi} \int_{4\pi} I(r, \hat{s}') d\Omega' \tag{3.7}$$

where $I(r, \hat{s})$ is the radiative intensity flux in the direction $\hat{s}$ located on the position r, $\sigma_{s\eta}$ is the scattering coefficient, k is the absorption coefficient and ω is the solid angle. The extinction coefficient $\beta = k + \sigma_s$.

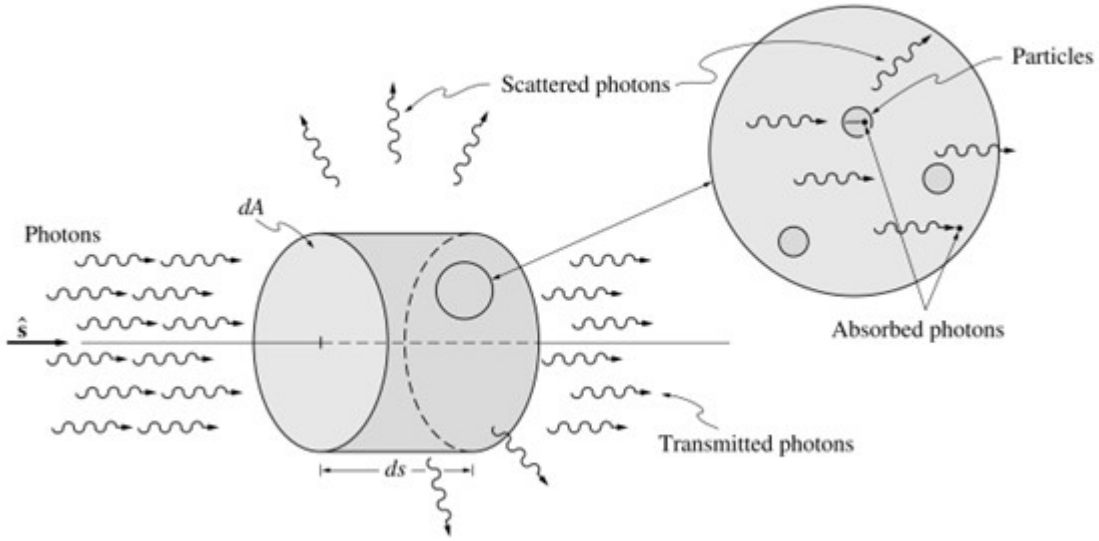

Figure 3.3: Attenuation of radiative intensity by absorption and scattering (Modest, 2013).

P_N and $P1$ approximation methods

To model the transfer of radiative energy in a gray medium (which participates in the absorption, emission and dispersion of radiative energy) it is necessary to have an expression for the radiative intensity flux $I(r, \hat{s})$ in the RTE. Thus, in the literature there are several proposals to shape the $I(r, \hat{s})$ (Eq. 3.7). The P_N method is often recommended to model the $I(r, \hat{s})$ in a medium with radiative characteristics without strong anisotropy. This method consists in defining an expression for $I(r, \hat{s})$ from a number N of Fourier terms (Modest, 2013), as follows:

$$I(r, \hat{s}) = \sum_{l=0}^{\infty} \sum_{m=-l}^{l} I_l^m(r) Y_l^m(\hat{s}) \tag{3.8}$$

where $I_l^m(r)$ are a position-dependent coefficients, r is the position vector in spherical coordinates, and $Y_l^m(\hat{s})$ are spherical harmonic terms.

Due to its complexity, it is common for the P_N method to be used up to the third order. Thus, the $P1$ approximation is a simple case of the P_N method taking the first order of the Fourier series. Then the expression for $I(r, \hat{s})$ is the following:

$$I(r, \hat{s}) = \frac{1}{4\pi}(G(r) + 3q_r(r) \cdot \hat{s}) \tag{3.9}$$

where q_r is the radiative heat transfer rate and G is the total irradiation.

From the Eq. 3.9 it is possible to determine the equation for RTE (Eq. 3.7) (Andrienko and Surzhikov, 2012; Modest, 2013; Kribus et al., 2014), as follows:

$$\frac{\partial}{\partial x_i}\left(\frac{1}{3(k+\sigma_s)}(\frac{\partial}{\partial x_j}G_s)\right) = k(4\sigma\langle T_s\rangle^{i^4} + G_s) + \sigma_s G_c \tag{3.10}$$

where σ is the Stefan–Boltzmann constant, the total irradiation $G = G_c + G_s$ composed by the diffuse integrated intensity G_s and the collimated irradiation in the flow direction $G_c(x)$, as follows:

$$G_c = I_0 e^{-\beta x} \tag{3.11}$$

Considering as following expressions the radiative heat source in solid phase:

$$S_r = \nabla \cdot q_r = -k(G - 4\sigma\langle T_s\rangle^{i^4}) \tag{3.12}$$

The aforementioned optical properties are computed considering the optical approximations for porous media proposed by Vafai (2015).

3.6 Boundary conditions

The equations of mass, momentum, and energy transport for a volumetric receiver (Eq. 3.1 to Eq. 3.5), consider the following boundary conditions:

- The inlet velocity is $u_c = 1\ (ms^{-1})$, which is considered as the apparent u_D velocity for the ceramic foam and, on the other hand, the comparison velocity is divided by the porosity and used as the pore real velocity (pore velocity in porous media analysis).
- The pore diameter in the ceramic is equal to the mini-channel in the honeycomb.
- The axial area of the receiver is a square with high length $l = 0.05\ (m)$.
- The incident radiation is fixed at $I_0 = 600\ (kWm^{-2})$.

Continuity and Momentum transport equation

- $u|_{x=0} = 1\ (ms^{-1})$
- $P|_{x=0} = 101.314\ (kPa)$

(3.13)

Energy transport equation for fluid-phase:

- $T_f|_{x=0} = 298.15\ K$

(3.14)

Energy transport equation for solid-phase:

- $T_s|_{x=0} = T_{s,shoot}$
- $q_s|_{x=0} = -k(\sigma(T^4_{s,shoot} - T^4_{\infty}) + I_0)$
- $q_s|_{x=L} = 0\ (kWm^{-2})$

(3.15)

In addition, to solve the RTE equation on the ceramic foam receiver was considered the Marshak's boundary conditions (Krittacom and Kamiuto, 2009), as follows:

- $G|_{x=0} = I_0$
- $\frac{1}{3(k+\sigma_s)}(\frac{\partial}{\partial x_j}G_s)|_{x=0} = 2\sigma T^4_{\infty} - \frac{G|_{x=0}}{2}$

(3.16)

3.7 Mesh Convergence Analysis

The one-dimensional analysis was implemented through the fourth-order Runge-Kutta method. To define the necessary number of elements, the convergence of the total rate of heat with respect to the number of elements was analyzed. Fig 3.4 shows the variation of the total rate of heat transferred for the Caramic Foam and the Honey Comb, respectively. It can be noted that from the 600 elements the variation of the heat transfer stabilizes in a range of variation below 0.1%. From this, a grid of 2000 elements was defined to ensure convergence of the analysis.

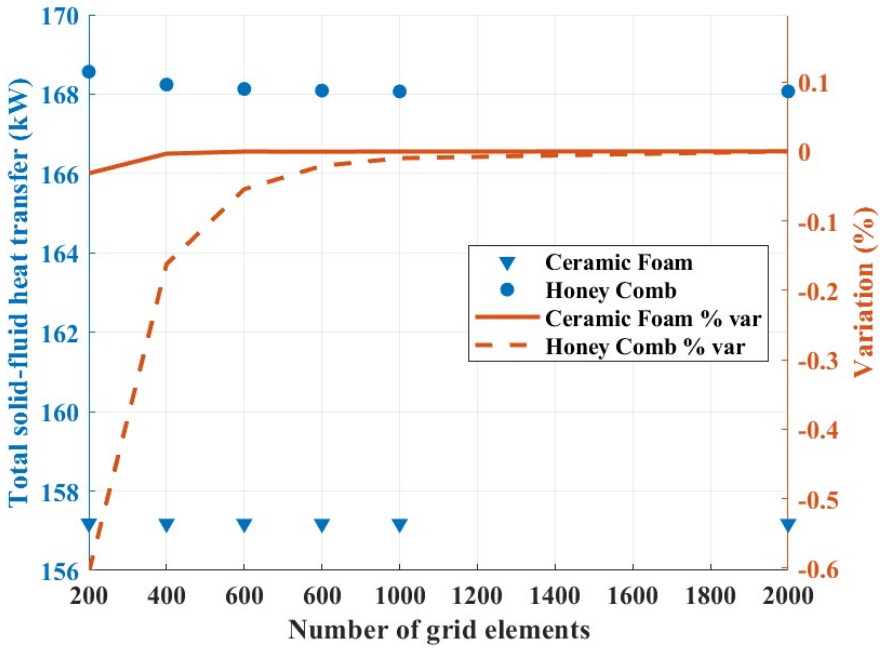

Figure 3.4: Mesh convergence analysis for $\phi = 0.6$ and $U_c = 10$ (ms^{-1}).

3.8 Volumetric Goodness Factor

Aiming to analyze and compare the performance of the HC and CF volumetric receivers, it is proposed a modification of the goodness factor proposed initially by Bergles et al. (Bergles et al., 1976; Shah et al., 2003). In essence, this figure of merit compares the heat transfer capacity of different heat exchange devices, including a penalization which accounts for the pressure drop associated in each case. Nevertheless, Bergles' goodness factor is commonly applied considering average properties (as temperature and fluid velocity) in each side of heat exchange, or in other cases, the logarithmic mean temperature difference between hot and cold sides of the analyzed exchange device. For this analysis, the volumetric goodness factor is integrated through the receiver to compare the real total amount of exchanged energy per unit of time with the total power lost by the hydrodynamic effects. The volumetric goodness factor is defined as follows:

$$GF_{HC} = \int_0^L \frac{h(T_s - T_f)}{\rho_f u(F_{HC})} dx \tag{3.17}$$

$$GF_{CF} = \int_0^L \frac{h_v(\langle T_s \rangle^i - \langle T_f \rangle^i)}{\rho_f \langle u \rangle^i (F_{CF})} dx \tag{3.18}$$

where L is the total length of the receiver in flow direction, GF the volumetric total goodness factor, HC, and CF subscripts represent both technologic proposals honeycomb and ceramic foam, respectively. Finally, both benefit figures of merit are confronted in the comparison factor, which allows determining the best technology considering different design configurations.

$$\psi = \frac{GF_{CF}}{GF_{HC}} \tag{3.19}$$

3.9 1D Analysis Results

Fig 3.5 and Fig 3.7 show the temperature distribution considering different material porosities, for a ceramic foam and honeycomb receiver, respectively. In both, honeycomb and ceramic foam, the inlet velocity is defined as a boundary condition at 1 m/s (for ceramic foam this corresponds to the real velocity). For each medium the porosity has a significative influence in solid inlet temperature, ranging its value between $\sim$ 800 K to $\sim$ 110 K for CF and $\sim$ 700 K to $\sim$ 900 K for HC, considering porosities from 0.5 to 0.9.

Regarding the ceramic foam (Fig 3.5), an increase in the porosity causes a decline in the solid axial area at the inlet face, decreasing the outlet temperature and the total length of the receiver. That length represents the distance necessary to reach a thermal equilibrium between the solid and fluid phases, which ranges from 0.01 to 0.025 m when the porosity takes values from 0.5 to 0.9, respectively. The porosity has a direct impact on the penetration of the radiation through the solid, which is strongly related to the solid temperature and the receiver equilibrium length at the same time. Thus, the solid temperature at the inlet shows a decrease when the porosity varies from 0.5 to 0.7 reaching its minimum value at a porosity of 0.7. Then, for porosities over 0.7 the solid temperature increases. This phenomenon is due to two simultaneous effects, first, a lower porosity implies an increment in the solid axial

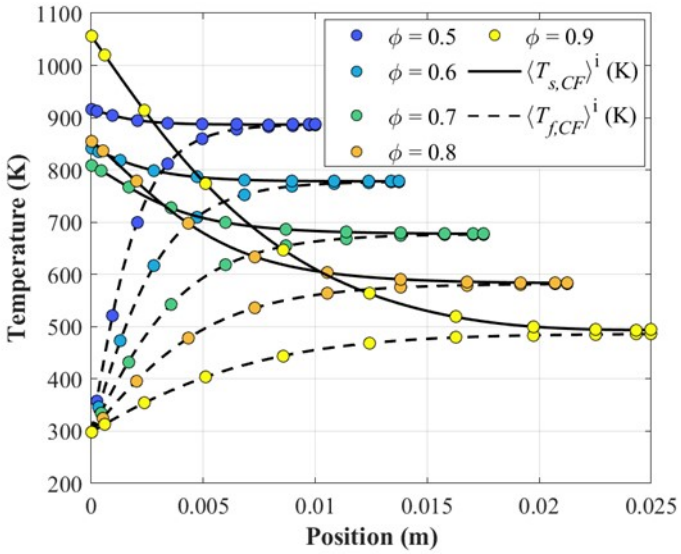

Figure 3.5: Temperature distribution for the solid and fluid phases in the flow direction, for a Ceramic Foam porous media in the receiver, considering a fixed mass flow (Sarmiento-Laurel et al., 2019).

area of the receiver, increasing the amount of radiative energy captured by the solid near the inlet side, then the temperature of the solid rises. Nevertheless, for porosities over 0.7, the previous effect loses significance against the fact that increasing the porosity dismisses the mass of solid, and so the temperature in the solid face increases again. The second effect, lower porosity values imply an increase in the extinction coefficient, which in consequence, reduces the penetration length of the radiation through the solid matrix (see Fig 3.6). Thus, a variation in the porosity has an important influence in the radiative source distribution inside the solid, which reaches higher values near the inlet side with a high rate of decrease in the flow direction for lower porosities, and on the other hand, normalizes its distribution in the flow direction for higher porosities. The honeycomb receiver (Fig 3.7) shows an opposite effect with the change in porosity compared to the aforementioned results with respect to the ceramic foam receiver. This is due to the configuration of the mini-channels of the honeycomb. The mini-channel configuration allows the radiation, normal to the receiver and proportional to φ (fluid portion), to pass across the medium without interacting with the walls of the solid inside the channel, considerably reducing the amount of radiative energy reaching the inner wall of the solid. Moreover, the necessary length to achieve the thermal equilibrium presents ranges from 0.015 to 0.06 m, using more material than the ceramic foam to reach the thermal equilibrium. This difference is due to the way that the different solid media exchange heat with the working fluid. The honeycomb mini-channel offers a lower heat exchange area per unit of length between solid and fluid phases than the ceramic foam. However, this advantage for the ceramic foam implies that the fluid is in constant contact with the inner pore walls (Wu et al., 2010), increasing the irreversibilities related to the drag forces associated with the presence of the solid matrix, commonly illustrated as pressure drop terms of Darcy-Forchheimer's law (Kaviany, 1999).

Figure 3.8 shows the outlet temperature of the fluid in both configurations and the result of the comparison factor, which faces the goodness factor of both technologies. It is possible

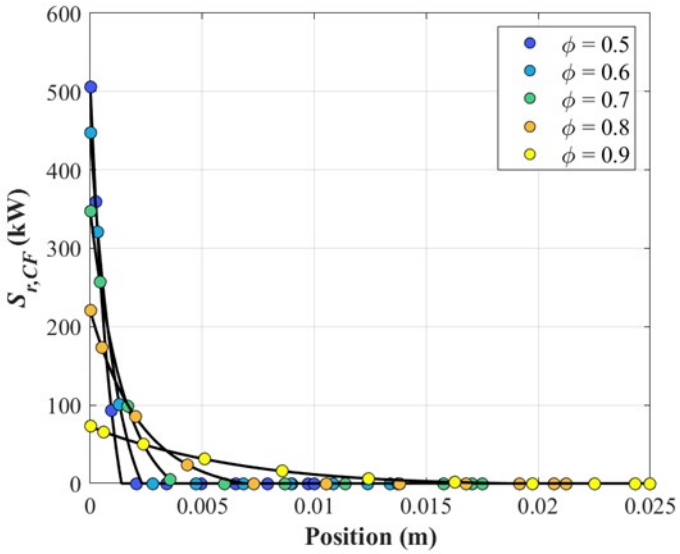

Figure 3.6: Radiative source distribution in the flow direction for the ceramic foam, considering a fixed mass flow. (Sarmiento-Laurel et al., 2019).

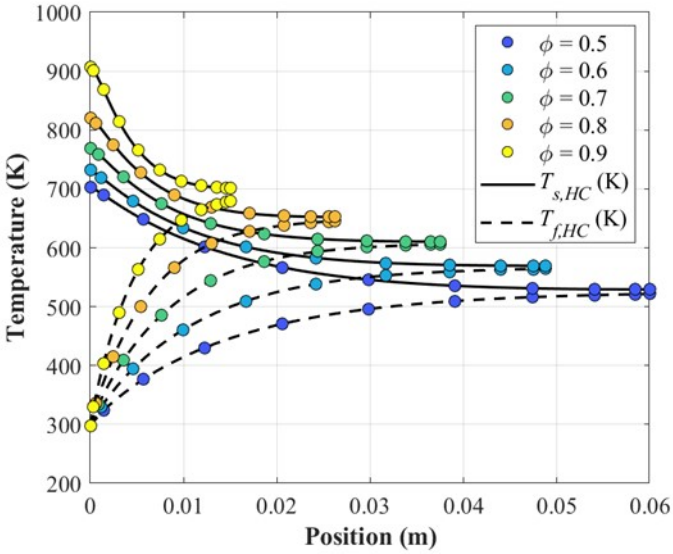

Figure 3.7: Temperature distribution for the solid and fluid phase in the flow direction, for a honeycomb porous media in the receiver. Considering a fix mass flow (Sarmiento-Laurel et al., 2019).

to note how the comparison factor shows a difference of one order of magnitude in all of the porosity ranges, indicating that the ceramic foam has a better performance in all the studied design porosities. This result is unexpected considering that the ceramic foam has a higher hydrodynamic resistance than the honeycomb, due to the inherent tortuosity of the flow path lines within the solid matrix of ceramic foam (Kaviany, 1999). Nevertheless, the definition of the volumetric goodness factor considers the complete effect of the loss of power by pressure drop along with the receiver, which is strongly associated with the receiver's length, and for this analysis, the total length of the HC is more than double the length of the CF. Thus, despite the ceramic foam presenting a higher hydrodynamic resistance, its impact on the

volumetric goodness factor is not significant enough compared to its benefit related to the heat transferred to the fluid.

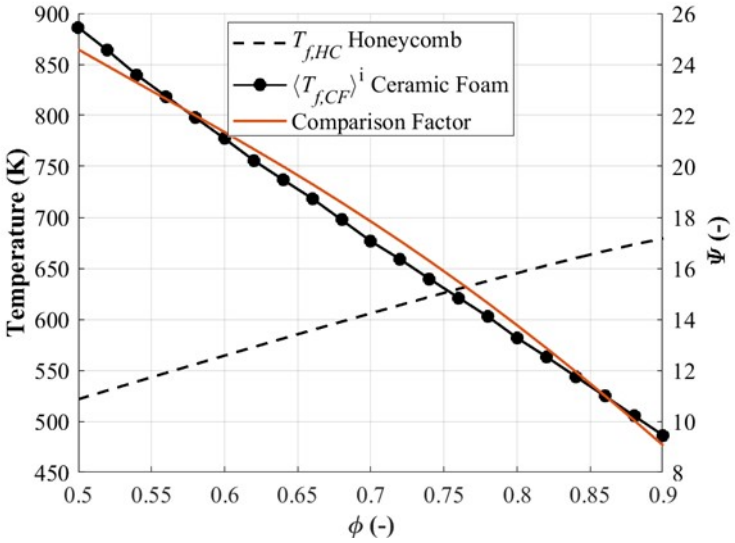

Figure 3.8: Comparison factor and fluid outlet temperature, for different porosities, considering a fixed inlet fluid velocity of ($1ms^{-1}$) (Sarmiento-Laurel et al., 2019).

Figure 3.9 shows the volumetric goodness factor of both technical proposals considering porosities from 0.5 to 0.9. Similarly to the result presented in Figure 3.8, the ceramic foam receiver achieves the highest benefit in terms of the volumetric goodness factor for all porosities. Furthermore, in both technologies, the optimum porosity is 0.9 where the goodness factor is 2.07×105 and 2.29×104 for honeycomb mini-channel and ceramic foam receiver, respectively. In both cases, the principal reason for making a decision about the porosity is the amount of power lost in terms of pressure drop, which is minimum for higher porosities despite the possibility of delivering a higher temperature outlet when considering lower porosities. However, the results in Figure 13 show that the highest outlet temperature of the fluid is reached for porosities of 0.5 and 0.9 for CF and HC, respectively, and for porosities of 0.9 (the best case in both technologies in terms of the goodness factor), the outlet temperature is higher in the HC than in the CF.

3.10 1D Model Main Conclusions

This chapter shows two simplified models, to solve in one dimension the heat exchange process inside two technologies of volumetric receiver, and proposes a comparison factor to measure and compare the benefit of both technological proposals, with the objective of maximizing the heat transferred to the fluid, incurring in the minimum energy lost by the pressure drop. The benefit of this figure of merit considers the energy transferred per unit of time to the working fluid and the power loss due to hydrodynamic resistance of each exchange medium, allowing to compare two different exchange geometries and consider its principal advantages and disadvantages at the same time. The volumetric goodness factor included in

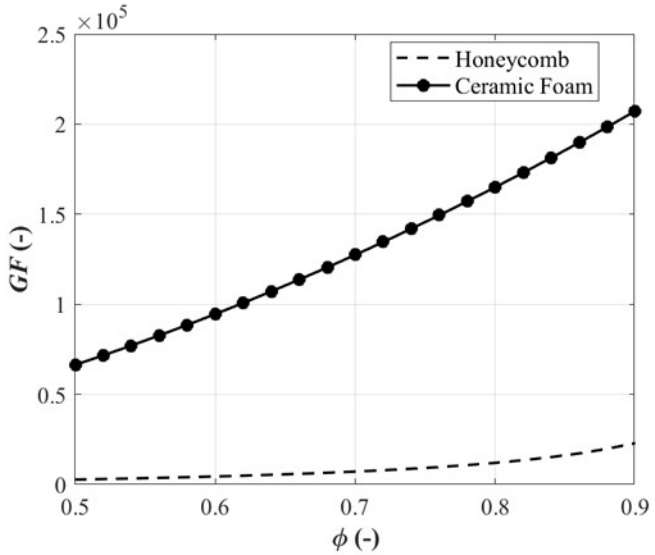

Figure 3.9: Goodness factor for a honeycomb and ceramic foam receivers, considering different porosities (Sarmiento-Laurel et al., 2019).

this analysis explains in a better form the benefit of the devices than others proposed in the literature, because it does not consider an average temperature in the solid and fluid sides or an approximation as the logarithmic mean temperature difference.

The ceramic foam receiver technology offers more exchange area between both phases (fluid and solid), reducing in 58.3% the necessary length to reach the thermal equilibrium compared to the honeycomb mini-channel. Furthermore, the amount of solid material is considerably lower than the honeycomb proposal.

The honeycomb mini-channel reaches higher fluid outlet temperatures from 629.9 to 679.3 K for porosities greater than 0.755. The comparison factor is greater than 9.08 for the complete range of porosity studied in this research. This reinforces the idea about the ceramic foam is the best technology, despite the fact that a solid foam porous medium has a higher hydrodynamic resistance than a mini-channel exchange medium.

However, it is important to note the contradiction of the optimum selection between both approaches, due to the difference in outlet temperatures at a porosity of 0.9. The volumetric goodness factor shows the design which exchanges energy reducing the hydrodynamic losses, however, a higher outlet temperature is also an important factor to take into consideration in the design process. Thus, it is necessary to determine a figure of merit capable of including the quality of the outlet energy. This last idea makes it necessary to include the entropy concept in a future analysis. The entropy generated considers the effects related to the irreversibilities of the heat transfer process and the hydrodynamic resistance, and additionally includes the concept of energy quality, distinguishing the difference between outlet fluids at different temperatures. Thereby, this previous analysis and results allow to defining the main objective of the present proposal, giving a practical sense for studying entropy transport and its generation mechanisms in porous media.

Chapter 4

Local entropy generation model for numerical CFD analysis of fluid flows through porous media, under laminar and turbulent regime

Chapter 4 presents the central part of this thesis. A new expression for entropy generation in porous media is developed and a method is developed to solve it using CFD tools. It is common in the literature that simulation research the implementation of models developed previously by other authors, but there are few works that present the development and implementation of an original model to predict and analyze a phenomenon.

In this chapter, a theoretical expression for local entropy transport and LEG in porous media is developed under low and high Reynolds regimes. First, the spatial dispersion terms associated with macroscopic analysis in a porous medium are studied and developed. Second, the LEG mechanisms by volumetric heat transfer and hydraulic resistance are recognized and mathematically developed. Subsequently, the Reynolds time-averaging method is applied to the entropy transport equation to incorporate the turbulent effects that can appear in high Reynolds regimes. These effects are represented by an expression for turbulent viscous dissipation disaggregated from the mean terms. Analogously, an expression is developed for the LEG by conductive heat transfer associated with temperature time-fluctuations. Finally, an expression is proposed to model the LEG associated with the turbulent component of viscous dissipation and the turbulent component of LEG due to conductive heat transfer. The LEG expression is determined as a post-process from the scalar and vectorial CFD fields resulting of temperature, pressure, k, ε, and velocity.

Later, in Chapter 5, a numerical experiment is conducted to implement the theoretical model stated in Chapter 4. Due to the complexity associated with the instrumentation in porous media, it is reasonable to perform a numerical investigation to evaluate the performance of the proposed model in an initial implementation stage (Ghalandari et al., 2019; Salih et al., 2019).

4.1 Local Entropy Analysis

As a first step to establish a general expression for entropy transport, the entropy is developed as a thermophysical property using the Gibbs' equation from the specific energy and the flow work in the energy conservation equation. Thus, considering the continuity equation (Eq. 2.11) to change the term $\frac{\partial u_k}{\partial x_k} = -\frac{1}{\rho_f}\frac{D(\rho_f)}{Dt}$ in the energy equation (Eq. 2.30, Chapter 2), and using the definition of entropy from the Gibbs' equation (Bejan, 2013; Currie, 2016; Cantwell, 2022) (see Annex (A.3)), it is possible to establish an expression for entropy transport as follows:

$$\begin{aligned}
&\rho_f \left[\frac{D\left(\phi\langle e\rangle^i\right)}{Dt}\right] \\
&= \phi\left\langle P\frac{1}{\rho_f}\frac{D(\rho_f)}{Dt}\right\rangle^i + \phi\langle\Phi\rangle^i + \phi\langle u_j\rangle^i R - \frac{\partial}{\partial x_j}\left(\langle q_j\rangle^v\right) \\
&\quad + h_i a_i\left(\langle T_s\rangle^i - \langle T_f\rangle^i\right)
\end{aligned} \tag{4.1}$$

$$\begin{aligned}
&\rho_f \left[\langle T_f\rangle^i \frac{D\left(\phi\langle s\rangle^i\right)}{Dt}\right] \\
&= -\frac{\partial}{\partial x_j}\left(\langle q_j\rangle^v\right) + \phi\langle\Phi\rangle^i + \phi\langle u_j\rangle^i R \\
&\quad + h_i a_i\left(\langle T_s\rangle^i - \langle T_f\rangle^i\right)
\end{aligned} \tag{4.2}$$

$$\begin{aligned}
&\rho_f \left[\frac{\partial}{\partial t}\left(\phi\langle s\rangle^i\right) + \phi\left\langle\frac{\partial}{\partial x_k}(u_k s)\right\rangle^i\right] \\
&= -\frac{1}{\langle T_f\rangle^i}\frac{\partial}{\partial x_j}\left(\langle q_j\rangle^v\right) + \frac{\phi\langle\Phi\rangle^i}{\langle T_f\rangle^i} \\
&\quad + \frac{\phi\langle u_j\rangle^i}{\langle T_f\rangle^i} R + \frac{h_i a_i}{\langle T_f\rangle^i}\left(\langle T_s\rangle^i - \langle T_f\rangle^i\right)
\end{aligned} \tag{4.3}$$

where s is the entropy per mass unit.

Expanding the heat transfer term on the right side of Eq. 4.3, and using the expression $\frac{\partial}{\partial x_j}\left(\frac{q_j}{T}\right) = \frac{1}{T}\frac{\partial}{\partial x_j}(q_j) - \frac{q_j}{T^2}\frac{\partial}{\partial x_j}(T)$,

$$\begin{aligned}
&\rho_f \left[\frac{\partial}{\partial t}\left(\phi\langle s\rangle^i\right) + \phi\left\langle\frac{\partial}{\partial x_k}(u_k s)\right\rangle^i\right] \\
&= -\left(\frac{\partial}{\partial x_j}\left(\frac{\langle q_j\rangle^v}{\langle T_f\rangle^i}\right) + \frac{\langle q_j\rangle^v}{\left(\langle T_f\rangle^i\right)^2}\frac{\partial}{\partial x_j}\left(\langle T_f\rangle^i\right)\right) \\
&\quad + \frac{\phi\langle\Phi\rangle^i}{\langle T_f\rangle^i} + \frac{\phi\langle u_j\rangle^i}{\langle T_f\rangle^i} R + \frac{h_i a_i}{\langle T_f\rangle^i}\left(\langle T_s\rangle^i - \langle T_f\rangle^i\right)
\end{aligned} \tag{4.4}$$

In addition, it is possible to express the directional heat flux of the second term on the right-side in terms of the Fourier's law of heat conduction (Bejan, 2013) in Eq. 4.4 as, $\langle q_j \rangle^v = -\lambda_{eff,f} \frac{\partial \langle T_f \rangle^i}{\partial x_j}$, and the first term on the right-side as a volumetric heat source, as follows:

$$\begin{aligned}
&\rho_f \left[\frac{\partial}{\partial t} \left(\phi \langle s \rangle^i \right) + \phi \left\langle \frac{\partial}{\partial x_k} (u_k s) \right\rangle^i \right] \\
&= - \left(\frac{\partial}{\partial x_j} \left(\frac{\langle q_j \rangle^v}{\langle T_f \rangle^i} \right) - \frac{\lambda_{\text{eff},f}}{\left(\langle T_f \rangle^i \right)^2} \frac{\partial \langle T_f \rangle^i}{\partial x_j} \frac{\partial \langle T_f \rangle^i}{\partial x_j} \right) \\
&\quad + \frac{\phi \langle \Phi \rangle^i}{\langle T_f \rangle^i} + \frac{\phi \langle u_j \rangle^i}{\langle T_f \rangle^i} R + \frac{h_i a_i}{\langle T_f \rangle^i} \left(\langle T_s \rangle^i - \langle T_f \rangle^i \right)
\end{aligned} \tag{4.5}$$

$$\begin{aligned}
&\rho_f \left[\frac{\partial}{\partial t} \left(\phi \langle s \rangle^i \right) + \phi \left\langle \frac{\partial}{\partial x_k} (u_k s) \right\rangle^i \right] \\
&= - \frac{\partial}{\partial x_j} \left(\frac{\langle q_j \rangle^v}{\langle T_f \rangle^i} \right) + \frac{\lambda_{\text{eff},f}}{\left(\langle T_f \rangle^i \right)^2} \left(\frac{\partial \langle T_f \rangle^i}{\partial x_j} \right)^2 \\
&\quad + \frac{\phi \langle \Phi \rangle^i}{\langle T_f \rangle^i} + \frac{\phi \langle u_j \rangle^i}{\langle T_f \rangle^i} R + \frac{h_i a_i}{\langle T_f \rangle^i} \left(\langle T_s \rangle^i - \langle T_f \rangle^i \right)
\end{aligned} \tag{4.6}$$

Expanding the second term of the left-side in Eq. 4.6, the convective entropy transport due to spatial dispersion of entropy and velocity is determined as follows:

$$\begin{aligned}
&\rho_f \left[\frac{\partial}{\partial t} \left(\phi \langle s \rangle^i \right) + \phi \frac{\partial}{\partial x_k} \left(\langle u_k \rangle^i \langle s \rangle^i \right) \right] \\
&= - \rho_f \phi \frac{\partial}{\partial x_k} \left(\left\langle {}^i u_k {}^i s \right\rangle^i \right) - \frac{\partial}{\partial x_j} \left(\frac{\langle q_j \rangle^v}{\langle T_f \rangle^i} \right) \\
&\quad + \frac{\lambda_{\text{eff},f}}{\left(\langle T_f \rangle^i \right)^2} \left(\frac{\partial \langle T_f \rangle^i}{\partial x_j} \right)^2 \\
&\quad + \frac{\phi \langle \Phi \rangle^i}{\langle T_f \rangle^i} + \frac{\phi \langle u_j \rangle^i}{\langle T_f \rangle^i} R + \frac{h_i a_i}{\langle T_f \rangle^i} \left(\langle T_s \rangle^i - \langle T_f \rangle^i \right)
\end{aligned} \tag{4.7}$$

Therefore, Eq. 4.7 shows the local entropy transport in a porous media through a macroscopic point of view, where each term represents the following phenomena defined in Table 4.1:

Finally, to consider the turbulent effects in the analysis, the time-averaging (Reynolds,

Table 4.1: Local entropy transport terms

Term	Definition
$\rho_f \phi \langle u_k \rangle^i \langle s \rangle^i$	Convective term of microscopic advection of entropy through the spatial mean velocity.
$\rho_f \phi \frac{\partial}{\partial x_k} \left(\langle {}^i u_k {}^i s \rangle^i \right)$	Convective entropy transport due to spatial dispersion of entropy and velocity. This term is also present in laminar convective heat transfer, $Re_D < 150$ (Forchheimer flow regime (Kaviany, 1999; Quintard and Whitaker, 1994), considering $Re_D = \frac{\rho_f u_D d_p}{\mu}$ and d_p the mean pore diameter.
$\frac{\partial}{\partial x_j} \left(\frac{\langle q_j \rangle^v}{\langle T_f \rangle^i} \right)$	Macroscopic entropy generation due to the heat exchange of the fluid control volume with the surroundings.
$\frac{\lambda_{\text{eff},f}}{\left(\langle T_f \rangle^i \right)^2} \left(\frac{\partial \langle T_f \rangle^i}{\partial x_j} \right)^2$	Macroscopic LEG by conduction heat transfer due to the spatial-mean temperature of the fluid.
$\frac{\phi \langle \Phi \rangle^i}{\langle T_f \rangle^i}$	Macroscopic LEG by viscous dissipation due to spatial-mean mean-velocity of the fluid.
$\frac{\phi \langle u_j \rangle^i}{\langle T_f \rangle^i} R$	Entropy generation due to work realized by drag efforts, related to the solid-fluid interaction.
$\frac{h_i a_i}{\langle T_f \rangle^i} \left(\langle T_s \rangle^i - \langle T_f \rangle^i \right)$	Heat transfer entropy generation due to the local heat microscopic heat exchange between fluid and solid phases.

1895) is applied to Eq. 4.6, where $\bar{\varphi}$ is the time average of φ, as follows:

$$\begin{aligned} \rho_f & \left[\frac{\partial}{\partial t} \left(\phi \langle \bar{s} \rangle^i \right) + \phi \left\langle \frac{\partial}{\partial x_k} (\overline{u_k s}) \right\rangle^i \right] \\ & = -\frac{\partial}{\partial x_j} \overline{\left(\frac{\langle q_j \rangle^v}{\langle T_f \rangle^i} \right)} + \overline{\frac{\lambda_{\text{eff},f}}{\left(\langle T_f \rangle^i \right)^2} \left(\frac{\partial \langle T_f \rangle^i}{\partial x_j} \right)^2} \\ & \quad + \overline{\frac{\phi \langle \Phi \rangle^i}{\langle T_f \rangle^i}} + \overline{\frac{\phi \langle u_j \rangle^i}{\langle T_f \rangle^i} R} + \overline{\frac{h_i a_i}{\langle T_f \rangle^i} \left(\langle T_s \rangle^i - \langle T_f \rangle^i \right)} \end{aligned} \tag{4.8}$$

$$\begin{aligned} \rho_f & \left[\frac{\partial}{\partial t} \left(\phi \langle \bar{s} \rangle^i \right) + \phi \left\langle \frac{\partial}{\partial x_k} (\overline{u_k s}) \right\rangle^i \right] \\ & = -\frac{\partial}{\partial x_j} \left(\frac{\langle \overline{q_j} \rangle^v}{\langle \overline{T_f} \rangle^i} \right) + \frac{\lambda_{\text{eff},f}}{\left(\langle \overline{T_f} \rangle^i \right)^2} \overline{\left(\frac{\partial \langle T_f \rangle^i}{\partial x_j} \right)^2} + \frac{\phi \langle \bar{\Phi} \rangle^i}{\langle \overline{T_f} \rangle^i} \\ & \quad + \frac{\phi \langle \overline{u_j} \rangle^i}{\langle \overline{T_f} \rangle^i} \bar{R} + \overline{\left(\frac{\phi \langle u_j \rangle^i}{\langle T_f \rangle^i} \right)' R'} + \frac{h_i a_i}{\langle \overline{T_f} \rangle^i} \left(\langle \overline{T_s} \rangle^i - \langle \overline{T_f} \rangle^i \right) \end{aligned} \tag{4.9}$$

Considering that the solid matrix is rigid and static the fluctuating mechanical energy $\langle u_j \rangle^{i\prime} R'$ is zero, thus, the fifth term on the right-side of Eq. 4.9 is neglected (Pedras and

de Lemos, 2001; de Lemos, 2012; de Lemos and Pedras, 2001).

$$\begin{aligned}
&\rho_f \left[\frac{\partial}{\partial t} \left(\phi \langle \bar{s} \rangle^i \right) + \phi \left\langle \frac{\partial}{\partial x_k} (\overline{u_k s}) \right\rangle^i \right] \\
&= -\frac{\partial}{\partial x_j} \left(\frac{\langle \overline{q_j} \rangle^v}{\langle \overline{T_f} \rangle^i} \right) + \frac{\lambda_{\text{eff},f}}{\left(\langle \overline{T_f} \rangle^i \right)^2} \overline{\left(\frac{\partial \langle T_f \rangle^i}{\partial x_j} \right)^2} \\
&\quad + \frac{\phi \langle \bar{\Phi} \rangle^i}{\langle \overline{T_f} \rangle^i} + \frac{\phi \langle \overline{u_j} \rangle^i}{\langle \overline{T_f} \rangle^i} \bar{R} + \frac{h_i a_i}{\langle \overline{T_f} \rangle^i} \left(\langle \overline{T_s} \rangle^i - \langle \overline{T_f} \rangle^i \right)
\end{aligned} \tag{4.10}$$

Expanding the second and third terms on the right-hand side in Eq. 4.10, both related to entropy generation by conduction heat transfer and viscous dissipation, respectively:

$$\begin{aligned}
&\rho_f \left[\frac{\partial}{\partial t} \left(\phi \langle \bar{s} \rangle^i \right) + \phi \left\langle \frac{\partial}{\partial x_k} (\overline{u_k s}) \right\rangle^i \right] \\
&= -\frac{\partial}{\partial x_j} \left(\frac{\langle \overline{q_j} \rangle^v}{\langle \overline{T_f} \rangle^i} \right) \\
&\quad + \frac{\lambda_{\text{eff},f}}{\left(\langle \overline{T_f} \rangle^i \right)^2} \left[\left\langle \left(\frac{\partial \overline{T_f}}{\partial x_j} \right)^2 \right\rangle^i + \left\langle \overline{\left(\frac{\partial T_f{}'}{\partial x_j} \right)^2} \right\rangle^i \right] \\
&\quad + \frac{2\mu\phi}{\langle \overline{T_f} \rangle^i} \left[\left\langle \left(\frac{\partial \bar{u}_i}{\partial x_j} + \frac{\partial \bar{u}_j}{\partial x_i} \right)^2 + \left(\frac{\partial \bar{u}_k}{\partial x_k} \right)^2 \right\rangle^i \right] \\
&\quad + \frac{2\mu\phi}{\langle \overline{T_f} \rangle^i} \left[\left\langle \overline{\left(\frac{\partial u_i{}'}{\partial x_j} + \frac{\partial u_j{}'}{\partial x_i} \right)^2} + \overline{\left(\frac{\partial u_k{}'}{\partial x_k} \right)^2} \right\rangle^i \right] \\
&\quad + \frac{\phi \langle \overline{u_j} \rangle^i}{\langle \overline{T_f} \rangle^i} \bar{R} + \frac{h_i a_i}{\langle \overline{T_f} \rangle^i} \left(\langle \overline{T_s} \rangle^i - \langle \overline{T_f} \rangle^i \right)
\end{aligned} \tag{4.11}$$

The Eq. 4.10 shows the transport of entropy in a porous medium, considering the effects associated with time-fluctuations at high Reynolds regimes, and the degradation of the energy potential associated with the interaction between both phases (solid and fluid). In particular, the interaction is associated with the volumetric heat exchange and the hydraulic resistance of the drag forces caused by the presence of the solid matrix.

Finally, the following equation shows the LEG rate desaggregating the different generation mechanisms related to the presence of the porous media and the turbulent effects.

$$
\begin{aligned}
\langle \dot{s}_{\text{gen}} \rangle^v = & \frac{\lambda_{\text{eff},f}}{\left(\langle \overline{T_f} \rangle^i \right)^2} \left[\left\langle \left(\frac{\partial \overline{T_f}}{\partial x_j} \right)^2 \right\rangle^i + \left\langle \overline{\left(\frac{\partial T_f{}'}{\partial x_j} \right)^2} \right\rangle^i \right] \\
& + \frac{\mu \phi}{\langle \overline{T_f} \rangle^i} \left[\left\langle \frac{1}{2} \left(\frac{\partial \bar{u}_i}{\partial x_j} + \frac{\partial \bar{u}_j}{\partial x_i} \right)^2 - \frac{2}{3} \left(\frac{\partial \bar{u}_k}{\partial x_k} \right)^2 \right\rangle^i \right] \\
& + \frac{\mu \phi}{\langle \overline{T_f} \rangle^i} \left[\left\langle \frac{1}{2} \overline{\left(\frac{\partial u_i{}'}{\partial x_j} + \frac{\partial u_j{}'}{\partial x_i} \right)^2} - \frac{2}{3} \overline{\left(\frac{\partial u_k{}'}{\partial x_k} \right)^2} \right\rangle^i \right] \\
& + \frac{\phi \langle \overline{u_j} \rangle^i}{\langle \overline{T_f} \rangle^i} \bar{R} + \frac{h_i a_i}{\langle \overline{T_f} \rangle^i} \left(\langle \overline{T_s} \rangle^i - \langle \overline{T_f} \rangle^i \right)
\end{aligned} \tag{4.12}
$$

Adding the complete expressions of the Darcy-Forchheimer analysis and the spatial-averaging method (Kaviany, 1999; de Lemos, 2012) in terms of $\bar{R}$ and h_i, the entropy generation rate is:

$$
\begin{aligned}
\langle \dot{s}_{\text{gen}} \rangle^v = & \frac{\lambda_{\text{eff},f}}{\left(\langle \overline{T_f} \rangle^i \right)^2} \left[\left\langle \left(\frac{\partial \overline{T_f}}{\partial x_j} \right)^2 \right\rangle^i + \overline{\left\langle \left(\frac{\partial T_f{}'}{\partial x_j} \right)^2 \right\rangle^i} \right] \\
& + \frac{\mu \phi}{\langle \overline{T_f} \rangle^i} \left[\left\langle \frac{1}{2} \left(\frac{\partial \bar{u}_i}{\partial x_j} + \frac{\partial \bar{u}_j}{\partial x_i} \right)^2 - \frac{2}{3} \left(\frac{\partial \bar{u}_k}{\partial x_k} \right)^2 \right\rangle^i \right] \\
& + \frac{\mu \phi}{\langle \overline{T_f} \rangle^i} \left[\left\langle \frac{1}{2} \overline{\left(\frac{\partial u_i{}'}{\partial x_j} + \frac{\partial u_j{}'}{\partial x_i} \right)^2} - \frac{2}{3} \overline{\left(\frac{\partial u_k{}'}{\partial x_k} \right)^2} \right\rangle^i \right] \\
& + \frac{\phi \langle \overline{u_j} \rangle^i}{\langle \overline{T_f} \rangle^i} \left[\frac{\mu}{\Delta V} \int_{A_i} \left(\left(\frac{\partial \bar{u}_i}{\partial x_j} + \frac{\partial \bar{u}_j}{\partial x_i} \right) \right. \right. \\
& \left. \left. - \frac{2}{3} \left(\delta_{ij} \frac{\partial \bar{u}_k}{\partial x_k} \right) \right) \cdot \boldsymbol{n} ds_i - \frac{1}{\Delta V} \int_{A_i} \bar{P} \boldsymbol{n} ds_i \right] \\
& + \frac{1}{\langle \overline{T_f} \rangle^i} \left[\frac{1}{\Delta V} \int_{A_i} \boldsymbol{n} \cdot \lambda_f \frac{\partial \overline{T_f}}{\partial x_j} \, ds_i \right]
\end{aligned} \tag{4.13}
$$

Rewriting the last three right-side terms, as is usually done in the literature for the

empirical correlations, Eq. 4.13 is as follows:

$$\begin{aligned}\langle \dot{s}_{\text{gen}} \rangle^v = & \frac{\lambda_{\text{eff},f}}{\left(\langle \overline{T_f} \rangle^i\right)^2} \left[\left\langle \left(\frac{\partial \overline{T_f}}{\partial x_j} \right)^2 \right\rangle^i + \overline{\left\langle \left(\frac{\partial T_f{}'}{\partial x_j} \right)^2 \right\rangle^i} \right] \\ & + \frac{\mu\phi}{\langle \overline{T_f} \rangle^i} \left[\left\langle \frac{1}{2} \left(\frac{\partial \bar{u}_i}{\partial x_j} + \frac{\partial \bar{u}_j}{\partial x_i} \right)^2 - \frac{2}{3} \left(\frac{\partial \bar{u}_k}{\partial x_k} \right)^2 \right\rangle^i \right] \\ & + \frac{\mu\phi}{\langle \overline{T_f} \rangle^i} \left[\left\langle \frac{1}{2} \overline{\left(\frac{\partial u_i{}'}{\partial x_j} + \frac{\partial u_j{}'}{\partial x_i} \right)^2} - \frac{2}{3} \overline{\left(\frac{\partial u_k{}'}{\partial x_k} \right)^2} \right\rangle^i \right] \\ & + \frac{\phi}{\langle \overline{T_f} \rangle^i} \left(\frac{\mu}{k_1} \overline{u_D}^2 + \frac{\rho_f}{k_2} |\overline{u_D}|^2 \overline{u_D} \right) \\ & + \frac{h_i a_i}{\langle \overline{T_f} \rangle^i} \left(\langle \overline{T_s} \rangle^i - \langle \overline{T_f} \rangle^i \right) \end{aligned} \tag{4.14}$$

Bejan presented an intuitive expression for the entropy generation in porous media under Darcian regime ($Re_D < 1$) (Bejan, 1995). In addition to this idea, Eq. 4.14 extends the analysis to higher values of Re_D[1] from the Darcian flow regime to post-Forchheimer and fully turbulent flow regimes, and including the LEG due to the volumetric heat transfer between the flow and the solid matrix.

Bejan's expression:

$$\langle \dot{s}_{\text{gen}} \rangle^i = \frac{\lambda_f}{\left(\langle T_f \rangle^i\right)^2} \left(\frac{\partial \langle T_f \rangle^i}{\partial x_j} \right)^2 + \frac{\mu_f}{k_1 \langle T_f \rangle^i} {u_D}^2 \tag{4.15}$$

In addition to Bejan's LEG equation, in 2008 Betchen and Straatman (2008) presented an extension of LEG in porous media where the LEG was considered as a Forchheimer hydrodynamic resistance term and the volumetric heat transfer was included. Nevertheless, this expression was restricted to Forchheimer flow regime ($Re_D < 150$). Thus, the expression developed in Eq. 4.14 includes the LEG related to the velocity and temperature time fluctuation effects.

Finally, from the expression for the LEG developed in this section, the following two sections are focused on developing a methodology that allows determining the LEG rate in Eq. 4.14 as a post process, without the need to solve an additional transport equation.

[1] considering Re_D as the Reynolds number based in the mean pore diameter d_p: $Re_D = \rho_f u_D d_p / \mu$

Table 4.2: Volume-averaged $k-\varepsilon$ terms

G_k	G_ε	Authors
$\phi\rho_f\varepsilon_\infty$	$\phi C_{2\varepsilon}\rho_f\varepsilon_\infty\frac{\varepsilon_\infty}{k_\infty}$	Nakayama and Kawahara (1999)
$C_k\rho_f\frac{\phi\langle k\rangle^i\bar{u_D}}{\sqrt{K}}$	$\frac{\phi C_{2\varepsilon}C_k\rho_f\langle\varepsilon\rangle^i\bar{u_D}}{\sqrt{K}}$	Pedras and de Lemos (2001)
$\frac{\phi\mu\bar{u_D}}{K}+\frac{\phi\rho_f C_E\lvert\bar{u_D}\rvert\bar{u_D}}{\sqrt{K}}$	$\frac{\phi f(\phi,K)\rho_f\langle\varepsilon\rangle^i\bar{u_D}}{\sqrt{K}}$	Teruel and Rizwan-uddin (2009b,a)

4.2 Local entropy generation in turbulent share flows

Several authors (Nakayama and Kawahara, 1999; Pedras and de Lemos, 2001; Teruel and Rizwan-uddin, 2009b,a) in the literature have presented their closure models to extend the $k-\varepsilon$ turbulence equations scope to porous media by a macroscopic view. In general terms, the proposals have the same structure of the usual $k-\varepsilon$ turbulence model (Khan and Straatman, 2016). It includes an additional term in each equation related to the production and dissipation of macroscopic TKE, due to the presence of the solid matrix G_k and G_ε (see Table 4.2), as follows:

$$\begin{aligned}&\frac{\partial\left(\rho_f\langle k\rangle^i\right)}{\partial t}+\rho_f\frac{\partial}{\partial x_k}\left(\overline{u_{D,k}}\langle k\rangle^i\right)\\&\quad=-\frac{\partial}{\partial x_j}\left[\left(\mu+\frac{\mu_{t\phi}}{\sigma_k}\right)\frac{\partial}{\partial x_j}\left(\phi\langle k\rangle^i\right)\right]\\&\qquad+P_k-\rho_f\phi\langle\varepsilon\rangle^i+G_k\end{aligned}\tag{4.16}$$

$$\begin{aligned}&\frac{\partial\left(\rho_f\langle\varepsilon\rangle^i\right)}{\partial t}+\rho_f\frac{\partial}{\partial x_k}\left(\overline{u_{D,k}}\langle\varepsilon\rangle^i\right)\\&\quad=-\frac{\partial}{\partial x_j}\left[\left(\mu+\frac{\mu_{t\phi}}{\sigma_k}\right)\frac{\partial}{\partial x_j}\left(\phi\langle\varepsilon\rangle^i\right)\right]\\&\qquad+C_1P_i\frac{\langle\varepsilon\rangle^i}{\langle k\rangle^i}-C_2\frac{\langle\varepsilon\rangle^i}{\langle k\rangle^i}\left(\rho_f\phi\langle\varepsilon\rangle^i\right)+G_\varepsilon\end{aligned}\tag{4.17}$$

where $\langle k\rangle^i$ is the volume average TKE, $\langle\varepsilon\rangle^i$ is the volume average of the dissipation rate of TKE, P_i is the production rate of $\langle k\rangle^i$, G_i is the generation rate of $\langle k\rangle^i$, $\mu_{t\phi}$ is the turbulent viscosity for porous media, and C_1, C_2, σ_k are $k-\varepsilon$ model constants. C_E is the inertial coefficient of porous media, and $f(\phi,K)$ introduced by Teruel and Rizwan-uddin (2009b) to include the effects of the morphology of the solid matrix. This function is zero for $\phi=1$ and tends to infinity for $\phi=0$. Moreover, Nakayama and Kawahara (1999) defined ε_∞ and k_∞ as model constants that must be determined experimentally using a pore-scale numerical analysis.

Therefore, to solve the usual transport equations of mass, momentum, and energy (in Annex (A.4)), this analysis aims to determine the LEG without solving an additional entropy transport equation. Thus, the present analysis proposes an expression to determine the LEG

as a post-process from the velocity, temperature, k, and ε solution fields, after solving the volume-averaged conservation equations and the turbulence $k-\varepsilon$ equations for porous media in the literature. When studying Eq. 4.14 it is possible to separate $\langle \dot{s}_{gen} \rangle^v$ into two main groups of entropy generation mechanisms, heat transfer $\langle \dot{s}_\Theta \rangle^v$ and viscous dissipation $\langle \dot{s}_\Phi \rangle^v$, as follows:

$$\langle \dot{s}_\Theta \rangle^v = \underbrace{\frac{\lambda_{\text{eff},f}}{\left(\langle \overline{T_f} \rangle^i\right)^2} \left\langle \left(\frac{\partial \overline{T_f}}{\partial x_j}\right)^2 \right\rangle^i}_{\langle \dot{s}_{\Theta,\bar{C}} \rangle^v} + \underbrace{\frac{\lambda_{\text{eff},f}}{\left(\langle \overline{T_f} \rangle^i\right)^2} \overline{\left\langle \left(\frac{\partial T_f{}'}{\partial x_j}\right)^2 \right\rangle^i}}_{\langle \dot{s}_{\Theta,C'} \rangle^v} + \underbrace{\frac{h_i a_i}{\langle \overline{T_f} \rangle^i} \left(\langle \overline{T_s} \rangle^i - \langle \overline{T_f} \rangle^i \right)}_{\dot{s}_{\Theta,V}} \tag{4.18}$$

where $\left\langle \dot{s}_{\Theta,\bar{C}} \right\rangle^v$ is the LEG rate by the conductive heat transfer related to the time-average fluid temperature, $\langle \dot{s}_{\Theta,C'} \rangle^v$ is the LEG rate due to the conductive heat transfer associated with the fluid temperature fluctuations. The last term $\dot{s}_{\Theta,v}$ is the entropy generation rate, due the volumetric heat transfer between the solid and fluid phases. Analogously,

$$\langle \dot{s}_\Phi \rangle^v = \underbrace{\frac{\mu\phi}{\langle \overline{T_f} \rangle^i} \left[\left\langle \frac{1}{2} \left(\frac{\partial \bar{u}_i}{\partial x_j} + \frac{\partial \bar{u}_j}{\partial x_i} \right)^2 - \frac{2}{3} \left(\frac{\partial \bar{u}_k}{\partial x_k} \right)^2 \right\rangle^i \right]}_{\left\langle \dot{s}_{\Phi,\bar{D}} \right\rangle^v} + \underbrace{\frac{\mu\phi}{\langle \overline{T_f} \rangle^i} \left[\left\langle \overline{\frac{1}{2} \left(\frac{\partial u_i{}'}{\partial x_j} + \frac{\partial u_j{}'}{\partial x_i} \right)^2} - \frac{2}{3} \overline{\left(\frac{\partial u_k{}'}{\partial x_k} \right)^2} \right\rangle^i \right]}_{\langle \dot{s}_{\Phi,D'} \rangle^v} + \underbrace{\frac{\phi}{\langle \overline{T_f} \rangle^i} \left(\frac{\mu}{k_1} \overline{u_D}^2 + \frac{\rho_f}{k_2} |\overline{u_D}|^2 \overline{u_D} \right)}_{\dot{s}_{\Phi,DF}} \tag{4.19}$$

where $\left\langle \dot{s}_{\Phi,\bar{D}} \right\rangle^v$ is the LEG rate due to viscous dissipation related to the time-average velocity, $\langle \dot{s}_{\Phi,D'} \rangle^v$ is the LEG rate by viscous dissipation regarded to the fluid velocity time fluctuations, and $\dot{s}_{\Phi,DF}$ is the LEG rate associated with Darcy-Forchheimer's hydrodynamic resistance due to the presence of the solid matrix against the flow.

4.3 Entropy generation by turbulent dissipation and thermal dispersion for CFD

For the analysis of $\langle \dot{s}_\Phi \rangle^v$ and $\langle \dot{s}_\Theta \rangle^v$, the terms $\left\langle \dot{s}_{\Theta,\bar{C}} \right\rangle^v$, $\dot{s}_{\Theta,v}$ and $\left\langle \dot{s}_{\Phi,\bar{D}} \right\rangle^v$ can be calculated by solving the transport and volume averaged $k-\varepsilon$ equations. On the other hand, the

fluctuation terms $\langle \dot{s}_{\Phi,D'} \rangle^v$ and $\langle \dot{s}_{\Theta,C'} \rangle^v$, are determined from the $k-\varepsilon$ scalar results. Thus, from the ε definition:

$$\begin{aligned}\langle \dot{s}_{\Phi,D'} \rangle^v &= \frac{\mu\phi}{\langle \overline{T_f} \rangle^i} \left[\left\langle \overline{\frac{1}{2}\left(\frac{\partial u_i{}'}{\partial x_j} + \frac{\partial u_j{}'}{\partial x_i} \right)^2} - \frac{2}{3}\overline{\left(\frac{\partial u_k{}'}{\partial x_k} \right)^2} \right\rangle^i \right] \\ &= \frac{\phi\mu \langle \varepsilon \rangle^i}{\langle \overline{T_f} \rangle^i} \end{aligned} \tag{4.20}$$

where $\langle \varepsilon \rangle^i$ is the viscous dissipation scalar term of the volume averaged turbulence model $k-\varepsilon$.

To solve the term $\langle \dot{s}_{\Phi,D'} \rangle^v$ it is necessary to consider the dissipation of the temperature fluctuation $\varepsilon_\Theta = \alpha_f \overline{\left(\frac{\partial T_f{}'}{\partial x_j} \right)^2}$ defined by Nagano and Kim (1988) in their two equations turbulence model, which establishes two pairs of equations, $k-\varepsilon$ and $k_\Theta - \varepsilon_\Theta$, where the second defines the temperature field fluctuations. Thus, $\langle \dot{s}_{\Theta,C'} \rangle^v$ can be rewritten as:

$$\langle \dot{s}_{\Theta,C'} \rangle^v = \frac{\lambda_{\text{eff},f}}{\left(\langle \overline{T_f} \rangle^i \right)^2} \overline{\left\langle \left(\frac{\partial T_f{}'}{\partial x_j} \right)^2 \right\rangle^i} = \frac{\rho_f c_{p,f} \phi}{\left(\langle \overline{T_f} \rangle^i \right)^2} \langle \varepsilon_\Theta \rangle^i \tag{4.21}$$

To determine the term ε_Θ without solving an additional $k_\Theta - \varepsilon_\Theta$ pair of equations, Kock and Herwig (2004) have proposed a useful approximation, which consists in approximating ε_Θ as the production rate of k_Θ defined as $P_{k,\Theta}$ (Kock and Herwig, 2005; Gersten and Herwig, 2013). From this approximation, it is possible to determine ε_Θ without solving an additional $k_\Theta - \varepsilon_\Theta$ equation system. This approximation is usually considered valid in the logarithmic region. Thus, ε_Θ can be rewritten as follow:

$$\rho_f \varepsilon_\Theta = P_{k,\Theta} = -\rho_f \overline{u_j{}' T'} \frac{\partial \bar{T}_f}{\partial x_j} \tag{4.22}$$

Extending Eq.4.22 to $\langle \varepsilon_\Theta \rangle^i$,

$$\rho_f \phi \langle \varepsilon_\Theta \rangle^i = -\rho_f \phi \overline{\langle u_j{}' T' \rangle^i} \frac{\partial \langle \bar{T}_f \rangle^i}{\partial x_j} \tag{4.23}$$

In addition, to solve for the terms $\overline{\langle u_j{}' T' \rangle^i}$, a Boussinesque-like approach is applied (Kock and Herwig, 2004), adapted to the volume-average method proposed by de Lemos (2012); Nakayama and Kawahara (1999), through the eddy-diffusivity concept.

$$-\overline{\langle u_j{}' T' \rangle^i} = \alpha_{t\phi} \frac{\partial \langle \bar{T}_f \rangle^i}{\partial x_j} \tag{4.24}$$

where $\alpha_{t\phi} = \mu_{t\phi}/\rho_f Pr_{t\phi}$ is the turbulent thermal diffusivity for porous media, $Pr_{t\phi} = \mu_{t\phi}/\alpha_{t\phi}$ is the turbulent volume average Prandtl number, and $\mu_{t\phi}$ is the turbulent viscosity for porous media $\mu_{t\phi} = \rho_f C_\mu (\langle k \rangle^i)^2 / \langle \varepsilon \rangle^i$, stated by de Lemos (2012); Lee and Howell (1987).

Finally, replacing Eq.4.23 and Eq.4.24 in Eq.4.21:

$$\langle \varepsilon_\Theta \rangle^i = -\left(\alpha_{t\phi} \frac{\partial \langle \bar{T}_f \rangle^i}{\partial x_j} \right) \frac{\partial \langle \bar{T}_f \rangle^i}{\partial x_j} \tag{4.25}$$

$$\begin{aligned} \langle \dot{s}_{\Theta,C'} \rangle^v = & \frac{\rho_f c_{p,f}}{\left(\langle \overline{T_f} \rangle^i \right)^2} \frac{C_\mu (\langle k \rangle^i)^2 \phi}{Pr_{t\phi} \langle \varepsilon \rangle^i} \\ & \times \left[\left(\frac{\partial \langle \bar{T}_f \rangle^i}{\partial x} \right)^2 + \left(\frac{\partial \langle \bar{T}_f \rangle^i}{\partial y} \right)^2 + \left(\frac{\partial \langle \bar{T}_f \rangle^i}{\partial z} \right)^2 \right] \end{aligned} \tag{4.26}$$

Hence, from the mathematical methodology described above it is possible to determine the LEG without solving an additional entropy transport equation or $k_\Theta - \varepsilon_\Theta$ equation system, additional to the usual conservation equations and $k - \varepsilon$ turbulence model for porous media.

Recapitulating, the proposed expression determines the LEG for a flow through a porous medium, considering the effects associated with the turbulence and the transfer of heat and momentum between the solid and liquid phases. The definitive expression for the LEG for CFD and the assumptions considered are shown below. Local entropy generation model assumptions:

- Non-thermal equilibrium between the solid and fluid phases.
- There is no mass exchange between the solid phase and the liquid phase.
- The solid matrix is rigid and static in space.
- A Newtonian fluid is considered.
- The turbulence is modeled using $k - \varepsilon$ equation system.
- The mechanical energy of the fluctuating hydrodynamic drag force $\overline{\langle u_j \rangle^{i'} R'}$ is neglected (de Lemos, 2012).
- The temperature fluctuation ε_Θ and the production rate of k_Θ have the same order of magnitude; ergo: $\varepsilon_\Theta = P_{k,\Theta}$.

$$
\begin{aligned}
&\left\langle \dot{s}_{\mathrm{gen},f} \right\rangle^{v} \\
&\quad = \left(\frac{\lambda_{\mathrm{eff},f} + \lambda_{t\phi,f}}{\left(\left\langle \overline{T_f} \right\rangle^{i} \right)^{2}} \right) \left(\frac{\partial \left\langle \bar{T}_f \right\rangle^{i}}{\partial x_j} \right)^{2} \\
&\qquad + \frac{h_i a_i}{\left\langle \overline{T_f} \right\rangle^{i}} \left(\left\langle \overline{T_s} \right\rangle^{i} - \left\langle \overline{T_f} \right\rangle^{i} \right) \\
&\qquad + \frac{\mu\phi}{\left\langle \overline{T_f} \right\rangle^{i}} \left[\left\langle \frac{1}{2} \left(\frac{\partial \bar{u}_i}{\partial x_j} + \frac{\partial \bar{u}_j}{\partial x_i} \right)^{2} - \frac{2}{3} \left(\frac{\partial \bar{u}_k}{\partial x_k} \right)^{2} \right\rangle^{i} \right] \\
&\qquad + \frac{\phi\mu \left\langle \varepsilon \right\rangle^{i}}{\left\langle \overline{T_f} \right\rangle^{i}} + \frac{\phi}{\left\langle \overline{T_f} \right\rangle^{i}} \left(\frac{\mu}{k_1} \overline{u_D}^{2} + \frac{\rho_f}{k_2} |\overline{u_D}|^{2} \overline{u_D} \right)
\end{aligned}
\tag{4.27}
$$

From the model presented in this chapter it is concluded that it is possible to develop an expression for the generation and transport of entropy at a local scale in a porous medium. Through the proposed methodology it is possible to determine the contribution of the different entropy generation mechanisms, distinguishing the additional generation mechanisms that arise from the volumetric exchange of heat and stress between the fluid and the solid porous matrix.

Chapter 5

Numerical experiment: Study Case

From the LEG equation and the modeling methodology developed in Chapter 4, Chapter 5 presents a case of study where the LEG is analyzed under different boundary temperatures and Reynolds regimes. Similarly, to put the proposed methodology into practice, a computational simulation tool has been developed in OpenFOAM V9 (2021) for this case. The tool consists of a CFD solver composed of two main libraries, the first is developed to simulate heat transfer in porous media considering NTE between solid and fluid, and the second library links the temperature, velocity, and pressure fields to determine the different LEG mechanisms stated in Chapter 4.

5.1 OpenFOAM®

OpenFOAM (Open-source Field Operation and Manipulation) is an open-source toolbox developed in *C++* and distributed by the OpenFOAM Foundation (OpenFOAM V9, 2021). The toolbox works as a framework for the integration and development of approximately 100 libraries written in object-oriented languages (see Figure 5.1).

The latest version of OpenFOAM offers around 200 applications for the analysis of problems of transport phenomena in fluids and/or solids. Applications are divided into 2 categories, solvers, and utilities. The *solvers* are focused on the simulation of specific problems such as: compressible flows, fluid mechanics in non-Newtonian fluids, heat transfer, and turbulence, among others. On the other hand, the *utilities* cover a wide range of uses focused on data management for pre- and post-processing of results, as well as the integration of applications in problems that require more than one *solver* (see Figure 5.2).

The software has the advantage of being built through sub-elements as independent classes, allowing the user to build and attach new modules without damaging or inducing errors in the core code of the software. This allows the experienced user to develop new tools and take advantage of the long list of *utilities* that OpenFOAM has.

In numerical modeling, OpenFOAM allows to control the numerical scheme separately for each term in a differential equation, increasing the user's control over their model.

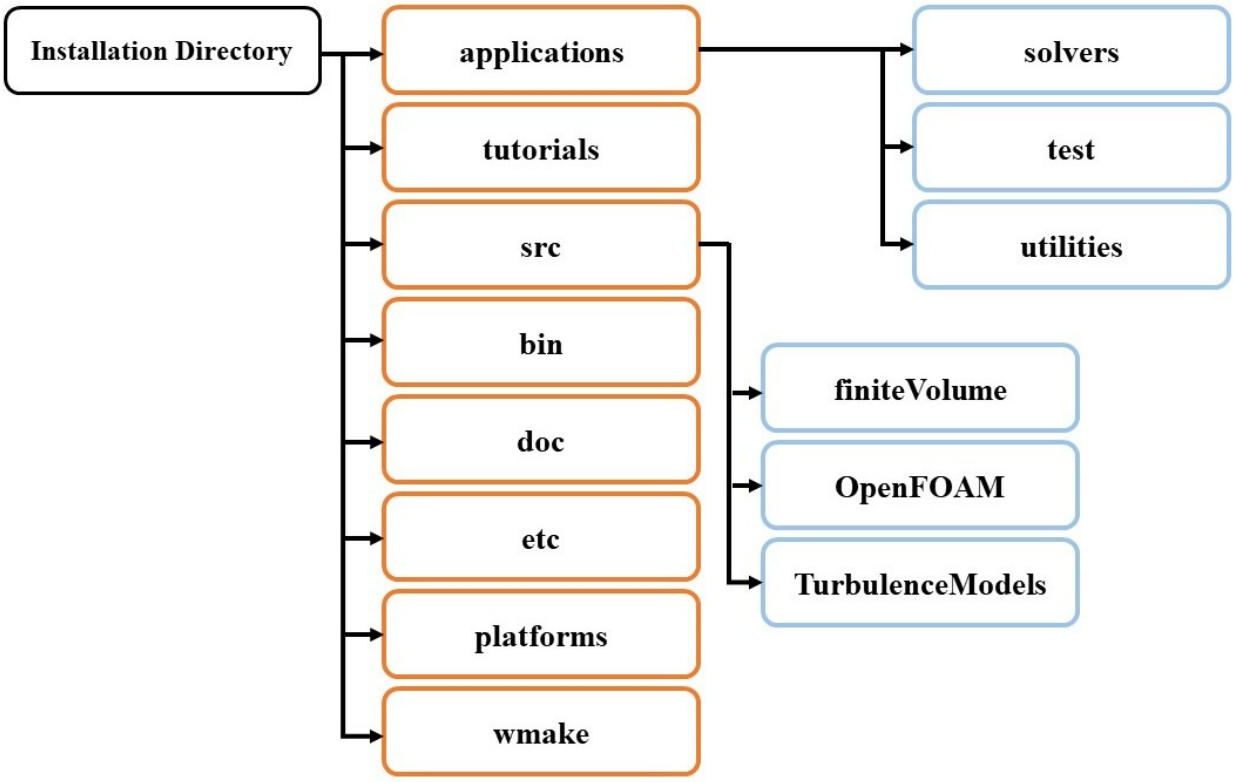

Figure 5.1: OpenFOAM directory.

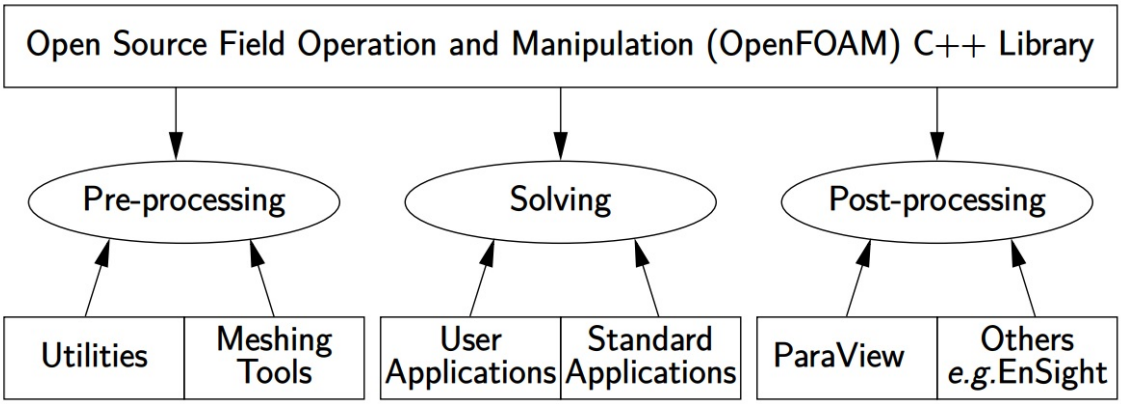

Figure 5.2: Overview of OpenFOAM structure (Greenshields, 2022).

In its standard version, OpenFOAM does not have a graphical interface, working directly in the Linux terminal. This makes it usually difficult for a new user to use this tool. However, in the long run, working from the terminal allows for more accurate and faster control of the parametric analysis of multiple simulations.

5.1.1 Development of *SgenPorousSimpleFoam* solver in OpenFOAM

The proposed solver *SgenPorousSimpleFoam*, was developed from the structure of the *simpleFoam* solver. *SimpleFoam* employs the SIMPLE algorithm (Semi-Implicit Method for pressure Linked Equations) of Patankar and Spalding (1972); Patankar (2018) to solve the pressure and velocity fields of the continuity and momentum equations, considering steady state for isothermal flows. Equations 5.1 and 5.2, are considered for the *simpleFoam* library, as follows:

$$\rho_f \frac{\partial(\bar{u}_k)}{\partial x_k} = 0 \tag{5.1}$$

$$\rho_f \frac{\partial(\bar{u}_j \bar{u}_k)}{\partial x_k} = \frac{\partial}{\partial x_i}\left(-\bar{P}\delta_{ij} + (\mu + \mu_T)\left(\left(\frac{\partial \bar{u}_i}{\partial x_j} + \frac{\partial \bar{u}_j}{\partial x_i}\right) - \frac{2}{3}\delta_{ij}\frac{\partial u_k}{\partial x_k}\right)\right) \tag{5.2}$$

where μ is the viscosity of the fluid and μ_T is the turbulent fluid viscosity.

The development of new solvers in OpenFOAM allows to define in detail the equation system and the variables to be implemented. Therefore, in the present work, a solver was developed to model the transport phenomena through a porous medium, considering the energy equations for the solid and fluid phases separately (non-thermal equilibrium configuration (Eq. 2.29)), and the hydrodynamic resistance due to the presence of the solid matrix.

To determine the hydrodynamic resistance effects related to the presence of the solid porous matrix, the terms of Darcy and Forchheimer are added to Eq. 5.2 as follows:

$$\begin{aligned}\rho_f \frac{\partial}{\partial x_k}\left(\phi\langle \bar{u}_j \bar{u}_k\rangle^i\right) = \frac{\partial}{\partial x_i}\Bigg(&-\phi\langle \bar{P}\rangle^i \delta_{ij} + \phi(\mu+\mu_T)\left(\frac{\partial\langle \bar{u}_i\rangle^i}{\partial x_j} + \frac{\partial\langle \bar{u}_j\rangle^i}{\partial x_i}\right) \\ &- \frac{2}{3}\phi(\mu+\mu_T)\left(\delta_{ij}\frac{\partial\langle \bar{u}_k\rangle^i}{\partial x_k}\right)\Bigg) - \phi\left(\frac{\mu}{k_1}\overline{u_D} + \frac{\rho_f}{k_2}|\overline{u_D}|\overline{u_D}\right)\end{aligned} \tag{5.3}$$

where $\bar{u}$ the time-averaged velocity, $u^{'}$ the velocity time-fluctuation term, ϕ the porosity, and $\bar{P}$ the time-averaged fluid pressure. The fluid viscosity is determined through the Sutherland law (Sutherland, 1893).

The last two terms on the right side of Eq. 5.3 derive from the expressions (2.5) and (2.6) applied to both surface force terms, pressure and viscous shear stress. They represent the interaction between the fluid and the solid matrix as drag force components.

On the other hand, the energy equations for the fluid and solid phases are included as follows.

$$\rho_f c_{p,f}\left(\frac{\partial}{\partial x_k}\left(\phi\langle \overline{T_f}\,\overline{u}_k\rangle^i\right)\right) = \frac{\partial}{\partial x_k}\left(\lambda_{eff,f}\frac{\partial\langle \overline{T_f}\rangle^i}{\partial x_k}\right) + h_i a_i\left(\langle \overline{T_s}\rangle^i - \langle \overline{T_f}\rangle^i\right) \tag{5.4}$$

$$0 = \frac{\partial}{\partial x_k}\left((1-\phi)\lambda_s \frac{\partial \left\langle \overline{T_f} \right\rangle^i}{\partial x_k}\right) - h_i a_i \left(\left\langle \overline{T_s} \right\rangle^i - \left\langle \overline{T_f} \right\rangle^i\right) \tag{5.5}$$

where c_p is the specific heat, λ the thermal conductivity, $\bar{T}$ is the time-averaged temperature, and the subscripts f and s are related to fluid and solid phases, respectively. Fluid density is determined using the ideal gases state equation, $\rho_f = \frac{\left\langle \overline{P} \right\rangle^i}{R_{gas}\left\langle \overline{T_f} \right\rangle^i}$

The last term on the right side of Eq. 5.4 and Eq. 5.5 represents the volumetric heat exchange between the solid and liquid mediums, where $h_i a_i$ varies as a function of the porosity and tortuosity of the solid medium, usually determined by a numerical CFD experiment at the pore scale (Chen et al., 2017).

Thus, *SgenPorousSimpleFoam* determines the LEG as a post-process function result after solving the momentum and energy equations. *SgenPorousSimpleFoam* couples the available turbulence libraries for RAS (Reynolds average simulation) models to use the scalars results of k and ε in the LEG expression stated in Chapter 4, as follows:

$$\begin{aligned}
&\left\langle \dot{s}_{\mathrm{gen},f} \right\rangle^v \\
&= \left(\frac{\lambda_{\mathrm{eff},f} + \lambda_{t\phi,f}}{\left(\left\langle \overline{T_f} \right\rangle^i\right)^2}\right)\left(\frac{\partial \left\langle \bar{T}_f \right\rangle^i}{\partial x_j}\right)^2 \\
&\quad + \frac{h_i a_i}{\left\langle \overline{T_f} \right\rangle^i}\left(\left\langle \overline{T_s} \right\rangle^i - \left\langle \overline{T_f} \right\rangle^i\right) \\
&\quad + \frac{\mu\phi}{\left\langle \overline{T_f} \right\rangle^i}\left[\left\langle \frac{1}{2}\left(\frac{\partial \bar{u}_i}{\partial x_j} + \frac{\partial \bar{u}_j}{\partial x_i}\right)^2 - \frac{2}{3}\left(\frac{\partial \bar{u}_k}{\partial x_k}\right)^2 \right\rangle^i\right] \\
&\quad + \frac{\phi\mu\langle\varepsilon\rangle^i}{\left\langle \overline{T_f} \right\rangle^i} + \frac{\phi}{\left\langle \overline{T_f} \right\rangle^i}\left(\frac{\mu}{k_1}\overline{u_D}^2 + \frac{\rho_f}{k_2}|\overline{u_D}|^2\overline{u_D}\right)
\end{aligned} \tag{5.6}$$

The diagram in Figure 5.3 shows the additional equations and properties that were added into the structure of *SgenPorousSimpleFoam*.

Assumptions of the solver:

- Isotropic porosity distribution.
- Air is considered an ideal gas.
- Steady-state regime.
- Constant thermo-physical properties for the solid phase.
- For simplicity, the local conduction between the solid and fluid phases is neglected; ergo $\frac{\partial}{\partial x_j}(\frac{1}{\Delta V}\int_{A_i} \mathbf{n}\lambda_f T_f ds_i)$.

Finally, to validate the solver developed, a comparison was made by adjusting the model parameters to the analysis presented in 2000 by Alazmi and Vafai (2000). In their analysis,

simpleFoam: parameters and variables

- Momentum Equation
  - Velocity (U) and Pressure (P)
  - Viscosity (μ)

SgenPorousSimpleFoam: parameters and variables

- Momentum Equation
  - Velocity (U) and Pressure (P)
  - Viscosity (μ)
  - Porosity (ϕ)
  - Hydrodynamic resistance terms (k_1 and k_2)
- Fluid Energy Equation
  - Fluid temperature (T_f)
  - Specific heat (c_p)
  - Fluid conductivity (λ_f)
  - Volumetric heat transfer coefficient ($h_v = h_i a_i$)
  - Density (ρ_f)
- Solid Energy Equation
  - Solid temperature (T_s)
  - Solid conductivity (λ_s)
- Entropy Equation
  - LEG rate by the conductive heat transfer ($\dot{s}_{\Theta,C}$)
  - Entropy generation rate due the volumetric heat transfer ($\dot{s}_{\Theta,V}$)
  - LEG rate due to viscous dissipation ($\dot{s}_{\Phi,D}$)
  - LEG rate associated to hydrodynamic resistance ($\dot{s}_{\Phi,DF}$)

Figure 5.3: SgenPororusSimpleFoam case directory.

several models of transport phenomena for heat exchange in porous media are applied in a 2D simulation of a porous channel and then compared. Figure 5.4 shows the axial profile of dimensionless temperature for each phase (fluid and solid), located at $X = 0.1$, where $X = H/L$ is the dimensionless distance in the flow direction. The results are in good agreement with those from the work of Alazmi and Vafai (2000).

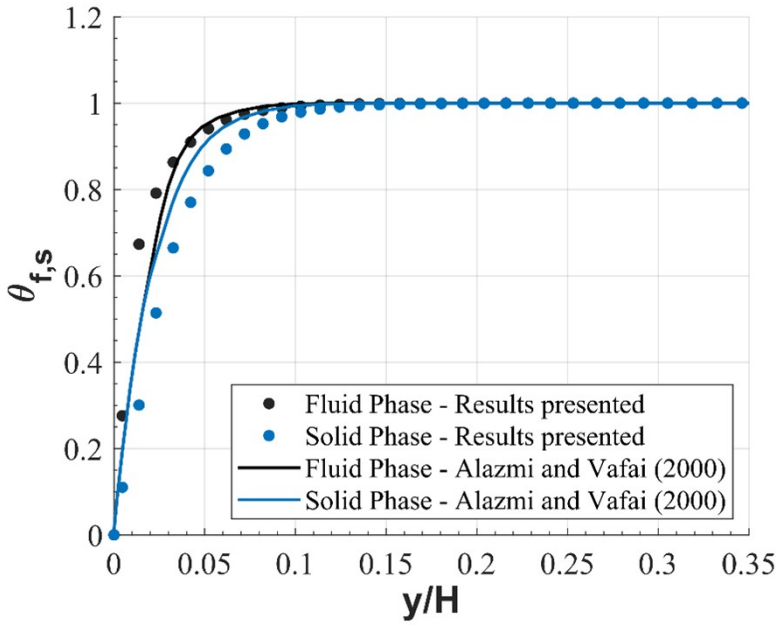

Figure 5.4: Axial dimensionless temperature distribution considering NTE heat transfer. $\phi = 0.6$, $Da = 10^{-4}$, $d_p = 0.008(m)$, $k_s/k_f = 25$, $Re_D = 1000$. (Sarmiento-Laurel et al., 2022)

5.2 Case of study: 2D Porous Heat Exchanger

5.2.1 System Description

The physical-mathematical model and the methodology presented in Chapter 4 define a way to study the entropy transport in porous energy exchange devices and, in addition, to know its performance through the spatial distribution of the LEG rate. By determining the LEG, it is possible to recognize the weak points of the system and establish modifications or key decisions in the design that allow for the best use of the available energy resource. As reviewed in Chapter 1, entropy generation is proposed as a measure associated with the inefficiencies of a process or, in the words of Clausius and Carnot (Carnot, 1824b; Clausius, 1879), with the degradation of the energy potential available in an energy reservoir. Thus, the proposed methodology and its subsequent implementation in a CFD analysis offer an analysis tool for design optimization in devices that incorporate porous media into their design. Consequently, to ground the concepts reviewed in Chapter 4, in this chapter a numerical experiment is developed on a basic but illustrative case, which allows showing the applications and potential of the proposed methodology.

For the implementation of the mathematical model that describes the LEG rate, an application for CFD simulation was developed in the OpenFOAM V9 (2021) software. This application was developed exclusively for this work, incorporating the terms of volumetric energy transfer and hydraulic resistance in the transport equations to be solved. With respect to the numerical experiment, a case in two dimensions was studied as a starting point for the use of this tool. The case study consists of an air flow through a porous channel under different boundary conditions: the temperature difference between both phases at the entrance of the channel and the entrance speed. Similarly, a simple case study was chosen in terms of geometry, but fast in terms of computational cost, to make a wide sweep in the boundary conditions and flow regimes. Thus, the results can be a starting point for other more detailed analyses of technological applications, such as packed rock-bed thermal storage or volumetric solar receivers.

The temperatures of the solid and the fluid are fixed at the entrance, as shown in Figure 5.5. For the complete parametrical analysis described in the following sections, the inlet fluid temperature is fixed at 300 K, and the temperature difference with the solid inlet varies from 0 to 1000 K. The temperatures of the upper and lower walls are set as the average between the solid and fluid inlet temperatures, as follows.

$$T_w = \frac{T_{f,\text{in}} + T_{s,\text{in}}}{2} \tag{5.7}$$

Additionally, Table 5.1 summarizes the key physical parameters considered for the analysis. Finally, the solving tolerance for the residuals was fixed at 10^{-7}, considering a grid resolution of 500×1000 elements, as shown in Figure 5.6. The turbulent effects were determined through the $k-\varepsilon$ equations of the RAS turbulence library considering the following constants: $C_\mu = 0.09$, $\sigma_k = 1$, $\sigma_\varepsilon = 1.3$, $C_{1\varepsilon} = 1.44$, and $C_{2\varepsilon} = 1.92$.

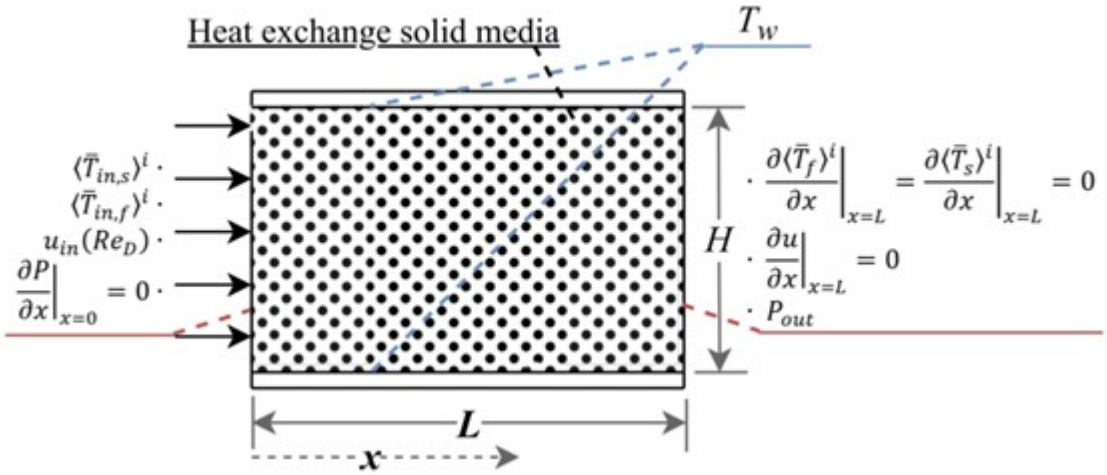

Figure 5.5: Case of study diagram (Sarmiento-Laurel et al., 2022)

Table 5.1: Analysis parameters

	Value
System Parameter	
Pore diameter (d_p)	0.0015 m
Channel height (H)	0.05 m
Channel length (L)	0.05 m
Type of fluid	Air (Ideal Gas)
Solid medium	Ceramic Foam (Wu et al., 2011b)
Thermal conductivity of the solid (λ_s)	80 $\mathrm{Wm^{-1}K^{-1}}$
Simulation Parameters	
Fluid inlet temperature $\langle \bar{T}_{f,in} \rangle^i$	300 K
Solid inlet temperature $\langle \bar{T}_{s,in} \rangle^i$	from 301 to 1300 K
Turbulent Prandtl number (Pr_t)	0.9
Outlet pressure (p_{out})	101.3 kPa
Reynolds number (Re_D)	from 1 to 1000

5.2.2 Boundary conditions

To solve the momentum and continuity equation system, the inlet velocity and the outlet pressure are considered as fixed values. Likewise, to solve the energy equation system, the inlet and wall temperatures of the solid and fluid phases are fixed values. Finally, on the domain boundaries, the gradient is set to zero for the following variables, as seen in Figure 5.5.

$$\left.\frac{\partial u_1}{\partial x}\right|_{x=L} = \left.\frac{\partial P}{\partial x}\right|_{x=0} = \left.\frac{\partial \langle \bar{T}_f \rangle^i}{\partial x}\right|_{x=L} = \left.\frac{\partial \langle \bar{T}_s \rangle^i}{\partial x}\right|_{x=L} = 0 \tag{5.8}$$

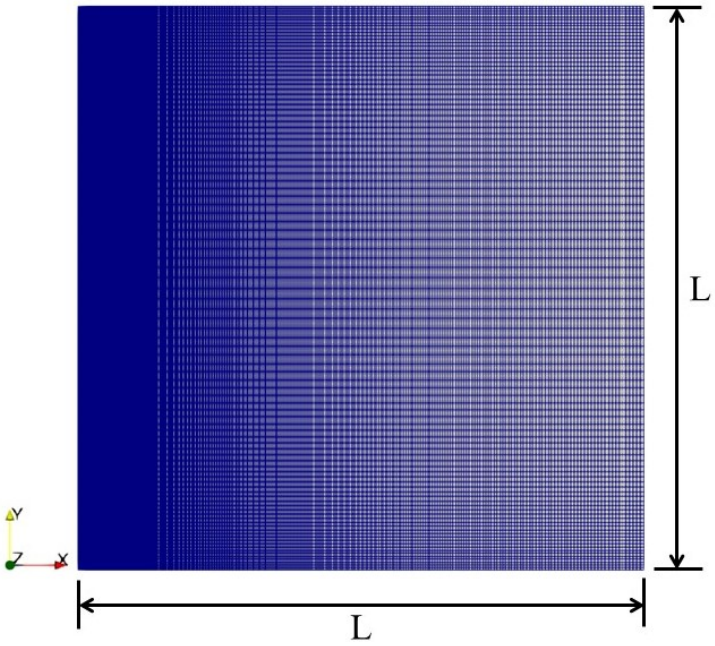

Figure 5.6: blockMesh algebraically generated grid

5.3 Dimensionless Analysis

From the development performed in Chapter 4, there is a detailed expression for each LEG mechanism on Eq.5.6. From this, it is reasonable to conduct a preliminary dimensionless analysis. As a prelude to numerical analysis in CFD, a dimensionless analysis provides more information about the significance of each LEG mechanism in the studied system under the established boundary conditions. Consequently, this section shows the development of the LEG equation presented in detail in Chapter 4 in its dimensionless version. In addition, the most relevant factors or dimensionless numbers in each LEG mechanism are recognized.

The dimensionless analysis was developed considering the following dimensionless variables:

$$
\begin{aligned}
{}^{*}x_i &= \frac{x_i}{H}, {}^{*}\bar{u}_i = \frac{\bar{u}_i}{U_0} \\
\theta_f &= \frac{T_f - T_{f,\text{in}}}{T_w - T_{f,\text{in}}}, \gamma_f = \frac{T_{f,\text{in}}}{T_w - T_{f,\text{in}}} \\
\theta_s &= \frac{T_s - T_{s,\text{in}}}{T_w - T_{s,\text{in}}}, \gamma_s = \frac{T_{s,\text{in}}}{T_w - T_{s,\text{in}}}
\end{aligned}
$$

where ${}^{*}x_i$ is the dimensionless longitude, ${}^{*}\bar{u}_i$ is the dimensionless velocity, U_0 is the inlet velocity, θ is the dimensionless temperature difference, and γ is the dimensionless inlet temperature. The subscripts f and s denote the fluid and solid phases, respectively. Thus, as it was proposed by Betchen and Straatman (2008), the dimensionless LEG term is written as follows:

$$
{}^{*}\langle \dot{s}_{\text{gen},f} \rangle^{v} = \frac{\langle \dot{s}_{\text{gen},f} \rangle^{v} H^2}{\lambda_f} \tag{5.9}
$$

$$ {}^{*}\langle \dot{s}_{\mathrm{gen},f} \rangle^{v} = {}^{*}\left\langle \dot{s}_{\Theta,\bar{C}} \right\rangle^{v} + {}^{*}\langle \dot{s}_{\Theta,C'} \rangle^{v} + {}^{*}\dot{s}_{\Theta,V} + {}^{*}\left\langle \dot{s}_{\Phi,\bar{D}} \right\rangle^{v} + {}^{*}\langle \dot{s}_{\Phi,D'} \rangle^{v} + {}^{*}\dot{s}_{\Phi,DF} \tag{5.10} $$

where ${}^{*}()$ refers to a dimensionless expression. Then, substituting the dimensionless properties on the Eq. 4.19, yields:

$$ \begin{aligned} &{}^{*}\left\langle \dot{s}_{\Theta,\bar{C}} \right\rangle^{v} + {}^{*}\langle \dot{s}_{\Theta,C'} \rangle^{v} + {}^{*}\dot{s}_{\Theta,V} \\ &\quad = \left(\frac{\phi \lambda_f H^2}{\lambda_f (\theta_f + \gamma_f)^2 H^2} + \frac{\rho_f c_{p,f} \mu_{t\phi} H^2}{\lambda_f (\theta_f + \gamma_f)^2 H^2} \right) \times \left[\left(\frac{\partial \theta_f}{\partial^{*} x} \right)^2 + \left(\frac{\partial \theta_f}{\partial^{*} y} \right)^2 + \left(\frac{\partial \theta_f}{\partial^{*} z} \right)^2 \right] \\ &\qquad + \frac{h_i a_i H^2}{\lambda_f (\theta_f + \gamma_f)} [(\theta_s + \gamma_s) - (\theta_f + \gamma_f)] \end{aligned} \tag{5.11} $$

Regrouping terms,

$$ \begin{aligned} &{}^{*}\left\langle \dot{s}_{\Theta,\bar{C}} \right\rangle^{v} + {}^{*}\langle \dot{s}_{\Theta,C'} \rangle^{v} + {}^{*}\dot{s}_{\Theta,V} \\ &\quad = \left(\frac{\phi \lambda_f + \lambda_{t\phi,f}}{\lambda_f (\theta_f + \gamma_f)^2} \right) {}^{*}\langle \Theta \rangle^{i} + \frac{\mathrm{Nu}_H (a_i H)}{(\theta_f + \gamma_f)} [(\theta_s + \gamma_s) - (\theta_f + \gamma_f)] \end{aligned} \tag{5.12} $$

where $Nu_H = \frac{h_i H}{\lambda_f}$ is the Nusselt number based on the channel high H, $\lambda_{t\phi,f}$ is the fluid turbulent thermal conductivity, and ${}^{*}\langle \Theta \rangle^{i}$ is the volume-averaged thermal diffusion term.

Analogously, for the viscous and Darcy-Forchheimer terms in Eq. 4.20:

$$ \begin{aligned} &{}^{*}\left\langle \dot{s}_{\Phi,\bar{D}} \right\rangle^{v} + {}^{*}\langle \dot{s}_{\Phi,D'} \rangle^{v} \\ &\quad = \frac{2\mu\phi {U_0}^2 H^2}{\lambda_f (\theta_f + \gamma_f) H^2} \left[\left\langle \left(\frac{\partial^{*} \bar{u}_i}{\partial^{*} x_j} + \frac{\partial^{*} \bar{u}_j}{\partial^{*} x_i} \right)^2 + \left(\frac{\partial^{*} \bar{u}_k}{\partial^{*} x_k} \right)^2 \right\rangle^{i} \right. \\ &\qquad \left. + \left\langle \overline{\left(\frac{\partial^{*} {u_i}'}{\partial^{*} x_j} + \frac{\partial^{*} {u_j}'}{\partial^{*} x_i} \right)^2} + \overline{\left(\frac{\partial^{*} {u_k}'}{\partial^{*} x_k} \right)^2} \right\rangle^{i} \right] \end{aligned} \tag{5.13} $$

$$ {}^{*}\left\langle \dot{s}_{\Phi,\bar{D}} \right\rangle^{v} + {}^{*}\langle \dot{s}_{\Phi,D'} \rangle^{v} = \frac{\mathrm{PrEc}}{(\theta_f + \gamma_f)} {}^{*}\langle \Phi \rangle^{i} \tag{5.14} $$

$$ {}^{*}\dot{s}_{\Phi,DF} = \frac{\phi H^2}{\lambda_f (\theta_f + \gamma_f)} \left(\frac{\mu {U_0}^2}{k_1} + \frac{\rho_f {U_0}^3}{k_2} |\overline{{}^{*}u_D}| \right) \overline{{}^{*}u_D}^2 \tag{5.15} $$

$$ {}^{*}\dot{s}_{\Phi,DF} = \frac{\mathrm{PrEc}}{(\theta_f + \gamma_f)} \left(\frac{1}{\mathrm{Da}} + \frac{\mathrm{Re}_H}{\sqrt{\mathrm{Da}}} |\overline{{}^{*}u_D}| \right) \overline{{}^{*}u_D}^2 \tag{5.16} $$

where $Re_H = u_D H/\mu$ is the Reynolds number based on the channel high H, $Da = K/{d_p}^2$ is the Darcy number, $Pr = \mu c_{p,f}/\lambda_f$ is the Prandtl number, and $Ec = {U_o}^2/(c_{p,f}(T_w - T_{f,in}))$ is the Eckert number.

Finally, the following equation shows the complete expression of ${}^*\langle \dot{s}_{gen,f} \rangle^v$ considering all the mechanisms of LEG, such as heat conduction, volumetric heat transfer, viscous effects, and hydrodynamic resistance.

$$
\begin{aligned}
{}^*\langle \dot{s}_{\mathrm{gen},f} \rangle^v = & \underbrace{\left(\frac{\phi\lambda_f + \lambda_{t\phi,f}}{\lambda_f(\theta_f + \gamma_f)^2} \right)}_{N_{\mathrm{CHT}}} {}^*\langle \Theta \rangle^i + \underbrace{\frac{\mathrm{Nu}_H(a_i H)}{(\theta_f + \gamma_f)}}_{N_{\mathrm{VHT}}} [(\theta_s + \gamma_s) - (\theta_f + \gamma_f)] \\
& + \left(\underbrace{\frac{\mathrm{PrEc}}{(\theta_f + \gamma_f)}}_{N_V} {}^*\langle \Phi \rangle^i + \underbrace{\frac{\mathrm{PrEc}}{(\theta_f + \gamma_f)\mathrm{Da}}}_{N_D} + \underbrace{\frac{\mathrm{PrEcRe}_H}{(\theta_f + \gamma_f)\sqrt{\mathrm{Da}}}}_{N_{\mathrm{FH}}} |\overline{{}^*u_D}| \right) \overline{{}^*u_D}^2
\end{aligned}
\tag{5.17}
$$

From the equation Eq. 5.17 it is possible to identify the key factors that define the impact of macroscopic conduction heat transfer (N_{CHT}), volumetric heat transfer ($N_V HT$), viscous effects (N_V), and Darcy-Forchheimer hydrodynamic resistances (N_D and N_{FH}).

5.4 Results and discussion

The dimensionless LEG term in Eq. 5.17 shows five key factors which define the magnitude of each entropy generation mechanism. Figure 5.7 shows the results of the post-processed LEG, including the variation of the two most significant parameters, comparing their development under different porosities, temperatures, and ranging the porous Reynolds number from 10 to 1000 (laminar and turbulent).

As shown in Figure 5.7, the heat transfer dimensionless factors were analyzed ranging the inlet temperature difference ΔT from 10 to 1000 K. The heat conduction factor N_{CHT} and the volumetric heat transfer factor N_{VHT} reach their highest values about 3 and 6 magnitude orders, respectively, when the Reynolds number is over 200; and reach their maximum value for $\phi = 0,9$ at $\Delta T = 1000$ K. As expected, the volumetric heat transfer dominates the heat transfer of LEG and reaches it maximum value for higher porosities, which it is translated as higher exchange areas. Nevertheless, a CFD analysis is necessary to conclude the influence of each mechanism and to determine its spatial distribution, because the two phenomena obey to different temperature fields. The conduction obeys to the fluid field temperature and the volumetric heat transfer to the interaction phenomenon between the two phases.

Analogously, Figure 5.8 shows the same dimensionless analysis applied to the viscous and hydrodynamic mechanisms of the LEG. Due to the low viscosity that the working fluid (air) exhibits in the full range of analysis, the viscous LEG is negligible for all cases. The same effect occurs for Darcy's viscous hydrodynamic resistance, which is negligible for the complete domain analyzed. On the other hand, Forchheimer's hydrodynamic resistance does present a significant impact on the LEG. The value of N_{FH} reaches 9 magnitude orders for porosity of 0.1. In low porosity configurations, the fluid is constantly impinging on the solid matrix, significantly increasing the amount of useless work done by the flow over the porous media.

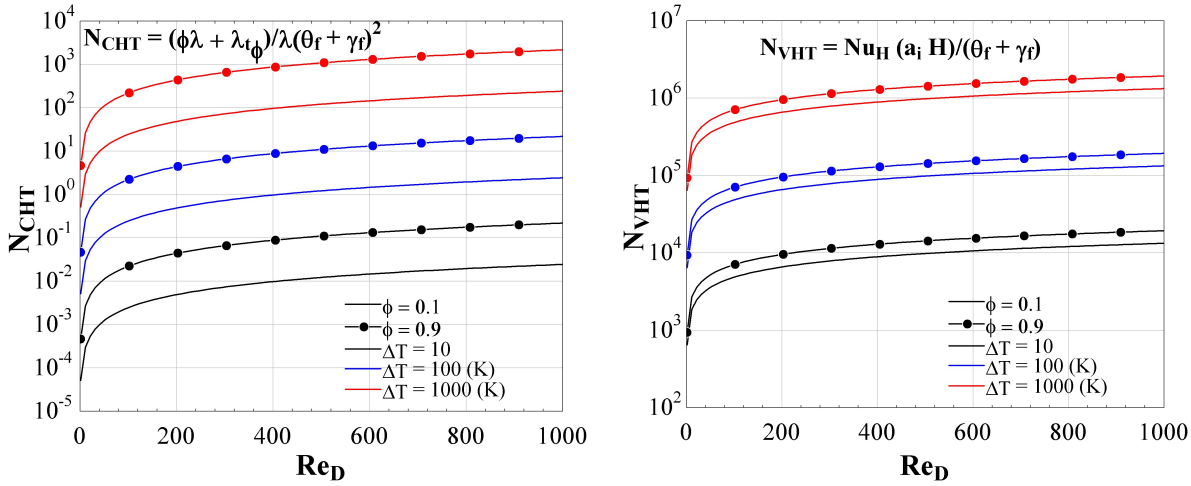

Figure 5.7: Heat transfer dimensionless factors, from laminar to turbulent porous Reynolds regimes.

Summarizing the dimensionless analysis of each LEG mechanism in Figure 5.7 and Figure 5.8, the maximum values of each magnitude factor are: $N_{CHT} < 2 \times 10^3$, $N_{VHT} < 2 \times 10^6$, $N_V < 10^{-1}$, $N_D < 10^{-7}$, $N_{FH} < 10^{10}$. Hydrodynamic effects are usually neglected in entropy generation analyzes (Bejan, 1995). Nevertheless, the magnitude of the Forchheimer's hydrodynamic term expressed trough N_{FH}, makes it necessary to consider its effect at the differential scale CFD analyses, in either laminar or turbulent regimes. Figure 5.9 shows the distribution of N_{VHT}/N_{FH} to compare the impact of each LEG mechanism on the different ranges of analysis (porosity, temperature difference, and porous Reynolds regime).

In Figure 5.9 it is possible to recognize the inflection points where Forchheimer's hydrodynamic resistance dominates the LEG compared to the volumetric heat transfer. For a porosity of 0.1, the magnitude of N_{FH} dominates for Re_D greater than 13.43, 29.92, and 36.62, for ΔT of 10, 100, and 1000 K, respectively. For higher porosities, 0.5 and 0.9, the volumetric heat transfer phenomenon dominates the LEG rate, but it is necessary to perform a numerical CFD analysis to define with precision the regions in the domain where each mechanism dominates over the others.

Consequently, a CFD analysis was performed to adjust the preliminary results in Figure 5.9. On the upper-side, Figure 5.10 shows the axial mean temperature profile for solid and fluid phases for two cases (of the 200 configurations analyzed) with the same Re_D and inlet temperature difference, and considering different porosities. There, the thermal equilibrium is reached for a higher porosity ($\phi = 0.8$), because a higher porosity implies a greater heat exchange area. Similarly, at the bottom-side of Figure 5.10, shows the LEG distribution along the porous heat exchanger considering the previously mentioned porosities. There, it is possible to recognize the inflection points where the LEG by volumetric heat transfer ceases to predominate over the LEG associated with the Darcy and Forchheimer hydraulic resistance, which occurs. The inflection occurs at $x/L = 0.094$ when $S_{gen} = 448.572(WK^{-1}m^{-3})$, and at $x/L = 0.036$ when $S_{gen} = 19.282(kWK^{-1}m^{-3})$, for porosities of 0.4 and 0.8 respectively. This inflection is due to the thermal equilibrium that has been reached at this critical point,

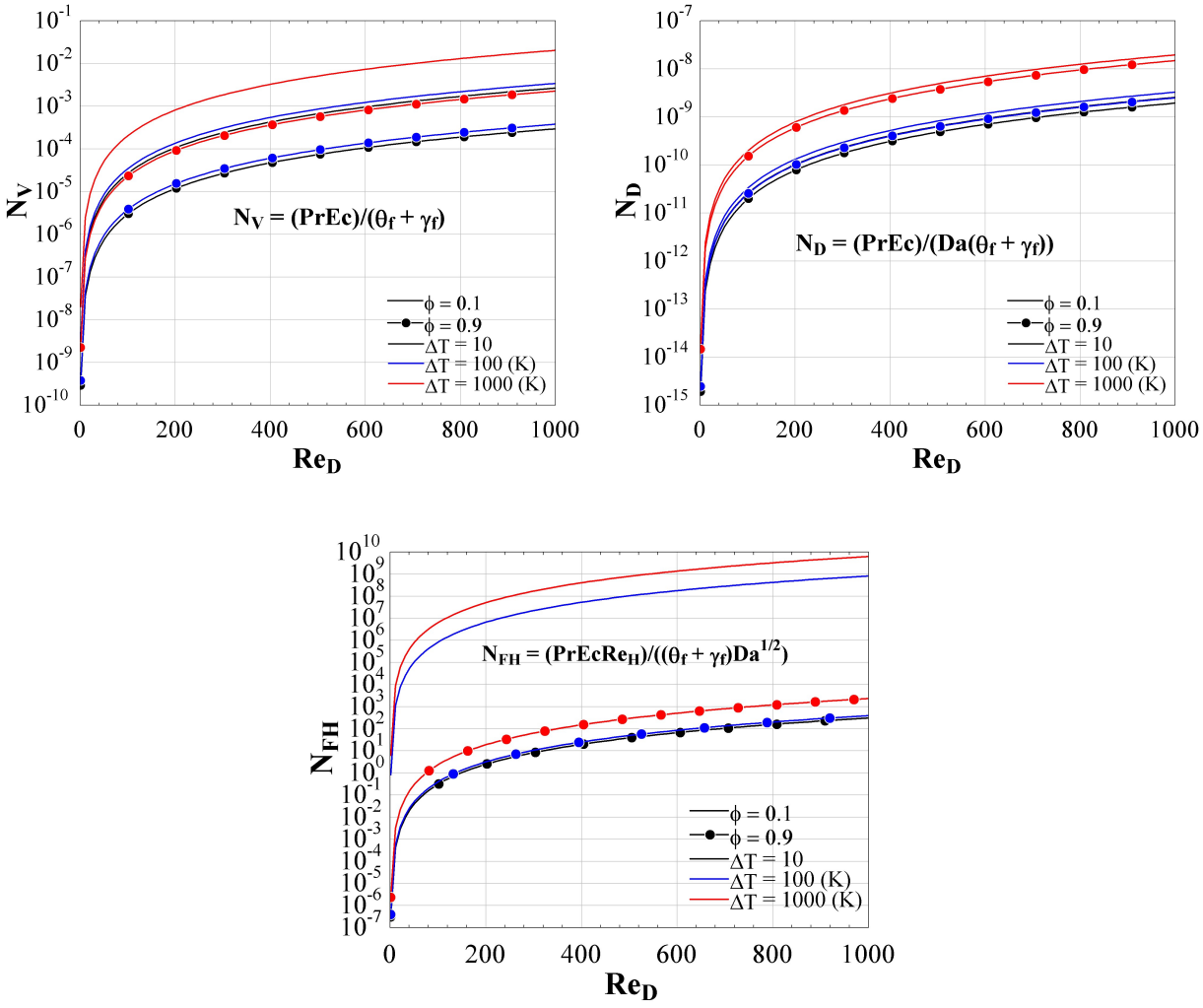

Figure 5.8: Viscous dissipation, Darcy's, and Forchheimer's hydrodynamic resistances dimensionless factors, from laminar to turbulent porous Reynolds regimes.

and consequently, the LEG due to volumetric heat exchange decreases significantly. From this, areas where some LEG mechanism dominates over others are recognized, and this can be strongly related to design parameters, operation, or characteristics of the porous medium or fluid.

From the two systems studied in Figure 5.10, Figure 5.11 presents the total spatial distribution of LEG. There, two zones can be recognized, a high LEG near the inlet and a stabilization value for the LEG at the point of thermal equilibrium. Downstream of the inflection point, the level of LEG is dominated by the hydraulic resistance mechanism, which, in other words, is strongly related to the porosity. Furthermore, by integrating the LEG into the entire control volume, the LEG in both cases is displayed in Figure 5.11. The volumetric heat transfer LEG is $\dot{S}_{\Theta,V} = 0.0247(WK^{-1})$, hydrodynamic resistance LEG $\dot{S}_{\Phi,DF} = 0.2379(WK^{-1})$, and the total LEG $\dot{S}_{gen} = 0.2627(WK^{-1})$, for $\phi = 0.4$; analogously, the $\dot{S}_{\Theta,V} = 0.0892(WK^{-1})$, $\dot{S}_{\Phi,DF} = 0.0058(WK^{-1})$, and $\dot{S}_{gen} = 0.0950(WK^{-1})$, for $\phi = 0.8$. Therefore, there are porosity configurations where the LEG due to hydraulic resistance can be

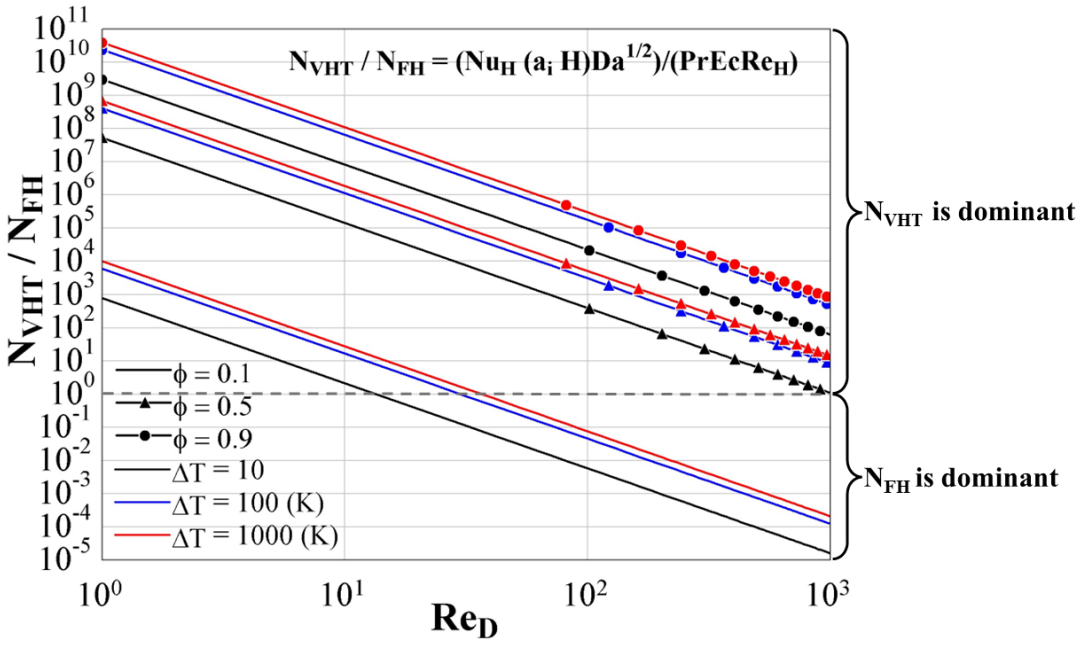

Figure 5.9: Comparison of dimensionless volumetric heat transfer against the Forchheimer's hydrodynamic resistance effect over the LEG

greater than the LEG associated with heat transfer, which is contrary to what is commonly expected. From this idea, the following results show a sweep through different cases varying the design and operation parameters, to study the total LEG and the predominance of its generation mechanisms.

From the LEG distribution presented in figure Figure 5.10, it is interesting to note that the LEG can vary its spatial distribution in the flow direction, establishing zones and, additionally, these zones can be dominated by one or another LEG mechanism. On the other hand, the LEG mechanisms are usually linked to different operating or design conditions, such as temperature or porosity, respectively. Therefore, it is possible to develop design strategies for entropy generation minimization, from the results of a spatial analysis of the LEG distribution. Thus, a design strategy can define the operating and design conditions for each zone as a function of the most significant LEG mechanism. For this, it is necessary to perform a detailed CFD analysis of a particular geometry on a technological application.

However, the phenomenon mentioned above could be due to a particular case within multiple contour or design configurations, which can be associated with different porous devices for storage, heat exchange, or energy generation. In other configurations of operation, design, or materials, other LEG mechanisms could dominate, such as hydraulic resistance or viscous dissipation. In consequence, the present analysis focuses on studying a wide range of operating configurations in order to guide future analyses aimed at devices in particular, such as hydrogen reactors, TES, VSR, among others. Then Figure 5.12 shows the computational results for 200 CFD cases under different boundary conditions and operating configurations, ranging the porosity of the solid matrix from 0.2 to 0.8, and the solid-fluid inlet temperature difference from 0 to 1000 K. These results could be useful for low-temperature configurations as sensible thermal energy storages and for high-temperature differences as VSR. N_{Sgen} compares the integrated LEG in the entire volume of heat transfer with viscous

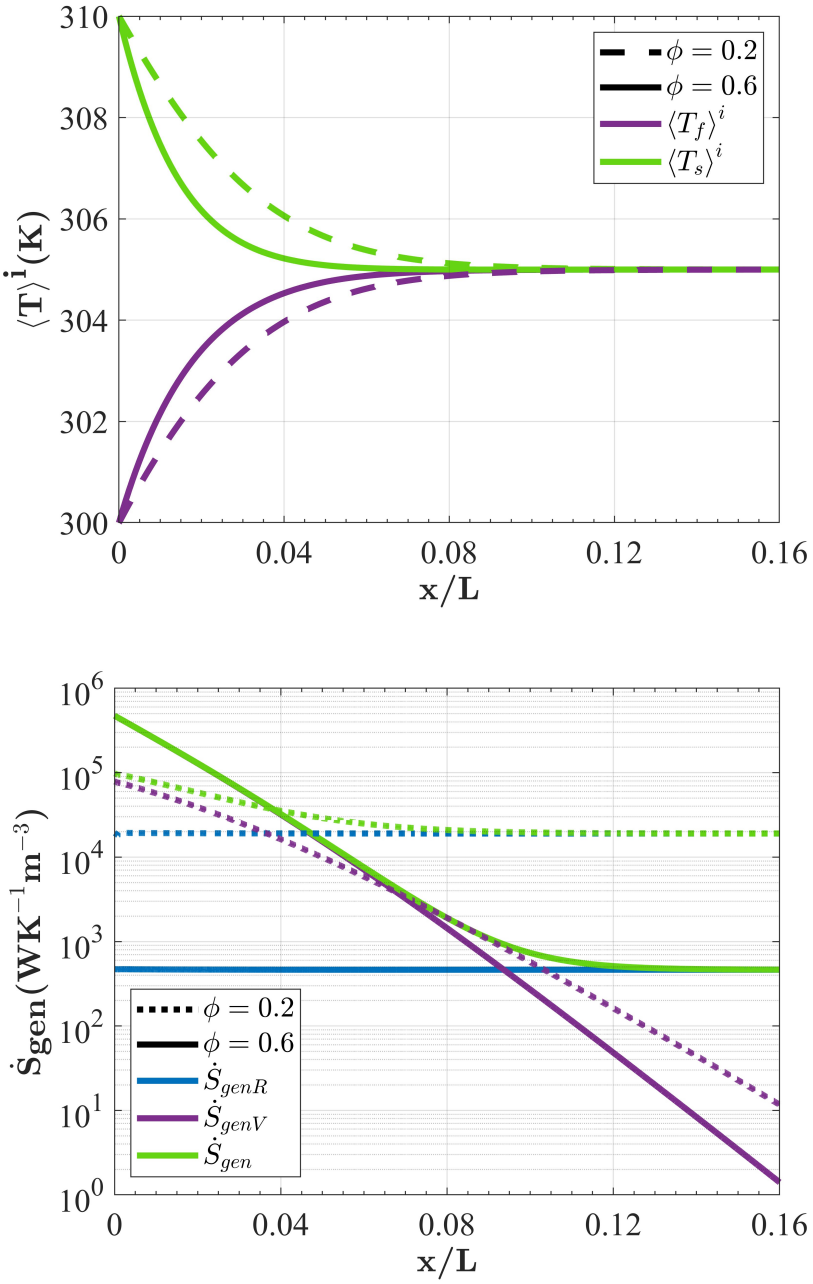

Figure 5.10: a) Mean axial temperature profile for porosities of 0.4 and 0.8; b) Longitudinal LEG profile for porosities of 0.4 and 0.8. Both cases consider $Re_D = 400$ and $\Delta T_{in} = 10$ K.

and hydrodynamic resistances (Annex (A.5)).

Similarly to the results shown in the previous dimensionless analysis, inflection points are recognized where the hydrodynamic effects are more relevant than the heat transfer LEG mechanisms. The red line in Figure 5.12 remark that the points were N_{Sgen} is equal to 1. It is interesting to note that the hydrodynamic LEG mechanisms are dominant in several configurations, which is unexpected. Thus, Forchheimer's effects are more relevant under higher porous Reynolds regimes, and its influence decreases with porosity. Taking into

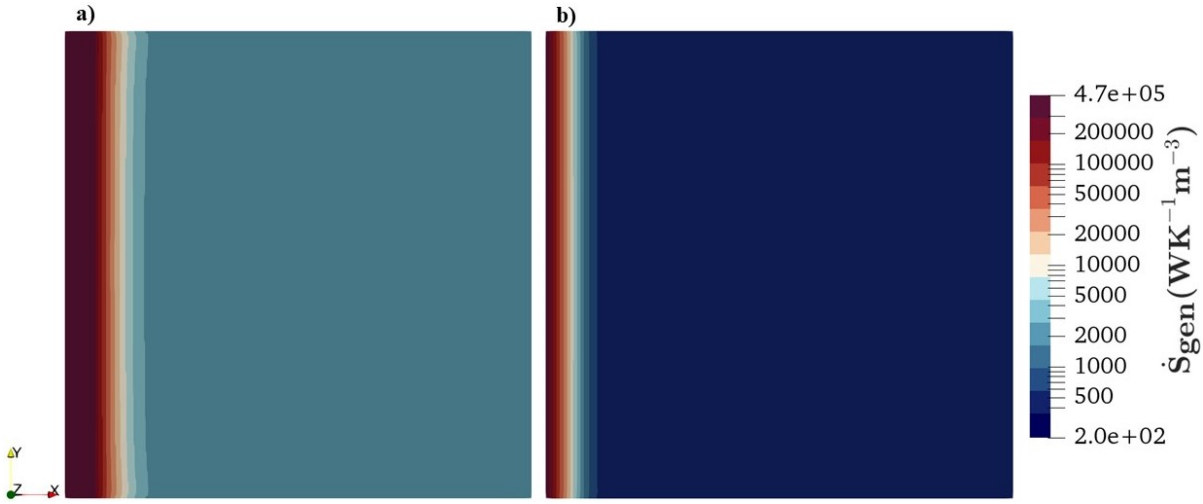

Figure 5.11: Total LEG distribution for $Re_D = 400$ and $\Delta T_{in} = 10$ K, considering a) $\phi = 0.4$, and b) $\phi = 0.8$.

account cases where the temperature difference is below 100 K (normal in TES operation), the inflection points are Re_D of 15, 100, 600, and 1000 for porosities of 0.2, 0.4, 0.6, and 0.8, respectively. These ranges of ΔT are commonly observed in sensible TES, where the temperature differences between the solid and fluid phases are below 100 K, for charge and discharge cycles. Consequently, at porosities below 0.4 the hydrodynamic resistance is dominant in laminar and turbulent regimes (turbulent: $Re_D \geq 300$). On the other hand, at porosities over 0.4 the hydrodynamic resistances are relevant only for turbulent regimes. Therefore, since the design of thermal storage considers porosities of around 0.4, it is necessary to consider the hydraulic resistance in the simulation and subsequent second law analysis, to minimize the entropy generation. Analogously, for ΔT greater than 100 K, the LEG mechanisms by heat transfer dominate under laminar and turbulent regimes for porosities higher than 0.6. These configurations are usually observed on VSR systems where the porosities are around 0.8 and the temperature differences on the inlet are close to 1000 K. Therefore, it is recommended to focus on minimizing LEG by heat transfer to optimize the thermodynamic performance of the VSR.

The entropy generation as a figure of merit allows one to distinguish the weak points of a particular design to focus efforts on the design task. Likewise, if the different generation mechanisms are recognized, it is possible to make a detailed optimization of the design and the operation conditions for systems of storage, generation, and transfer energy. Consequently, Figure 5.13 shows the entropy generation integrated in the control volume for different operating conditions in terms of the Reynolds number and the temperature difference at the inlet of the porous channel. Although Figure 5.12 recognized some inflection points where one mechanism of LEG may predominate over another, it is also important to account for how much entropy is generated (associated irreversibilities) in each case. Thus, it is possible to recognize critical cases and, in such cases, define which mechanism dominates the LEG and in which zone it is located.

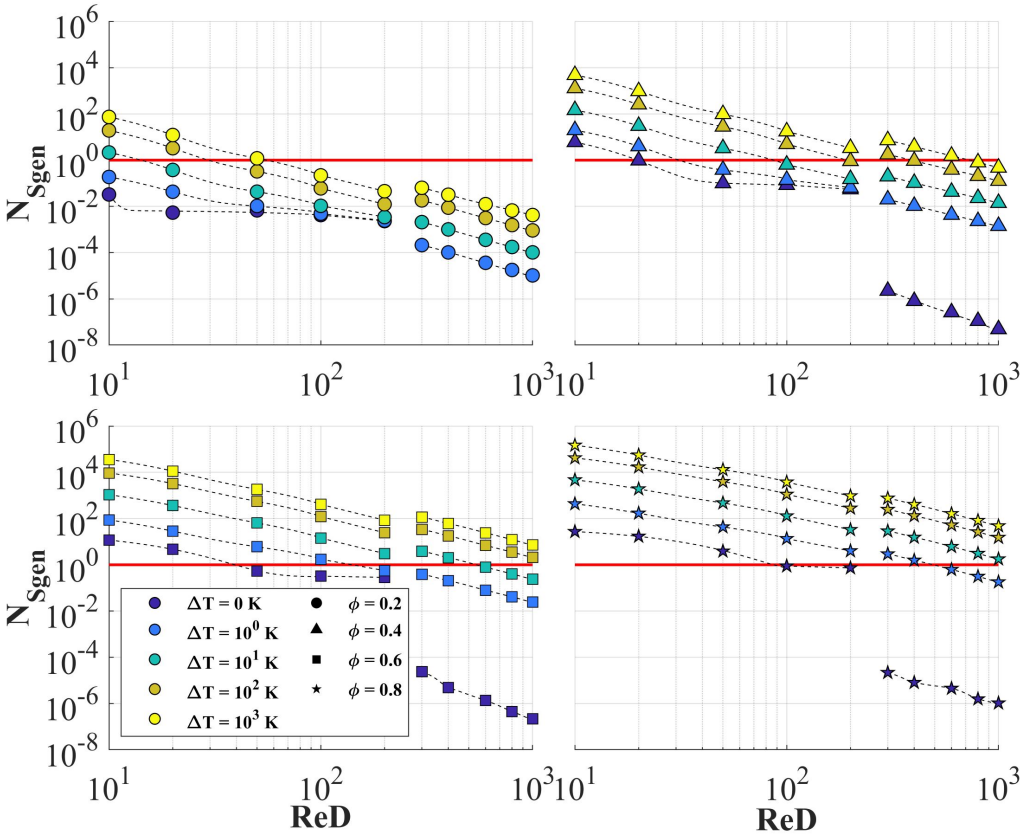

Figure 5.12: Comparison factor for the volumetric heat transfer against the Forchheimer's hydrodynamic resistance effect over the LEG.

In Figure 5.13 the entropy rate reaches its maximum value of 825.18 W/K for a porosity of 0.2, with a low variation related to the temperature difference at the entrance. This is due to the high impact of the hydrodynamic resistance on the LEG rate, presented in Figure 5.12. Likewise, the case of porosity of 0.2 shows the largest increase in entropy generation as the Reynolds number increases, reaching an increase of 4 orders of magnitude. This is because a lower porosity means a large area of solid obstructing the flow path. For a porosity of 0.4, a similar trend to the previous case is achieved from Reynolds numbers greater than 100 (inflection point for that porosity). A similar trend is observed at porosity of 0.4 where the largest increase in the entropy generation is in the cases where the hydraulic resistance dominates at Reynolds numbers greater than 100 ($Re_D \geq 100$). For Reynolds below 100, the main increase of entropy generation is dominated by the temperature difference between both media at the inlet, mainly associated with the sold-fluid volumetric heat transfer. Finally, for porosities over 0.6 the total entropy generation in the volume does not increase significantly with the Reynolds number. The entropy generation in this last range is strongly linked to the temperature difference between both media.

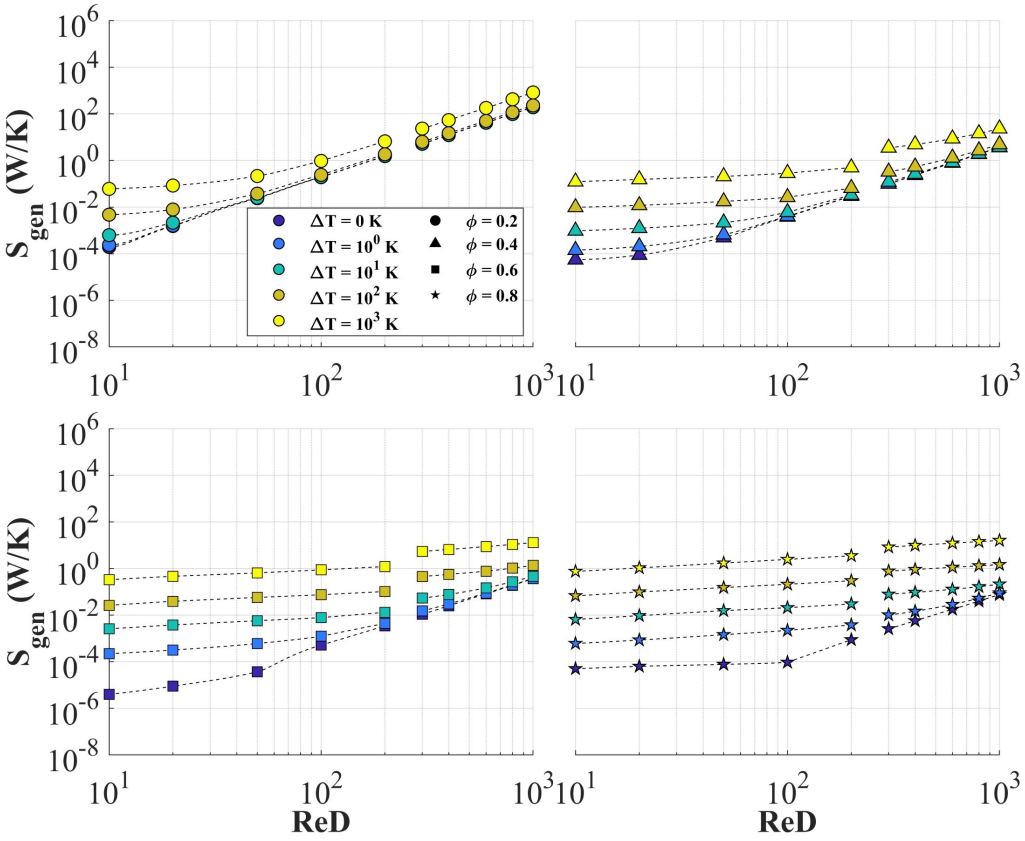

Figure 5.13: Total LEG rate integrated for the complete volume.

Chapter 6

Conclusions

A study of the energy and entropy transport in porous media was developed. The analysis considers Reynolds' time-averaging and the spatial volume-averaging methods to develop an entropy transport equation for fluid flow in a porous medium, under laminar to turbulent regimes. A physical and mathematical methodology was proposed to determine the LEG from the formulated thermo-physical local entropy transport model (Eq. 4.11). The methodology was developed to determine the LEG rate as a post-process function from the velocity, temperature, k, and ε fields, commonly resulting from regular CFD analysis. The proposed methodology allows determining the LEG without solving an additional transport entropy equation. Furthermore, a dimensionless analysis was developed in the LEG model to determine the key dimensionless parameters that define the magnitude of each LEG mechanism recognized in this study: LEG by conduction, volumetric heat transfer, hydrodynamic resistance, viscous dissipation, and turbulent dissipation. Finally, a numerical experiment was developed to study and compare the dominance of the different LEG mechanisms, considering different configurations of inlet temperature, porosity, and flow regime. The results are proposed as a starting point for future CFD entropy analysis applied to solar thermal sensible heat storage systems, solar hydrogen generation reactors, and volumetric solar receivers, among others.

The LEG model allows studying the performance of a porous heat exchange device, distinguishing different LEG mechanisms (or irreversibility sources), such as momentum dissipation phenomena, porous hydraulic resistance, and heat transfer, in a single figure of merit. Therefore, it is possible to measure the disadvantages related to the pressure drop and viscous effects of a porous medium $\langle \dot{s}_{\Phi} \rangle^{v}$, and at the same time, determine the benefits related to the large heat exchange area related to the porous matrix. Furthermore, through the entropy concept, the most rational way to exchange thermal energy is recognized, distinguishing the level of irreversibilities $\langle \dot{s}_{\Theta} \rangle^{v}$ under different design and/or operation restrictions.

The presented model defines a physico-mathematical expression for each LEG mechanism, allowing to distinguish areas of significance where one mechanism may be more relevant than another. Therefore, it is possible to establish different design and/or operation strategies in terms of the type of LEG mechanism to be minimized. The proposed expression for the LEG is a starting point for future optimization work on the design of porous devices to minimize

the LEG or, in other words, its level of irreversibility.

The numerical experiment shows an analysis on a porous channel evaluated in 200 configurations for its boundary conditions, where the Reynolds number varies from laminar to turbulent regime, and the inlet temperature difference between the solid and porous phases varies from 1 to 1000 K. From the numerical results in a porous channel, the LEG rate can be dominated principally by volumetric heat transfer or hydrodynamic resistance entropy generation mechanisms. Also, at a temperature difference of 100 K, inflection points are observed. The inflection points establish the Re_D where both principal LEG mechanisms have equal significance in the global LEG rate. Inflection points are Re_D of 15, 100, 600, and 1000 for porosities of 0.2, 0.4, 0.6, and 0.8, respectively. For porosities below 0.4 the hydrodynamic resistance dominates in laminar and turbulent regimes (turbulent: $Re_D \geq 300$). Thus, it is concluded that the mechanism of entropy generation associated with hydraulic resistance is more significant for laminar and turbulent regimes in the design and optimization of thermal storage systems, which usually coincide with porosities close to 0.4. Analogously, for ΔT greater than 100 K, the LEG mechanism associated with volumetric heat transfer dominates under laminar and turbulent regimes for porosities greater than 0.6. Therefore, the entropy generation associated with the volumetric heat transfer LEG mechanism and its spatial distribution dominates in the global LEG and, consequently, in the optimization and design of high-temperature heat exchange systems such as VSR for CSP. It is usual for a VSR to consider porosities around 0.8 and temperature differences at the inlet from 1000 K.

An analysis based on a LEG model allows to recognize and compare the impact of all the irreversibility mechanisms in a single figure of merit, allowing to define the main focuses in the optimization procedure, during the design of porous media systems. From the model presented in this thesis, it is possible to localize spatially and define the dominant LEG mechanism for different areas in a porous device. Thus, it is possible to define design strategies in function of the different regions of the analysis and the restrictions of geometry and operation.

In future research, the proposed LEG expression and dimensionless parameters could be implemented to study more working fluids and porous media configurations (wire mesh, wool, packed bed, ceramic foam, etc.), allowing to optimize novel applications on storage, exchange, and generation of energy.

6.1 Future Work

The proposed theoretical model, the methodology, and its computational implementation help direct some promising lines of research, as follows.

Regarding exergoeconomic analysis, the proposed simulation tool and methodology open the possibility to extend the study of heat-exchanging porous devises to second-law analyses. The LEG expression allows access to entropy minimization and exergetic analyses on the design of a porous system for storage and exchange of energy. Currently, porous heat exchangers have interesting applications in volumetric receives for CSP systems and packed rock bed energy storage systems. However, the porous material, porosity, and geometry are

still a matter for discussion.

Because of their large exchange area, porous media have promising potential in applications for hydrogen and syngas production through inert porous media reactors. As in the previous point, the contributions of this doctoral work open the door to analysis and optimization through the minimization of entropy generation in reactors for hydrogen and syngas production.

Finally, the proposed expression for the LEG is a first step for the development of an expression that considers mass exchanges and changes in chemical potential. The latter could be a useful tool in the analysis and design of porous membrane desalination systems. The analysis of the LEG allows to determine a design that better manages the energy used for the generation of fresh water.

Bibliography

Alazmi, B. and Vafai, K. (2000). Analysis of variants within the porous media transport models. *J. Heat Transfer*, 122(2):303–326.

Andrienko, D. A. and Surzhikov, S. T. (2012). P1 approximation applied to the radiative heating of descent spacecraft. *J. Spacecr. Rockets*, 49(6):1088–1098.

Ávila-Marín, A. L. (2011). Volumetric receivers in solar thermal power plants with central receiver system technology: A review. *Solar Energy*, 85(5):891–910.

Avila-Marin, A. L., Caliot, C., Alvarez de Lara, M., Fernandez-Reche, J., Montes, M. J., and Martinez-Tarifa, A. (2019). Homogeneous equivalent model coupled with p1-approximation for dense wire meshes volumetric air receivers. *Renewable Energy*, 135:908–919.

Avila-Marin, A. L., Caliot, C., Flamant, G., Alvarez de Lara, M., and Fernandez-Reche, J. (2018). Numerical determination of the heat transfer coefficient for volumetric air receivers with wire meshes. *Solar Energy*, 162:317–329.

Ávila-Marín, A. L., Fernandez-Reche, J., and Martinez-Tarifa, A. (2019). Modelling strategies for porous structures as solar receivers in central receiver systems: A review. *Renewable Sustainable Energy Rev.*, 111:15–33.

Bai, F. (2010). One dimensional thermal analysis of silicon carbide ceramic foam used for solar air receiver. *Int. J. Therm. Sci.*, 49(12):2400–2404.

Baumann, A., Hoch, D., Behringer, J., and Niessner, J. (2020). Macro-scale modeling and simulation of two-phase flow in fibrous liquid aerosol filters. *Engineering Applications of Computational Fluid Mechanics*, 14(1):1325–1336.

Bejan, A. (1977). The concept of irreversibility in heat exchanger design: Counterflow heat exchangers for Gas-to-Gas applications. *J. Heat Transfer*, 99(3):374–380.

Bejan, A. (1978). Two thermodynamic optima in the design of sensible heat units for energy storage. *J. Heat Transfer*, 100(4):708–712.

Bejan, A. (1980). Second law analysis in heat transfer. *Energy*, 5(8):720–732.

Bejan, A. (1995). *Convection Heat Transfer*. John Wiley & Sons, 2 edition.

Bejan, A. (2002). Fundamentals of exergy analysis, entropy generation minimization, and the generation of flow architecture. *Int. J. Energy Res.*

Bejan, A. (2013). *Entropy generation minimization: the method of thermodynamic optimization of finite-size systems and finite-time processes*. CRC Press.

Bergles, A. E., Junkhan, G. H., and Bunn, R. L. (1976). Performance criteria for cooling systems on agricultural and industrial machines. *SAE Trans. J. Mater. Manuf.*, 85:38–47.

Betchen, L. J. and Straatman, A. G. (2008). The development of a Volume-Averaged Entropy-Generation function for nonequilibrium heat transfer in High-Conductivity porous foams. *Numerical Heat Transfer, Part B: Fundamentals*, 53(5):412–436.

Betchen, L. J. and Straatman, A. G. (2014). Entropy generation-based computational geometry optimization of the pore structure of high-conductivity graphite foams for use in enhanced heat transfer devices. *Comput. Fluids*, 103:49–70.

Calderón-Vásquez, I., Cortés, E., García, J., Segovia, V., Caroca, A., Sarmiento, C., Barraza, R., and Cardemil, J. M. (2021). Review on modeling approaches for packed-bed thermal storage systems. *Renewable Sustainable Energy Rev.*, 143:110902.

Cantwell, B. J. (2022). *Fundamentals of Compressible Flow*. Department of Aeronautics and Astronautics Stanford University, California.

Capuano, R., Fend, T., Schwarzbözl, P., Smirnova, O., Stadler, H., Hoffschmidt, B., and Pitz-Paal, R. (2016). Numerical models of advanced ceramic absorbers for volumetric solar receivers. *Renewable Sustainable Energy Rev.*, 58:656–665.

Carnot, S. (1824a). *Réfexions sur la puissance motrice du feu et sur le machines propres à développer cette puissance*. Bachelier.

Carnot, S. (1824b). *Reflections on the Motive Power of Heat (1824), English traslation by R.H. Thurston (1897)*. John Wiley and Sons, London.

Chen, X., Xia, X.-L., Yan, X.-W., and Sun, C. (2017). Heat transfer analysis of a volumetric solar receiver with composite porous structure. *Energy Convers. Manage.*, 136:262–269.

Clapeyron, E. (1834). Mémoire sur la puissance motrice de la chaleur , ,. *Journal de l'E cole Royale Polytechnique*, (14):153190.

Clausius, R. (1850). Ueber die bewegende kraft der wärme und die gesetze, welche sich daraus für die wärmelehre selbst ableiten lassen. *Annalen der Physik*, 155(3):368–397.

Clausius, R. (1856). On a modified form of the second fundamental theorem in the mechanical theory of heat. *The London, Edinburgh, and Dublin Philosophical Magazine and Journal of Science*, 12(77):81–98.

Clausius, R. (1879). *The Mechanical Theory of Heat with its Applications to the Steam-Engine and to the Physycal Properties of Bodies*. Taylor and Francis.

Cohen, I. M. and Kundu, P. K. (2004). *Fluid Mechanics*. Elsevier.

Currie, I. G. (2016). *Fundamental Mechanics of Fluids*. CRC Press.

de Lemos, M. J. S. (2012). *Turbulence in Porous Media: Modeling and Applications*. Elsevier.

de Lemos, M. J. S. and Pedras, M. H. J. (2001). Recent mathematical models for turbulent flow in saturated rigid porous media. *J. Fluids Eng.*, 123(4):935–940.

Dincer, I. and Rosen, M. A. (2012). *Exergy: Energy, Environment and Sustainable Development*. Newnes.

Du, S., Li, M.-J., Ren, Q., Liang, Q., and He, Y.-L. (2017). Pore-scale numerical simulation of fully coupled heat transfer process in porous volumetric solar receiver. *Energy*, 140:1267–1275.

Ergun, S. and Orning, A. A. (1949). Fluid flow through randomly packed columns and fluidized beds. *Ind. Eng. Chem.*, 41(6):1179–1184.

Esence, T., Bruch, A., Molina, S., Stutz, B., and Fourmigué, J.-F. (2017). A review on experience feedback and numerical modeling of packed-bed thermal energy storage systems. *Solar Energy*, 153:628–654.

Fend, T., Hoffschmidt, B., Pitz-Paal, R., Reutter, O., and Rietbrock, P. (2004a). Porous materials as open volumetric solar receivers: Experimental determination of thermophysical and heat transfer properties. *Energy*, 29(5):823–833.

Fend, T., Robert-Pitz-Paal, Reutter, O., Bauer, J., and Hoffschmidt, B. (2004b). Two novel high-porosity materials as volumetric receivers for concentrated solar radiation. *Solar Energy Materials and Solar Cells*, 84(1):291–304. International Solar Energy Society World Congress 2003.

Feng, Y. and Kleinstreuer, C. (2010). Nanofluid convective heat transfer in a parallel-disk system. *Int. J. Heat Mass Transf.*, 53(21):4619–4628.

Gersten, K. and Herwig, H. (2013). *Strömungsmechanik: Grundlagen der Impuls-, Wärme- und Stoffübertragung aus asymptotischer Sicht*. Springer-Verlag.

Ghalandari, M., Mirzadeh Koohshahi, E., Mohamadian, F., Shamshirband, S., and Chau, K. W. (2019). Numerical simulation of nanofluid flow inside a root canal. *Engineering Applications of Computational Fluid Mechanics*, 13(1):254–264.

Girolami, G. S. (2020). A brief history of thermodynamics, as illustrated by books and people. *J. Chem. Eng. Data*, 65(2):298–311.

Greenshields, C. (2022). *OpenFOAM v10 User Guide*. The OpenFOAM Foundation, London, UK.

Han, L., Lu, C., Yumashev, A., Bahrami, D., Kalbasi, R., Jahangiri, M., Karimipour, A., Band, S. S., Chau, K.-W., and Mosavi, A. (2021). Numerical investigation of magnetic field on forced convection heat transfer and entropy generation in a microchannel with trapezoidal ribs. *Engineering Applications of Computational Fluid Mechanics*, 15(1):1746–1760.

Hanlon, R. T. (2020). *Block by Block The Historical and Theoretical Foundations of Thermodynamics*. OXFORD Universuty Press.

Hischier, I., Leumann, P., and Steinfeld, A. (2012). Experimental and numerical analyses of a pressurized air receiver for Solar-Driven gas turbines. *J. Sol. Energy Eng.*, 134(2).

Ho, C. K. and Iverson, B. D. (2014). Review of high-temperature central receiver designs for concentrating solar power. *Renewable Sustainable Energy Rev.*, 29:835–846.

Howes, F. A. and Whitaker, S. (1985). The spatial averaging theorem revisited. *Chem. Eng. Sci.*, 40(8):1387–1392.

Hsu, C. T. and Cheng, P. (1990). Thermal dispersion in a porous medium. *Int. J. Heat Mass Transf.*, 33(8):1587–1597.

Jemmal, Y., Zari, N., and Maaroufi, M. (2017). Experimental characterization of siliceous rocks to be used as filler materials for air-rock packed beds thermal energy storage systems in concentrated solar power plants. *Sol. Energy Mater. Sol. Cells*, 171:33–42.

Kalita, J. C. and Dass, A. K. (2011). Higher order compact simulation of Double-Diffusive natural convection in a vertical porous annulus. *Engineering Applications of Computational Fluid Mechanics*, 5(3):357–371.

Kaviany, M. (1999). *Principles of Heat Transfer in Porous Media*. Springer, New York.

Khan, F. A. and Straatman, A. G. (2016). Closure of a macroscopic turbulence and non-equilibrium turbulent heat and mass transfer model for a porous media comprised of randomly packed spheres. *Int. J. Heat Mass Transf.*, 101:1003–1015.

Kock, F. and Herwig, H. (2004). Local entropy production in turbulent shear flows: a high-reynolds number model with wall functions. *Int. J. Heat Mass Transf.*, 47(10):2205–2215.

Kock, F. and Herwig, H. (2005). Entropy production calculation for turbulent shear flows and their implementation in cfd codes. *Int. J. Heat Fluid Flow*, 26(4):672–680.

Kostic, M. M. (2011). Revisiting the second law of energy degradation and entropy generation: From sadi carnot's ingenious reasoning to holistic generalization. *AIP Conf. Proc.*, 1411(1):327–350.

Kotas, T. J., Mayhew, Y. R., and Raichura, R. C. (1995). Nomenclature for exergy analysis. *Proc. Inst. Mech. Eng. A: J. Power Energy*, 209(4):275–280.

Kribus, A., Gray, Y., Grijnevich, M., Mittelman, G., Mey-Cloutier, S., and Caliot, C. (2014). The promise and challenge of solar volumetric absorbers. *Solar Energy*, 110:463–481.

Kribus, A., Ries, H., and Spirkl, W. (1996). Inherent limitations of volumetric solar receivers. *J. Sol. Energy Eng.*, 118(3):151–155.

Krittacom, B. and Kamiuto, K. (2009). Radiation emission characteristics of an Open-Cellular porous burner. *J. Therm. Sci. Technol.*, 4(1):13–24.

Kun-Can, Z., Tong, W., Hai-Cheng, L., Zhi-Jun, G., and Wen-Fei, W. (2017). Fractal analysis of flow resistance in random porous media based on the staggered pore-throat model. *Int. J. Heat Mass Transf.*, 115:225–231.

Kuwahara, F., Nakayama, A., and Koyama, H. (1996). A numerical study of thermal dispersion in porous media. *J. Heat Transfer*, 118(3):756–761.

Lee, K. and Howell, J. R. (1987). Forced convective and radiative transfer within a highly porous layer exposed to a turbulent external flow field. In *Proceedings of the 1987 ASME-JSME*, pages 377–386, Honolulu.

Liu, G., Gong, W., Wu, H., and Lin, A. (2021). Experimental and CFD analysis on the pressure ratio and entropy increment in a cover-plate pre-swirl system of gas turbine engine. *Engineering Applications of Computational Fluid Mechanics*, 15(1):476–489.

Mahian, O., Kianifar, A., Kleinstreuer, C., Al-Nimr, M. A., Pop, I., Sahin, A. Z., and Wongwises, S. (2013). A review of entropy generation in nanofluid flow. *Int. J. Heat Mass Transf.*, 65:514–532.

Modest, M. F. (2013). *Radiative Heat Transfer*. Academic Press.

Moghaddami, M., Mohammadzade, A., and Esfehani, S. A. V. (2011). Second law analysis of nanofluid flow. *Energy Convers. Manage.*, 52(2):1397–1405.

Moran, M. J. (1989). *Availability analysis: a guide to efficient energy use corrected edition*. ASME press, New York.

Moran, M. J. and Sciubba, E. (1994). Exergy analysis: Principles and practice. *J. Eng. Gas Turbines Power*, 116(2):285–290.

Nagano, Y. and Kim, C. (1988). A Two-Equation model for heat transport in wall turbulent shear flows. *J. Heat Transfer*, 110(3):583–589.

Nakayama, A. and Kawahara, F. (1999). A macroscopic turbulence model for flow in a porous medium. *Journal of Fluids Engineering*, 121(2):427–433.

OpenFOAM V9 (2021). *The OpenFOAM Fundation Ltd.*

Pabst, C., Feckler, G., Schmitz, S., Smirnova, O., Capuano, R., Hirth, P., and Fend, T. (2017). Experimental performance of an advanced metal volumetric air receiver for solar towers. *Renewable Energy*, 106:91–98.

Patankar, S. V. (2018). *Numerical heat transfer and fluid flow*. CRC press.

Patankar, S. V. and Spalding, D. B. (1972). A calculation procedure for heat, mass and momentum transfer in three-dimensional parabolic flows. *Int. J. Heat Mass Transf.*, 15(10):1787–1806.

Pedras, M. H. J. and de Lemos, M. J. S. (2001). Macroscopic turbulence modeling for incompressible fow through undeformable porous media. *Int. J. Heat Mass Transf.*, 44:1081–1093.

Quintard, M. and Whitaker, S. (1994). Transport in ordered and disordered porous media II: Generalized volume averaging. *Transp. Porous Media*, 14(2):179–206.

Reynolds, O. (1895). IV. on the dynamical theory of incompressible viscous fluids and the determination of the criterion. *Philosophical Transactions of the Royal Society of London. (A.)*, 186:123–164.

Saito, M. B. and de Lemos, M. J. S. (2005). Interfacial heat transfer coefficient for non-equilibrium convective transport in porous media. *Int. Commun. Heat Mass Transfer*, 32(5):666–676.

Salih, S. Q., Aldlemy, M. S., Rasani, M. R., Ariffin, A. K., Ya, T. M. Y. S. T., Al-Ansari, N., Yaseen, Z. M., and Chau, K.-W. (2019). Thin and sharp edges bodies-fluid interaction simulation using cut-cell immersed boundary method. *Engineering Applications of Computational Fluid Mechanics*, 13(1):860–877.

Salvi, P. R. and Schettino, V. (2019). Sadi carnot's réflexions and the foundation of thermodynamics. *Substantia*, 3(2):73–96.

Sarmiento-Laurel, C., Cardemil, J., Herrmann, B., and Calderon, W. (2019). Heat transfer framework for selecting the structure of open volumetric air receivers. In *Proceedings of the ISES Solar World Congress 2019*, Freiburg, Germany. International Solar Energy Society.

Sarmiento-Laurel, C., Cardemil, J. M., and Calderón-Muñoz, W. R. (2022). Local entropy generation model for numerical CFD analysis of fluid flows through porous media, under laminar and turbulent regimes. *Engineering Applications of Computational Fluid Mechanics*, 16(1):804–825.

Sciacovelli, A., Verda, V., and Sciubba, E. (2015). Entropy generation analysis as a design tool—a review. *Renewable Sustainable Energy Rev.*, 43:1167–1181.

Shah, R. K., Shah, R. K., and Sekulic, D. P. (2003). *Fundamentals of heat exchanger design*. John Wiley & Sons, Hoboken, N.J.

Singh, S., Sørensen, K., Condra, T., Batz, S. S., and Kristensen, K. (2019). Investigation on transient performance of a large-scale packed-bed thermal energy storage. *Appl. Energy*, 239:1114–1129.

Slattery, J. C. (1967). Flow of viscoelastic fluids through porous media. *AIChE J.*, 13(6):1066–1071.

Song, Z. and Liu, B. (2018). Optimization design for tandem cascades of compressors based on adaptive particle swarm optimization. *Engineering Applications of Computational Fluid Mechanics*, 12(1):535–552.

Spelling, J., Favrat, D., Martin, A., and Augsburger, G. (2012). Thermoeconomic optimization of a combined-cycle solar tower power plant. *Energy*, 41(1):113–120.

Sutherland, W. (1893). LII. the viscosity of gases and molecular force. *The London, Edinburgh, and Dublin Philosophical Magazine and Journal of Science*, 36(223):507–531.

Teruel, F. E. and Rizwan-uddin (2009a). A new turbulence model for porous media flows. part i: Constitutive equations and model closure. *Int. J. Heat Mass Transf.*, 52(19):4264–4272.

Teruel, F. E. and Rizwan-uddin (2009b). A new turbulence model for porous media flows. part II: Analysis and validation using microscopic simulations. *Int. J. Heat Mass Transf.*, 52(21):5193–5203.

Thomson, W. (1853). Xv.—on the dynamical theory of heat, with numerical results deduced from mr joule's equivalent of a thermal unit, and m. regnault's observations on steam. *Transactions of the Royal Society of Edinburgh*, 20(2):261–288.

Ting, T. W., Hung, Y. M., and Guo, N. (2015). Entropy generation of viscous dissipative nanofluid flow in thermal non-equilibrium porous media embedded in microchannels. *Int. J. Heat Mass Transf.*, 81:862–877.

Torabi, M., Torabi, M., and Peterson, G. P. (2017). Heat transfer and entropy generation analyses of forced convection through porous media using pore scale modeling. *J. Heat Transfer*, 139(1).

Torabi, M., Torabi, M., Yazdi, M. E., and Peterson, G. P. (2019). Fluid flow, heat transfer and entropy generation analyses of turbulent forced convection through isotropic porous media using RANS models. *Int. J. Heat Mass Transf.*, 132:443–461.

Vafai, K. (2015). *Handbook of Porous Media*. CRC Press.

Villafán-Vidales, H. I., Abanades, S., Caliot, C., and Romero-Paredes, H. (2011). Heat transfer simulation in a thermochemical solar reactor based on a volumetric porous receiver. *Appl. Therm. Eng.*, 31(16):3377–3386.

Whitaker, S. (1969). ADVANCES IN THEORY OF FLUID MOTION IN POROUS MEDIA. *Ind. Eng. Chem.*, 61(12):14–28.

Whitaker, S. (1998). *The Method of Volume Averaging*. Springer Science & Business Media.

Wilcox, D. C. (2006). *Turbulence modeling for CFD*. DCW Industries, Inc., La Cañada, California.

Worth, D. J., Spence, A., Crumpton, P. I., and Kolaczkowski, S. T. (1996). Radiative exchange between square parallel channels in a concentric monolith structure. *Int. J. Heat Mass Transf.*, 39(7):1463–1474.

Wu, J. and Yu, B. (2007). A fractal resistance model for flow through porous media. *Int. J. Heat Mass Transf.*, 50(19):3925–3932.

Wu, Z., Caliot, C., Bai, F., Flamant, G., Wang, Z., Zhang, J., and Tian, C. (2010). Experimental and numerical studies of the pressure drop in ceramic foams for volumetric solar receiver applications. *Appl. Energy*, 87(2):504–513.

Wu, Z., Caliot, C., Flamant, G., and Wang, Z. (2011a). Coupled radiation and flow modeling in ceramic foam volumetric solar air receivers. *Solar Energy*, 85(9):2374–2385.

Wu, Z., Caliot, C., Flamant, G., and Wang, Z. (2011b). Numerical simulation of convective heat transfer between air flow and ceramic foams to optimise volumetric solar air receiver performances. *Int. J. Heat Mass Transf.*, 54(7):1527–1537.

Xu, C., Song, Z., Chen, L.-d., and Zhen, Y. (2011). Numerical investigation on porous media heat transfer in a solar tower receiver. *Renewable Energy*, 36(3):1138–1144.

Younis, L. B. and Viskanta, R. (1993). Experimental determination of the volumetric heat transfer coefficient between stream of air and ceramic foam. *Int. J. Heat Mass Transf.*, 36(6):1425–1434.

Annex A

A.1 General energy equation

$$\frac{D}{Dt}\left(\rho_f e + \frac{1}{2}\rho_f u_j u_j\right) = \frac{\partial}{\partial x_i}(u_j \sigma_{ij}) + u_j \rho_f f_j - \frac{\partial q_j}{\partial x_j} \tag{A.1}$$

$$\begin{aligned}\frac{\partial}{\partial t}\left(\rho_f e + \frac{1}{2}\rho_f u_j u_j\right) + \frac{\partial}{\partial x_k}\left[\left(\rho_f e + \frac{1}{2}\rho_f u_j u_j\right) u_k\right] \\ = \frac{\partial}{\partial x_i}(u_j \sigma_{ij}) + u_j \rho_f f_j - \frac{\partial q_j}{\partial x_j}\end{aligned} \tag{A.2}$$

where e is internal energy per unit of mass, σ_{ij} the surface forces tensor, f_j the mass forces vector and q_j net the heat flux.
Then, expanding and regrouping the left-hand side terms,

$$\begin{aligned}&\frac{\partial}{\partial t}\left(\rho_f e + \frac{1}{2}\rho_f u_j u_j\right) + \frac{\partial}{\partial x_k}\left[\left(\rho_f e + \frac{1}{2}\rho_f u_j u_j\right) u_k\right] \\ &= \frac{\partial}{\partial t}(\rho_f) e + \rho_f \frac{\partial}{\partial t}(e) + \frac{\partial}{\partial t}(\rho_f)\frac{1}{2}u_j u_j \\ &\quad + \rho_f \frac{\partial}{\partial t}\left(\frac{1}{2}u_j u_j\right) + \frac{\partial}{\partial x_k}(e)\rho_f u_k + e\frac{\partial}{\partial x_k}(\rho_f u_k) \\ &\quad + \frac{\partial}{\partial x_k}(\rho_f u_k)\frac{1}{2}u_j u_j + \frac{\partial}{\partial x_k}\left(\frac{1}{2}u_j u_j\right)\rho_f u_k\end{aligned} \tag{A.3}$$

$$\begin{aligned}&= e\left(\frac{\partial}{\partial t}(\rho_f) + \frac{\partial}{\partial x_k}(\rho_f u_k)\right) + \rho_f \frac{\partial}{\partial t}(e) \\ &\quad + \frac{1}{2}u_j u_j\left(\frac{\partial}{\partial t}(\rho_f) + \frac{\partial}{\partial x_k}(\rho_f u_k)\right) \\ &\quad + \rho_f \frac{\partial}{\partial t}\left(\frac{1}{2}u_j u_j\right) + \frac{\partial}{\partial x_k}(e)\rho_f u_k + \frac{\partial}{\partial x_k}\left(\frac{1}{2}u_j u_j\right)\rho_f u_k\end{aligned} \tag{A.4}$$

Substituting the continuity equation in the first and second parentheses in Equation A.4.

$$
\begin{aligned}
& e\left(\frac{\partial}{\partial t}(\rho_f)+\frac{\partial}{\partial x_k}(\rho_f u_k)\right)+\rho_f\frac{\partial}{\partial t}(e) \\
& \quad+\frac{1}{2}u_j u_j\left(\frac{\partial}{\partial t}(\rho_f)+\frac{\partial}{\partial x_k}(\rho_f u_k)\right) \\
& \quad+\rho_f\frac{\partial}{\partial t}\left(\frac{1}{2}u_j u_j\right)+\frac{\partial}{\partial x_k}(e)\rho_f u_k+\frac{\partial}{\partial x_k}\left(\frac{1}{2}u_j u_j\right)\rho_f u_k \\
& =\rho_f\frac{\partial}{\partial t}(e)+\rho_f\frac{\partial}{\partial t}\left(\frac{1}{2}u_j u_j\right)+\frac{\partial}{\partial x_k}(e)\rho_f u_k \\
& \quad+\frac{\partial}{\partial x_k}\left(\frac{1}{2}u_j u_j\right)\rho_f u_k \qquad \text{(A.5)}
\end{aligned}
$$

$$
=\rho_f\frac{\partial}{\partial t}(e)+\frac{\partial}{\partial x_k}(e)\rho_f u_k+\rho_f u_j\frac{\partial}{\partial t}(u_j)+\frac{\partial}{\partial x_k}(u_j)\rho_f u_j u_k \qquad \text{(A.6)}
$$

Thus, including Equation A.6 in Equation A.1,

$$
\begin{aligned}
& \rho_f\left[\left(\frac{\partial}{\partial t}(e)+\frac{\partial}{\partial x_k}(e)u_k\right)+\left(u_j\frac{\partial}{\partial t}(u_j)+\frac{\partial}{\partial x_k}(u_j)u_j u_k\right)\right] \\
& \quad=u_j\frac{\partial}{\partial x_i}(\sigma_{ij})+\sigma_{ij}\frac{\partial}{\partial x_i}(u_j)+u_j\rho_f f_j-\frac{\partial q_j}{\partial x_j} \qquad \text{(A.7)}
\end{aligned}
$$

A.2 Spatial-averaging method on momentum equation

Multiplying for u_j and applying the spatial-averaging method over the momentum transport equation, the relation used in Equation (11) is determined as follows:

$$
\rho_f\frac{\partial}{\partial t}(u_j)+\rho_f u_k\frac{\partial}{\partial x_k}(u_j)=\frac{\partial}{\partial x_i}(\sigma_{ij})+\rho_f f_i \qquad \text{(A.8)}
$$

$$
\phi\left\langle u_j\left[\rho_f\frac{\partial}{\partial t}(u_j)+\rho_f u_k\frac{\partial}{\partial x_k}(u_j)\right]\right\rangle^i=\phi\left\langle u_j\left[\frac{\partial}{\partial x_i}(\sigma_{ij})+\rho_f f_i\right]\right\rangle^i \qquad \text{(A.9)}
$$

$$
\phi\left\langle \rho_f u_j\frac{\partial}{\partial t}(u_j)+\rho_f u_j u_k\frac{\partial}{\partial x_k}(u_j)\right\rangle^i=\phi\left\langle u_j\frac{\partial}{\partial x_i}(\sigma_{ij})+\rho_f u_j f_i\right\rangle^i \qquad \text{(A.10)}
$$

$$
\begin{aligned}
& \rho_f\phi\left\langle u_j\frac{\partial}{\partial t}(u_j)\right\rangle^i+\rho_f\phi\left\langle u_j u_k\frac{\partial}{\partial x_k}(u_j)\right\rangle^i \\
& \quad=\phi\left\langle u_j\frac{\partial}{\partial x_i}(\sigma_{ij})\right\rangle^i+\phi\left(\langle u_j\rangle^i\left\langle\frac{\partial}{\partial x_i}(\sigma_{ij})\right\rangle^i\right. \\
& \qquad\left.+\left\langle {}^i(u_j)^i\left(\frac{\partial}{\partial x_i}(\sigma_{ij})\right)\right\rangle^i\right)+\phi\langle\rho_f u_j f_i\rangle^i \qquad \text{(A.11)}
\end{aligned}
$$

A.3 Energy and entropy relation from Gibbs' equation

From the Gibbs equation Cantwell (2022).

$$T\frac{Ds}{Dt} = \frac{De}{Dt} + P\frac{D(1/\rho)}{Dt} \tag{A.12}$$

$$T\frac{Ds}{Dt} = \frac{De}{Dt} - \frac{P}{\rho^2}\frac{D\rho}{Dt} \tag{A.13}$$

$$\rho T\frac{Ds}{Dt} = \rho\frac{De}{Dt} - \frac{P}{\rho}\frac{D\rho}{Dt} \tag{A.14}$$

A.4 Spatial-averaged transport equations for NTE porous media

A.4.1 Continuity and momentum equations

$$\frac{\partial \rho_f}{\partial t} + \rho_f \frac{\partial}{\partial x_k}\Big(\phi \left\langle \bar{u}_k \right\rangle^i\Big) = 0 \tag{A.15}$$

$$\begin{aligned}
&\frac{\partial \left(\rho_f \phi \langle \bar{u} \rangle^i\right)}{\partial t} + \rho_f \frac{\partial}{\partial x_k}\left(\phi \langle \bar{u}_j \bar{u}_k \rangle^i\right) \\
&\quad = \frac{\partial}{\partial x_i}\left(-\phi \left\langle \bar{P} \right\rangle^i \delta_{ij} + \phi\mu\left(\frac{\partial \langle \bar{u_i} \rangle^i}{\partial x_j} + \frac{\partial \langle \bar{u_j} \rangle^i}{\partial x_i}\right)\right. \\
&\qquad \left. - \frac{2}{3}\phi\mu\left(\delta_{ij}\frac{\partial \langle \bar{u_k} \rangle^i}{\partial x_k}\right)\right) \\
&\qquad - \rho_f \frac{\partial}{\partial x_k}\left(\phi \overline{\langle u_j{}' u_k{}' \rangle^i}\right) - \phi\left(\frac{\mu_f}{k_1}\overline{u_D} + \frac{\rho_f}{k_2}|\overline{u_D}|\overline{u_D}\right)
\end{aligned} \tag{A.16}$$

where ρ_f is the fluid density, $\bar{u}$ the time-averaged velocity, $u^{'}$ the velocity time-fluctuation term, ϕ the porosity, $\bar{P}$ the time-averaged fluid pressure and μ fluid viscosity.

The last two terms in Eq. A.16 derive from the expressions (2.5) and (2.6) applied to both surface force terms, pressure, and viscous shear stress. They represent the interaction between

the fluid with the solid matrix as a drag force. Commonly are defined as Darcy–Forchheimer terms Pedras and de Lemos (2001), as follows:

$$\bar{R} = \phi \left(\frac{\mu_f}{k_1} \overline{u_D} + \frac{\rho_f}{k_2} |\overline{u_D}| \overline{u_D} \right) \tag{A.17}$$

The last two in Equation (A.17) are determined experimentally, considering the Darcian velocity $u_D = \phi u_i$, where k_1 and k_2 are correlation constants.

A.4.2 Energy equation

The energy equation is split into two parts to consider NTE de Lemos (2012) between both phases (fluid and solid).

$$\begin{aligned} \rho_f c_{p,f} & \left(\frac{\partial \left(\phi \langle \overline{T_f} \rangle^i \right)}{\partial t} + \frac{\partial}{\partial x_k} \left(\phi \langle \overline{T_f}\, \overline{u}_k \rangle^i \right) \right) \\ & = \frac{\partial}{\partial x_k} \left(\phi \lambda_f \frac{\partial \langle \overline{T_f} \rangle^i}{\partial x_k} \right) - \rho_f c_{p,f} \frac{\partial}{\partial x_k} \left(\phi \overline{\langle T_f' u_k' \rangle^i} \right) \\ & \quad + h_i a_i \left(\langle \overline{T_s} \rangle^i - \langle \overline{T_f} \rangle^i \right) \end{aligned} \tag{A.18}$$

$$\begin{aligned} & \rho_s c_{p,s} \frac{\partial \left((1-\phi) \langle \overline{T_s} \rangle^i \right)}{\partial t} \\ & \quad = \frac{\partial}{\partial x_k} \left((1-\phi) \lambda_s \frac{\partial \langle \overline{T_s} \rangle^i}{\partial x_k} \right) - h_i a_i \left(\langle \overline{T_s} \rangle^i - \langle \overline{T_f} \rangle^i \right) \end{aligned} \tag{A.19}$$

where c_p is the specific heat, λ the thermal conductivity, $\bar{T}$ is time-averaged temperature, T' the temperature fluctuation in time term, and the subscripts f and s are related to fluid and solid phases, respectively.

A.5 Comparison factor N_{Sgen}

N_{Sgen} compares the integrated LEG on the entire volume of heat transfer against the viscous and hydrodynamic resistances.

$$N_{Sgen} = \frac{\displaystyle\int_{C,\mathcal{V}} \left(\left\langle \dot{s}_{\Theta,\bar{C}} \right\rangle^v + \langle \dot{s}_{\Theta,C'} \rangle^v + \dot{s}_{\Theta,v} \right) d\mathcal{V}}{\displaystyle\int_{C,\mathcal{V}} \left(\left\langle \dot{s}_{\Phi,\bar{D}} \right\rangle^v + \langle \dot{s}_{\Phi,D'} \rangle^v + \dot{s}_{\Phi,DF} \right) d\mathcal{V}} \tag{A.20}$$

where $\left\langle \dot{s}_{\Theta,\bar{C}} \right\rangle^{v}$ is the LEG rate by the conductive heat transfer related to the time-average fluid temperature, $\langle \dot{s}_{\Theta,C'} \rangle^{v}$ is the LEG rate due to the conductive heat transfer associated with the fluid temperature fluctuations. The last term $\dot{s}_{\Theta,v}$ is the entropy generation rate, due the volumetric heat transfer between the solid and fluid phases, $\left\langle \dot{s}_{\Phi,\bar{D}} \right\rangle^{v}$ is the LEG rate due to viscous dissipation related to the time-average velocity, $\langle \dot{s}_{\Phi,D'} \rangle^{v}$ is the LEG rate by viscous dissipation regarded to the fluid velocity time fluctuations, and $\dot{s}_{\Phi,DF}$ is the LEG rate associated to Darcy-Forchheimer's hydrodynamic resistance due to the presence of the solid matrix against the flow.